UNIVERSITAT POLITÈCNICA
DE CATALUNYA
BARCELONATECH

Study of a Compton camera based on CsI(Tl) scintillator bars for radiological environmental imaging

María D. Rodríguez

ADVERTIMENT La consulta d'aquesta tesi queda condicionada a l'acceptació de les següents condicions d'ús: La difusió d'aquesta tesi per mitjà del repositori institucional UPCommons (http://upcommons.upc.edu/tesis) i el repositori cooperatiu TDX (http://www.tdx.cat/) ha estat autoritzada pels titulars dels drets de propietat intel·lectual **únicament per a usos privats** emmarcats en activitats d'investigació i docència. No s'autoritza la seva reproducció amb finalitats de lucre ni la seva difusió i posada a disposició des d'un lloc aliè al servei UPCommons o TDX. No s'autoritza la presentació del seu contingut en una finestra o marc aliè a UPCommons (*framing*). Aquesta reserva de drets afecta tant al resum de presentació de la tesi com als seus continguts. En la utilització o cita de parts de la tesi és obligat indicar el nom de la persona autora.

ADVERTENCIA La consulta de esta tesis queda condicionada a la aceptación de las siguientes condiciones de uso: La difusión de esta tesis por medio del repositorio institucional UPCommons (http://upcommons.upc.edu/tesis) y el repositorio cooperativo TDR (http://www.tdx.cat/?locale-attribute=es) ha sido autorizada por los titulares de los derechos de propiedad intelectual **únicamente para usos privados enmarcados** en actividades de investigación y docencia. No se autoriza su reproducción con finalidades de lucro ni su difusión y puesta a disposición desde un sitio ajeno al servicio UPCommons No se autoriza la presentación de su contenido en una ventana o marco ajeno a UPCommons (*framing)*. Esta reserva de derechos afecta tanto al resumen de presentación de la tesis como a sus contenidos. En la utilización o cita de partes de la tesis es obligado indicar el nombre de la persona autora.

WARNING On having consulted this thesis you're accepting the following use conditions: Spreading this thesis by the institutional repository UPCommons (http://upcommons.upc.edu/tesis) and the cooperative repository TDX (http://www.tdx.cat/?locale- attribute=en) has been authorized by the titular of the intellectual property rights **only for private uses** placed in investigation and teaching activities. Reproduction with lucrative aims is not authorized neither its spreading nor availability from a site foreign to the UPCommons service. Introducing its content in a window or frame foreign to the UPCommons service is not authorized (framing). These rights affect to the presentation summary of the thesis as well as to its contents. In the using or citation of parts of the thesis it's obliged to indicate the name of the author.

UNIVERSITAT POLITÈCNICA DE CATALUNYA

Doctoral dissertation

Nuclear and ionizing radiation engineering program

Study of a Compton camera based on CsI(Tl) scintillator bars for radiological environmental imaging

Author:

María D. Rodríguez

Supervisor:

Dr. Arturo Vargas

October 2020

Agradecimientos

En primer lugar me gustaría agradecer al Consejo de Seguridad Nuclear por su ayuda económica a través de la Cátedra Argos. También doy las gracias a mi director de tesis, Dr. Arturo Vargas, que me haya dado la oportunidad de realizar esta tesis y por su inestimable guia durante estos cuatro años. Este período ha sido una gran oportunidad para crecer personal, intelectual y profesionalmente.

También me gustaría agradecer a aquellas personas que me permitirerion realizar medidas en el laboratoria. En especial a Ariel Tarifeño por todo el tiempo invertido en explicarme el funcionamiento del sistema de adquisición de datos. Así como a María Roig y a Anna Camp que con su ayuda pude realizar las medidas en el laboratorio de calibración y dosimetría.

A todos mis compañeros del INTE que me permitieron tener esas comidas más llevaderas. En espacial agradecele a Sara Principi, Dani Mulas y Adrià Casanovas por su consejo y apoyo durante la tesis. La han hecho más llevadera.

Sobre todo quería agradecerle a mi familia por todo su apoyo durante este tiempo. En especial a Lina, mi madre, y a Sergio, mi marido. Sin su ayuda no podría haberla acabado.

Summary

Compton cameras are used for radiological imaging, which can be useful in environmental applications and especially in determining the position of hidden sources. Current Compton cameras are based on pixelated detectors with complex electronic instrumentation and these devices are usually expensive. In order to overcome these issues, a Compton camera consisting of scintillator bars with two photo-sensors placed at both ends is a promising option. These detectors determine the location of γ-ray interactions and energies along the bar through the combination of signals from both photo-sensors.

Characterization of two identical CsI(Tl) scintillator bars with two silicon photomultipliers each was done. The basic characterization parameters of detectors, such as the attenuation coefficient, position resolution and energy resolution, were determined experimentally with a collimated ^{137}Cs point source. Different light attenuation coefficients were found for identical scintillators, causing different position resolutions. This fact highlights the importance of carrying out a control analysis for each detector. In addition, the position resolution and energy resolution were found to be independent of the position of γ-ray interactions within the crystal.

Monte Carlo (MC) simulations with PENELOPE/penEasy were carried out to design a Compton camera. In order to achieve this, the MC simulations needed to be validated. This was done by comparing both simulated and experimental data obtained in two different experimental measurement campaigns. In the first campaign, two detectors were irradiated individually with a collimated ^{137}Cs point source, while the second campaign consisted of irradiating a simple Compton camera made of two CsI(Tl) scintillator bars. The geometry defined in the MC simulations and the codes used to calculate the image for a Compton camera based on CsI(Tl) scintillator bars were validated with these experimental campaigns. The response of each individual detector, the Compton camera efficiency, the angular resolution and images obtained with MC simulations and experimental measurements were compared. Results show good agreement between experimental and simulated data.

Once the MC simulations were fully validated, the design of a Compton camera consisting of two layers with four CsI(Tl) scintillator bars each was done. The cross-section size of crystals and distance between layers were optimized based on Compton camera efficiency, angular resolution and image resolution. This analysis was carried out with an energy range of 360 – 1330 keV. The final optimized Compton camera consists of two layers separated by 10 cm. Each layer has four 2 × 2 × 10 cm^3 CsI(Tl) scintillator bars.

The Compton camera has a field of view of around 60°, 45° and 45° for sources of ^{131}I, ^{137}Cs and ^{60}Co, respectively. The Compton camera efficiency is defined as the events that are used to calculate the image (number of cones) per number of gamma-rays emitted by the source (a history in MC simulations). The Compton camera has an efficiency of $4.563 \cdot 10^{-7} \pm 9 \cdot 10^{-10}$ cones/history, $6.490 \cdot 10^{-7} \pm 1.1 \cdot 10^{-9}$ cones/history and $3.841 \cdot 10^{-7} \pm 7 \cdot 10^{-10}$ cones/history for sources of ^{131}I, ^{137}Cs and ^{60}Co, respectively when the distance between the Compton camera and sources is 2 metres. At this distance, the angular resolution is found to be between 11° and 16° ($FWHM$), depending on the energy of the incident γ-ray. Image resolution is found to be between 17° and 21° ($FWHM_x$) on the x-axis, while on the y-axis it is found to be between 16° and 27° ($FWHM_y$), also depending on the energy. The x-axis is the horizontal image axis, while the y-axis is the vertical axis.

The ability of the Compton camera to make use of the simple back-projection method to identify radioactive material in the environment has also been evaluated by simulating several point sources. The Compton camera was able to detect several point sources simultaneously, however, as the number of sources increases, the images became blurred.

The capacity of the Compton camera is promising, since it can detect several sources in the environment according to MC simulations. Therefore, the construction of a Compton camera based on eight 2 × 2 × 10 cm^3 CsI(Tl) scintillator bars should prove to be useful for environmental measurements and for installation on unmanned aerial systems, commonly called “drones”.

Contents

List of Figures

List of Tables

Chapter 1

Introduction

Artificial radionuclides can be found in the environment since radioactive particles are released from nuclear reactor accidents, nuclear weapons and other activities involving nuclear and radiological installations. These possible releases cause a heterogeneous distribution of radioactive material in the environment. After first indications of a radiological incident, radiation protection authorities and other decision makers need both fast and reliable information about affected and contaminated areas in order to take both urgent and appropriate decisions regarding protecting the public and workers. Furthermore, public confidence in governmental emergency readiness depends on the availability of distributing reliable radiological data in the media.

After the accident at the Fukushima Dai-chi Nuclear Power Plant (FDNPP), a large amount of radioactive material was released into the environment over large areas. In order to evaluate the most affected areas as well as exposure to humans and the environment, large-scale environmental monitoring was carried out (Saito and Onda, 2015).

One of the techniques used in the vicinity of the FDNPP was airborne radiation monitoring in order to assess the initial dose rate and its evolution with time. Estimation of the initial dose rate and its evolution with time in this case was carried out by using fixed detectors, both walking and car-borne surveys and taking measurements with manned and unmanned aerial systems (UAS) commonly named “drones”. The use of UAS allowed them to cover large areas in a short period of time and also to take measurements in areas of difficult access, such as mountains and forests (Saito et al., 2019; Sanada et al., 2016, 2018). In addition, the use of UAS prevents personal exposure to contamination or unexpectedly high levels of ionizing radiation.

In the FDNPP aerial measurement campaigns, large NaI scintillator detectors(12.6L volume) were installed in a manned helicopter, while LaBr3:Ce scintillation detectors (0.13L volume) were installed on a UAS (Sanada et al., 2018). The manned and unmanned aerial systems flew in cross-lines separated by a certain distance in order to map the radiological risk and to localize hot-spots of radioactive contamination. The energy spectrum and the GPS data were stored every second. Estimation of the ambient dose equivalent rate normalized at 1 m above ground level (AGL) was done. The field of view of a scintillator detector coupled to a manned or an unmanned aerial system is approximately a circular area of radius equal to the altitude of the flight. Therefore, average air dose rate is determined in this area. Spatial resolution depends on the flight altitude.

Results from the measurements taken with manned and unmanned aerial systems are shown on maps. The dose rate map obtained with a UAS has a much better resolution due to the fact that it can fly at a lower altitude AGL. The maps obtained in the vicinity of the FDNPP using an UAS show four deposition patterns that indicate four unique releases during the accident. These incidents were not possible to determine with the measurements carried out by aerial manned vehicles (Sanada et al., 2018; Sanada and Torii, 2015). It is important to point out that measurements obtained with a UAS provides additional information regarding the spatial resolution in contrast to manned systems, which is of the utmost relevance for decision makers to identify the most affected areas.

An alternative to the detection methodology mentioned above is the use of environmental γ-ray imaging. It can provide an improvement in the spatial resolution data and a faster response in comparison with conventional spectrometric monitors. In this case, the UAS would be hovering for a period of time of a few minutes in order to obtain a radiological image with sufficient resolution. This thesis consists of determining the possibility of using airborne gamma-ray image systems mounted on a UAS.

1.1 State of the art of environmental γ-ray imaging

A common technique of gamma-ray imaging is the mechanical collimated Gamma Camera (Gormley et al., 1997). It generally consists of a collimator, a gamma photon detector and photomultiplier tubes. The collimator is made of a high-density material and generally has a large number of holes that allow photons from a particular direction to enter. The collimated photons are detected by the detector and a projection of the radiological source is obtained. Such gamma cameras have intrinsic limitations mainly due to the use of a mechanical collimator. The collimator cannot completely shield the high energy gamma-rays, which will cause a loss of contrast and resolution. The holes of the collimator should be as small as possible in order to obtain a better resolution, but this will decrease efficiency. Due to the fact that only specific directions for the incoming gamma-rays can reach the detector, the Field of View (FOV) is limited. In addition, the heavy collimator considerably increases the weight of such cameras, which makes its installation on UAS complicated and its operational efficiency seems barely feasible.

An alternative to overcome the above-mentioned drawbacks is the use of a Compton camera (Llosá, 2019). In this case, the mechanical collimator is substituted by a layer of detectors. Collimation is carried out electronically using two layers of detectors. It uses detectors that are both position and energy sensitive. Since a Compton camera does not use a mechanical collimator, the FOV is expected to be wider and the efficiency higher than mechanical cameras. It can perform the imaging in a wider energy range. Furthermore, the signal-to-noise ratio should be better than mechanical collimation because, in principle, a larger proportion of gamma-rays that come from the source are contributing to the image. In addition, a Compton camera is expected to be lighter than a Gamma Camera and could be installed on a common multi-rotor UAS. All of these factors make Compton cameras a preferred type of potential imaging systems mounted on a UAS.

A Compton camera typically consists of two layers of detectors: the scatter layer and the absorber layer. The detectors must be energy and position sensitive in order to determine the position of interactions and the deposited energy of γ-rays. When a γ-ray is scattered in the scatter layer and the scattered γ-ray is fully absorbed by the photoelectric effect in the absorber layer, the scattering angle of the incoming gamma ray can be calculated as is described in Section 2.6.

Originally, Compton cameras were developed for astrophysics research and have been successfully used in this field since the 1970's. Later on, Compton cameras were developed for medical imaging, homeland security and nuclear inspections. They were also used for identification of areas with high radioactive activity. For example, after the FDNPP accident a Compton camera, called ASTROCAM, capable of locating hot spots, was manufactured (Takeda et al., 2015). The monitor was made of Si and CdTe detectors. The incident gamma photons are scattered in the Si detector and then are fully absorbed in the CdTe detector. Using semiconductor detectors allowed them to have a good energy resolution ($FWHM/E =$ 2.2% at 662keV). Furthermore, the effect of Doppler broadening is smaller in Si devices than in other semiconductors. These factors give a good angular resolution: 5.4° ($FWHM$). They achieved a FOV of 2π. This Compton camera was tested in an area near the FDNPP, where it needed 30 minutes to obtain an image with a background of $0.5-1.0$ μSv/h. They managed to locate hot spots and verify the correct decontamination procedures. It is important to point out that the Compton camera is 445 mm in depth, 340 mm in width and 235 mm in height, and the weight is approximately 10 kg. Therefore, a huge unmanned helicopter would be needed to carry the detector and carry out the measurements for 30 minutes. This Compton camera needs a large enough number of semiconductor detectors to obtain good efficiency detection, which increases its cost to 667,000$ (Kagaya et al., 2015).

A more compact Compton camera was developed based on scintillator detectors in order to improve the sensitivity to γ-rays that come from ^{137}Cs and ^{134}Cs (Kataoka et al., 2013, 2018). This Compton camera consists of 2 layers of cubic Ce:GAGG scintillators coupled to large-area monolithic multi-pixel photon counter arrays. Photodetectors are placed on both sides of the crystals. This Compton camera, with a total weight of 1.9 kg, was coupled to a drone and tested in Fukushima. An image of a contaminated area was taken at 20 m height for 25 min. The Compton camera was able to locate the hot spots in quite a short time. Its energy and angular resolutions are 9.8% ($FWHM$) and 14° ($FWHM$), respectively. One of the main drawbacks of this Compton camera is its elevated cost, which is around 100.000 $.

The main differences between the two Compton cameras described above are the following. The use of scintillators causes a worsening of energy resolution, which causes an increase in uncertainty of the scattering angle θ_c and thus, a worse angular resolution is obtained. Furthermore, a Compton camera based on scintillator detectors only detects γ-rays with energies greater than 250 keV, while a Compton camera based on semiconductors developed by Takeda et al. (2015) is able to detect gamma-rays down to 100 keV. It is important to bear in mind that gamma-rays detected by a Compton camera must interact first in the scatter layer via Compton scattering and subsequently the scattered photon must be absorbed in the absorber. Therefore, those Compton cameras made of scatter detectors with low atomic number, such as Si semiconductor detectors, are able to detect lower energies. This is due to the fact that gamma-rays are less likely to be absorbed via the photoelectric effect in a material with a low atomic number.

The desirable characteristics for a Compton camera designed for homeland security are an excellent FOV, good angular and energy resolutions and quite good efficiency across a wide energy range ($0-3$ MeV) in order to enable the identification of a wide variety of radionuclides. In general, all these characteristics are not completely fulfilled at once because they depend strongly on the chosen materials of detectors, on their size and their geometric arrangement. Furthermore, a device for nuclear decommissioning or for emergency surveillance should be both portable and robust to allow transport onto and around nuclear sites and close to the accident. In addition, a Compton camera must be light so that it can be mounted on a UAS.

An option that would make the Compton camera robust, flexible enough in operation and with a lower cost than the previous systems described is a Compton imager consisting of long scintillator bars with two photo-sensors placed at both ends. The use of long scintillator bars offers an inexpensive design solution that could fit with the technical requirements of a Compton camera that needs to be installed on a common multi-rotor UAS. Furthermore, these detectors need only a few readout channels, which makes them easier to use than Compton cameras based on an array of a large number of small detectors.

Long scintillator bars with two photo-sensors placed at both ends have been studied since the 80's (Carter et al., 1982). They are able to determine the location of γ-ray interactions along the bar (1D) and energy deposited by combining the signals from both photo-sensors. The energy deposited is calculated by summing the signals from both photo-sensors, while the interaction position is obtained with the ratio of both signals. These kinds of detectors have been applied in many different fields.

For instance, they have been used in astrophysics. The use of NaI(Tl) scintillator bars with two photomultiplier tubes (PMTs) in a γ-ray telescope for energies of $0.2-10$ MeV was analysed in different works such as Carter et al. (1982) and Court et al. (1988). It is also possible to build a Compton scatter telescope. A prototype that is sensitive to γ-rays of $1-30$ MeV is shown in Zych et al. (1983). It consists of two arrays of plastic and NaI(Tl) scintillator bars coupled to two PMTs at both ends.

Scintillator bars are also used in high energy physics. A combination of several NaI scintillator bars with a large NaI detector is able to determine both the position of interaction and deposited energy of γ-rays with $E > 20$ MeV (Bassalleck et al., 1979).

These bars are also useful to carry out nuclear physics research. A cylindrical detector made of NaI(Tl) scintillator bars is shown in Kaloskamis et al. (1993). It was used to observe positrons produced in collisions of heavy nuclei. This is done by detecting annihilation radiation. Scheit et al. (1999) used NaI(Tl) cylindrical bars with two PMTs each in order to study the nuclear structure of unstable nuclei.

Askari et al. (2019) used a rectangular NaI(Tl) scintillator bar coupled to a PMT on each side to perform Gamma-ray Computed Tomography. The study was done using Monte Carlo simulations, which were validated with experimental data.

These types of detectors were also studied in the imaging medicine field. Vilardi et al. (2006) performed experimental measurements of polished long YAP:Ce and LYSO:Ge scintillator bars for different wrappings and coatings. They studied the influence of different wrappings and coatings on position, energy and time resolutions. The aim was to explore their ability to build a Positron Emission Tomography (PET) device. In the same field, Monte Carlo simulations of polished or wrapped YAP:Ce scintillator bars with PMTs at both ends were carried out (Ciocia et al., 2009). The optical processes of scintillation light were simulated in order to optimize position and energy resolutions.

The performance of a Compton camera is assessed by its ability to identify and locate radionuclides. It is therefore necessary to study the efficiency, angular resolution and image resolution of different geometrical configurations. The efficiency, angular resolution and image resolution of a Compton camera depends on detector characterization, such as the detector thicknesses and separation between layers. Thus, optimization of the Compton camera requires a study of many detector configurations and numerical simulations in order to find the best configuration. The most common technique to perform such a study is by using Monte Carlo simulations.

1.2 Objectives

The aim of the thesis is to design and characterize a Compton camera composed of scintillator bars. The objective is to determine whether the Compton camera can be used as an airborne imaging system to be mounted on a UAS for environment mapping. In order to achieve this, the following objectives were proposed:

1. Characterization of two scintillator bars. Their main characteristics, such as the

attenuation coefficient, energy resolution and position resolution, are determined using a point collimated ^{137}Cs source.

2. Adapt PENELOPE/penEasy MC software package in order for it to be used for Compton imaging. Deposited energies and position interactions of the simulated γ-rays are written in a file when a γ-ray interacts in the scatter and absorber layers. These files will be used as input to the image reconstruction algorithm.

3. Implement an image reconstruction algorithm. The Simple Back-Projection method is used to calculate images of radioactive sources.

4. Experimental measurements with a simple Compton camera based on two scintillator bars have been made in order to test the algorithm developed in point 3.

5. Validation of Monte Carlo simulations comparing experimental and simulated data.

6. Design of a Compton camera based on several scintillator bars. Different geometry configurations are simulated using PENELOPE/penEasy MC code in order to analyse the best configuration to locate hot spots. Efficiency, angular resolution and image resolution are optimized.

7. Characterization of the Compton camera designed in point 6.

1.3 Structure of the report

Chapter 2 describes the main methods and instrumentation used to develop the thesis. First, the scintillator detectors that were purchased and the data acquisition system are described. The method to determine the position of interaction and deposited energy after a γ-ray interaction in a scintillator bar is also explained. In addition, experimental measurements and Monte Carlo simulations with PENELOPE/penEasy are described together with the image reconstruction algorithm. Finally, the procedure used to carry out the design and characterization of the Compton camera based on scintillator bars is briefly described.

Experimental measurements are shown in Chapter 3. Two measurements campaigns were done in order to characterize the CsI(Tl) scintillator bars and to validate Monte Carlo simulations. The first campaign of measurements was carried out by irradiating the scintillator bars with a point collimated source. In the second campaign , a simple Compton camera made of two CsI(Tl) scintillator bars was irradiated at the Calibration and Dosimetry Laboratory (LCD) of the Institute of Energy Technologies (INTE) of the Technical University of Catalonia (UPC).

The design of a Compton camera consisting of two layers of CsI(Tl) detectors, called the scatter and absorber layers, is done by Monte Carlo simulations in Chapter 4. The design is done by analysing the Compton camera efficiency with the angular resolution and image resolution. The Compton camera was designed in three stages. First, the optimum geometric arrangement of scintillator detectors was analysed. The optimum sizes of scatter and absorber detectors were then studied. Finally, the Compton camera performance was analysed based on the distance between the scatter and absorber layers.

Chapter 5 describes the characterization of the Compton camera designed in Chapter 4. The parameters that are studied are the Compton camera field of view and minimum number of cones to locate a source. The minimum time needed to locate a source with a certain activity is estimated from the efficiency and the minimum number of cones. The variation of efficiency, angular resolution and image resolution with distance between sources and the Compton camera is also studied. Furthermore, the ability to locate several point and surface sources using the Simple Back-Projection method is analysed.

Finally, both conclusions and future work are presented in Chapter 6.

Chapter 2

Instrumentation and methods

The instrumentation and the main methods used in the thesis are described in this chapter. First the experimental material, such as detectors and digital data acquisition system, is described. The methods to determine the position of interaction, attenuation coefficient, energy deposited, energy resolution and position resolution are also described. The thesis describes two experimental measurement campaigns in laboratory conditions in order to characterize the CsI(Tl) scintillator bars and to validate Monte Carlo simulations. The experimental set up together with the geometries defined in the Monte Carlo simulations are explained in this chapter. The Monte Carlo simulations were performed by using the PENELOPE/penEasy code. The adaptation of PENELOPE/penEasy simulations is also given.

The characteristics of a Compton camera, the reconstruction algorithm, the selection of events according to their deposited energy and the parameters that evaluate the performance of a Compton camera, i.e. efficiency, angular resolution and image resolution are described in this chapter. Finally, the methodology for designing the Compton camera and its characterization are briefly commented on in the last sections of this chapter, which are then fully developed in Chapters 4 and 5, respectively.

2.1 CsI(Tl) scintillator bars

Two identical CsI(Tl) scintillator bars with dimensions of $1.2 \times 1.2 \times 10$ cm^3 were purchased (see Fig. 2.1). Detectors were assembled by the Scionix[1] company. The company treated the crystals superficially and wrapped them with special reflective material in order to

---

[1] https://scionix.nl/

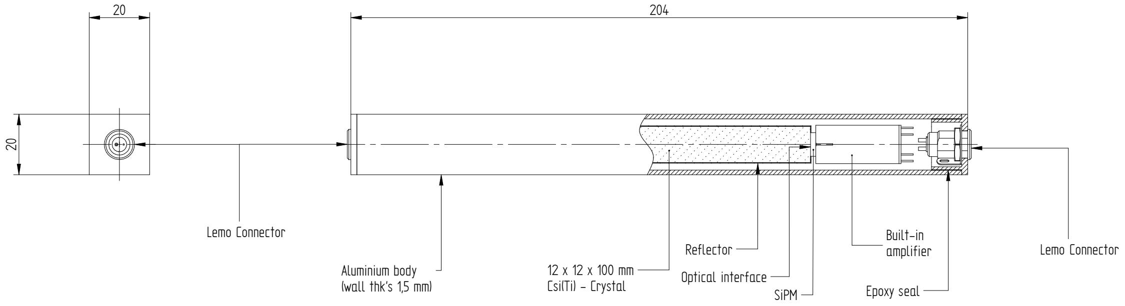

Figure 2.1: Scheme of the $1.2 \times 1.2 \times 10$ cm^3 Cs(Tl) coupled to both sides of the SiPM with the bias generator/preamplifier detector.

obtain optimal position measurements according to results from previous studies (MacLeod et al., 2014). The CsI(Tl) scintillator bars were coupled to two J series SENSL Silicon photomultipliers (SiPMs) with an active area of 1.2×1.2 cm^2. Each SiPM was provided with a bias generator and preamplifier. The scintillator and SiPMs are covered by a 1.5-mm-thick, square-shaped aluminium housing. The final size is $2 \times 2 \times 20.4$ cm^3. The total weight of each detector is 158 g. The cost of each detector was around 2000 €.

Considering that the Compton camera should be affordable, portable and rugged in order to be mounted on a UAS, CsI(Tl) scintillation materials were chosen. CsI(Tl) is less fragile than NaI(Tl), which means that it is more resistant to thermal and mechanical shocks (Knoll, 2000). It should also be pointed out that size and weight are important parameters in the selection criteria. In this context, the use of SiPMs is much better than PMTs because the former has a more compact size than the latter. In addition, SiPMs perform better with the wavelength light spectrum emitted by the CsI(Tl) than PMTs. SiPMs are solid-state photodetectors, which makes them more rugged than PMTs and they do not need a high-voltage supply. Their time response is comparable to the PMT, so they can be used in coincidence applications. Figure 2.2 shows the signals from both SiPMs obtained with an oscilloscope connected to one of the detectors. The time constant, τ, was found to be between 2.4 and 2.6 μs.

2.2 Digital data acquisition system (DDACQ)

The DDACQ is based on VME digitizers from the Struck Innovative Systeme[2] company. The digitizer employed is the SIS3316 Desktop Digitizer (see Fig. 2.3), which has 16

---

[2] http://www.struck.de/

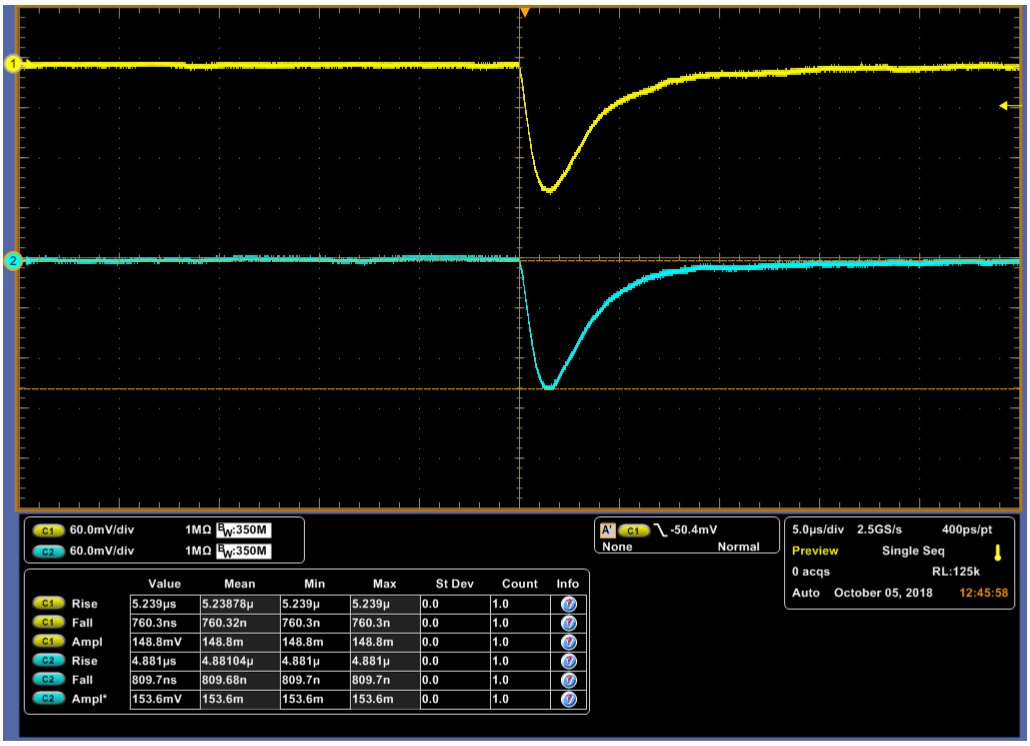

C1 60.0mV/div 1MΩ BW:350M
C2 60.0mV/div 1MΩ BW:350M

A' C1 ╲ -50.4mV
None Normal

5.0µs/div 2.5GS/s 400ps/pt
Preview Single Seq
0 acqs RL:125k
Auto October 05, 2018 12:45:58

	Value	Mean	Min	Max	St Dev	Count	Info
C1 Rise	5.239µs	5.23878µ	5.239µ	5.239µ	0.0	1.0	?
C1 Fall	760.3ns	760.32n	760.3n	760.3n	0.0	1.0	?
C1 Ampl	148.8mV	148.8m	148.8m	148.8m	0.0	1.0	?
C2 Rise	4.881µs	4.88104µ	4.881µ	4.881µ	0.0	1.0	?
C2 Fall	809.7ns	809.68n	809.7n	809.7n	0.0	1.0	?
C2 Ampl*	153.6mV	153.6m	153.6m	153.6m	0.0	1.0	?

Figure 2.2: Signals from both SiPMs from one of the detectors obtained with a oscilloscope.

Figure 2.3: Photo of the SIS3316 Desktop Digitizer.

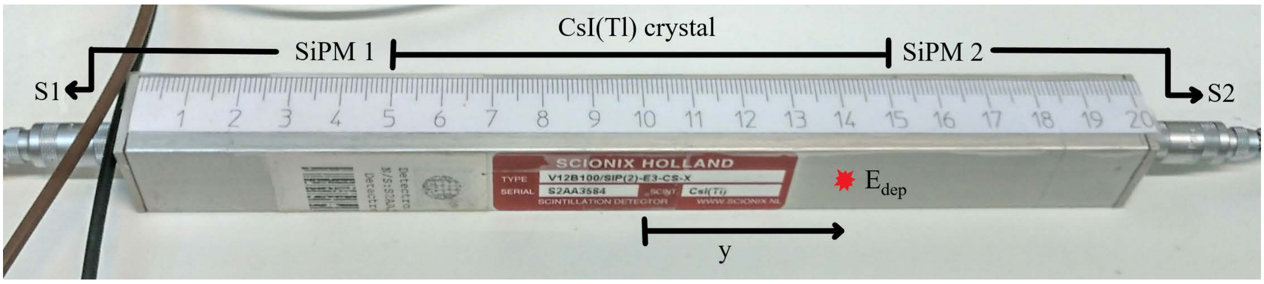

Figure 2.4: Photo of a CsI(Tl) scintillator bar with two SiPMs. The positions of the crystal and the SiPMs are indicated. Signals from the SiPMs, S_1 and S_2, are obtained when a γ-ray interacts in the scintillator. The interaction takes place at a distance y from the bar centre and it deposits energy, E_{dep}.

independent signal channel inputs. The software used for the data acquisition system is called GasificTL (Agramunt et al., 2013, 2016), which was developed by the Gamma and Neutron Spectrometry group at IFIC-Valencia. The DDACQ software is able to provide both the amplitude and timestamp of signals with a resolution of 16 ns. Events can be analysed a posteriori by using the timestamp information.

2.3 Location and energy deposited of γ-ray interactions

When a γ-ray interacts in the scintillator bar, light quanta are yielded. This light is attenuated on its way to the photo-sensors due to the inherent attenuation in the crystal and its surface finish. It is necessary that the scintillation light undergoes optimum attenuation along the bar in order to distinguish the position of γ-ray interactions. This can be done by modifying the surface finish in order to lower the light intensity reaching the photo-sensors (Charalambous et al., 1984). For example, by using different coatings and wrappings (Vilardi et al., 2006), or polishing or degrading the crystal surface (Kaloskamis et al., 1993; MacLeod et al., 2014). This latter case might be combined with the use of optical reflectors to obtain the desired position and energy resolutions.

If the crystal surface is ideally polished, light undergoes total internal and specular reflection, while if the surface is rough, the generated light suffers diffusive reflections. The former case provides less information about the position of γ-ray interactions than the latter. The signals can be considered to be exponentially attenuated along the bar when scintillator bars have a diffuse surface. After a γ-ray interaction occurs at a distance y from the bar centre, as Fig. 2.4 shows, the signals from both SiPMs, S_1 and S_2, are proportional to the number of photons detected in each photo-sensor and the signals can be represented as follows (Carter et al., 1982).

$$S_1 \propto P\frac{N_{ph}}{2}e^{-\alpha\left(\frac{L}{2}+y\right)} \tag{2.1}$$

$$S_2 \propto P\frac{N_{ph}}{2}e^{-\alpha\left(\frac{L}{2}-y\right)} \tag{2.2}$$

Where α [cm^{-1}] is the attenuation coefficient per unit length, L [cm] the length of the crystal, N_{ph} the number of light photons generated in the crystal and P is the photon detection efficiency of SiPMs. The position along the bar of the γ-ray interaction is denoted by y [cm]. The origin of the y axis, i.e. $y = 0$, is located at the centre of detectors, as Fig. 2.4 shows. Positions with $y > 0$ indicate interactions between the bar centre and SiPM 2.

Eqs. 2.1 and 2.2 consider a similar photon detection efficiency for both SiPMs and a similar attenuation coefficient in both directions. The attenuation coefficient includes loss of light in the bulk of the material and loss of light due to collisions with the surface. Therefore, it depends on the optical properties of the scintillator, its surface finish, the coupling between the SiPMs and the scintillator and the properties of the SiPMs.

The interaction point of the γ-ray, y, can be calculated with the ratio of 2.1 and 2.2:

$$y = \frac{1}{2\alpha}\ln\left(\frac{S_2}{S_1}\right) \tag{2.3}$$

The position of interaction in the crystal cross-section is unknown. The position is calculated with random numbers generated by a uniform distribution.

The energy deposited in the scintillators is proportional to the amount of scintillation light generated in the crystal. This magnitude was calculated by summing both signals, $S_1 + S_2$, which can be considered independent of position.

In order to be able to calculate the position and energy of a γ-ray event, a characterization of detectors must be done. In the following sections the calculation of the attenuation coefficient, the determination of both energy and position resolutions, and the optimization of the parameter αL are discussed.

2.3.1 Determination of the attenuation coefficient

The attenuation coefficient, α, can be calculated with Eq. 2.3 by carrying out measurements with a collimated source at different positions along the bar, y. The attenuation coefficient is calculated by fitting measurements of S_2/S_1 for different positions of the collimated source, y, to an exponential function, as Eq. 2.4 shows. This procedure should be done experimentally and must be performed for each detector.

$$\frac{S_2}{S_1} = e^{2\alpha y} \tag{2.4}$$

2.3.2 Energy resolution

Energy resolution can be expressed as (Syntfeld-Kazuch et al., 2006)

$$\left(\frac{FWHM}{E}\right)^2 = \left(\frac{FWHM}{E}\right)^2_{st} + \left(\frac{FWHM}{E}\right)^2_{int} + \left(\frac{FWHM}{E}\right)^2_{t} \tag{2.5}$$

The first term of the right-hand side considers the statistical factors related to the number of detected photons, the second is the intrinsic resolution that is a property of the crystals themselves. It is mainly associated with the non-proportional response of the scintillator to γ-ray energy. The third term is the transfer resolution related to the variations of light collection. The transfer resolution is not considered because its value is small compared to the statistical and intrinsic energy resolutions.

The statistical contribution, $\left(\frac{FWHM}{E}\right)^2_{st}$, is estimated by applying propagation of uncertainties to $\sqrt{S_1 S_2}$ obtaining the following equation (Carter et al., 1982):

$$\left(\frac{FWHM}{E}\right)_{st} = 2.35\frac{\sigma_E^{st}}{E} = \frac{2.35}{\sqrt{N_{ph}P}} e^{\alpha L/4}\sqrt{\cosh(\alpha y)} \tag{2.6}$$

Note that the energy deposited, E_{dep}, can be obtained from $\sqrt{S_1 S_2}$, since $\sqrt{S_1 S_2} \propto N_{ph} \propto E_{dep}$. It was assumed that signals, S_1 and S_2, follow Poisson statistics, i.e. $\sigma_{S_1} = \sqrt{S_1}$ and $\sigma_{S_2} = \sqrt{S_2}$.

The intrinsic component of the energy resolution was determined based on data shown in the work presented in Syntfeld-Kazuch et al. (2006). This work studied the intrinsic resolution of CsI(Tl) crystals with different concentrations of the Tl activator and used two shaping time constants, τ, of 3 and 12 μs. They found that intrinsic energy resolution is independent for Tl concentration higher than 0.05 mole%. Differences between intrinsic resolutions from crystals with different concentration doping are a lot more important for energies lower than 20 keV.

The signals obtained with the two purchased CsI(Tl) scintillator bars have a time constant of 2.4−2.6 μs. Therefore, the intrinsic resolution for time constants of 3 μs obtained in Syntfeld-Kazuch et al. (2006) was used for further calculations. The Tl concentration is not an important factor in our application because low deposited energies are not considered in the experimental measurements since an experimental threshold was set to 20 keV in order to reduce the noise.

Data obtained in Syntfeld-Kazuch et al. (2006) for a Tl concentration of 0.01 mole% and a time constant of 3 μs are separated into three sections according to deposited energy: 20keV$\leq E_{dep} <$ 30 keV, 30 keV $\leqslant E_{dep} <$ 510 keV and $E_{dep} \geq$ 510 keV. Each section was fitted to a function $\left(\frac{FWHM}{E}\right)^2_{int} = a + \frac{b}{\sqrt{E}}$, as Eqs. 2.7, 2.8 and 2.9 show.

$$\left(\frac{FWHM}{E}\right)^2_{int} [\%] = (-11 \pm 1) + \frac{(108 \pm 4)}{\sqrt{E[keV]}} \tag{2.7}$$

$$\left(\frac{FWHM}{E}\right)^2_{int} [\%] = (5.4 \pm 0.4) + \frac{(21 \pm 3)}{\sqrt{E[keV]}} \tag{2.8}$$

$$\left(\frac{FWHM}{E}\right)^2_{int} [\%] = (0.6 \pm 0.2) + \frac{(134 \pm 7)}{\sqrt{E[keV]}} \tag{2.9}$$

2.3.3 Position resolution

When a collimated source is placed at a certain distance from the bar centre, the position of interaction, y, is calculated with Eq. 2.3. The position resolution can be determined by calculating the standard deviation of the position distribution, σ_y. It can be calculated experimentally, however, for those energies that are not measured directly, σ_y can be determined through the energy resolution as follows.

The statistical component of the standard deviation of position, σ_y^{st}, is calculated by applying propagation of uncertainties to Eq. 2.3 and assuming that signals S_1 and S_2 follow Poisson statistics, i.e. $\sigma_{S_1} = \sqrt{S_1}$ and $\sigma_{S_2} = \sqrt{S_2}$ (Carter et al., 1982):

$$\sigma_y^{st} = \frac{1}{\alpha\sqrt{N_{ph}P}} e^{\alpha L/4} \sqrt{\cosh(\alpha y)} \tag{2.10}$$

The equation that relates the statistical standard deviation of position, σ_y^{st}, and the statistical standard deviation of energy, σ_E^{st}, is obtained with Eqs. 2.6 and 2.10:

$$\sigma_y^{st} = \frac{1}{\alpha}\frac{\sigma_E^{st}}{E} \tag{2.11}$$

According to MacLeod et al. (2014), position resolution is roughly equal to its statistical component. Using Eqs. 2.5 and 2.11, the position resolution can be written as

$$\sigma_y \approx \sigma_y^{st} = \frac{1}{\alpha}\sqrt{\left(\frac{\sigma_E}{E}\right)^2 - \left(\frac{\sigma_E^{int}}{E}\right)^2} \tag{2.12}$$

2.3.4 Optimization of the parameter αL

If $\alpha \to \infty$, it means that no light is transmitted and, therefore, no light would reach the end of the bars, where the SiPMs are located. On the other hand, if $\alpha \to 0$, there is no attenuation in the crystal and all the generated light will be detected. In both cases, it is not possible to determine the position of interaction, y. Therefore, an optimum attenuation coefficient between 0 and ∞ should be determined in order to optimize position resolution. It was found that an increase in the attenuation coefficient improves the position resolution, but also leads to a worse energy resolution due to the decrease of detected light (Kaloskamis et al., 1993). In order to obtain a good position resolution without considerably degrading the energy resolution, an optimization of αL was done by MacLeod et al. (2014). This optimization was carried out with Monte Carlo simulations for NaI(Tl) scintillator bars. The study shows how different surface treatments affect the attenuation coefficient and how this, when rubbed down with sandpaper in the longitudinal direction, improved the position resolution. An optimum value of $\alpha L \approx 1$ was found for which the position resolution was found to be four times better than for polished scintillators, while there was a 20% worsening in energy resolution (Boyle et al., 2011).In addition, it was found that position resolution and energy resolution are independent of the position of gamma-ray interactions when $\alpha L \approx 1$. Therefore, the Scionix company was instructed to treat the surfaces of the scintillator bars purchased in order that $\alpha L \approx 1$.

2.4 Experimental measurements

2.4.1 Characterization of detectors

Experimental measurements using a ^{137}Cs isotropic point source with an activity of 185 kBq (19/10/2018) were performed at the Nuclear Instrumentation Laboratory (LIN) of the Technical University of Catalonia (UPC) in order to characterise both detectors. The attenuation coefficients, energy resolution and position resolution were determined for an energy of 662 keV.

The ^{137}Cs point source was collimated with a lead brick with a 3.5-mm diameter circular opening and a thickness of 8.4 cm. The collimated source was placed at 11 positions along the detector, with a separation between measurements of 1 cm. Data were acquired for about one hour at each position of the collimated source. The DDACQ recorded the amplitude of the signals, S_1 and S_2, together with their corresponding timestamp during experimental measurements. In order to accept a pair of signals (S_1 and S_2), their energy should be above a threshold of 20 keV in order to reduce noise and they should be in coincidence. In order to determine the optimum width of the coincidence window, the timestamps from both signals are compared. A histogram of their differences is shown in Fig. 2.5. It shows the distribution of the number of coincident events as a function of the difference of the two timestamps recorded by S_1 and S_2. Therefore, the probability of accepting signals, S_1 and S_2, from the same γ-ray interaction within a difference of the timestamps of 500 ns guarantees that almost all the coincidence events are registered and the probability to register events from different gamma-rays as one gamma ray is low. In the case that a pair of signals are accepted, the position of interaction and energy deposited were calculated by combining the signals from the two SiPMs.

2.4.2 Compton camera based on two scintillator bars

Measurements with a simple Compton camera consisting of two CsI(Tl) scintillator bars were done at the Calibration and Dosimetry Laboratory (LCD) of the Institute of Energy Technologies (INTE) of the Technical University of Catalonia (UPC). One of the CsI(Tl) detectors acts as a scatterer and the other as an absorber. The distance between the detector surfaces was 1.5 cm. The source used was ^{137}Cs with an activity of 299 MBq on 03/03/2020. The distance between the surface of the scatter detector and the source was 5 m. Figs. 2.6

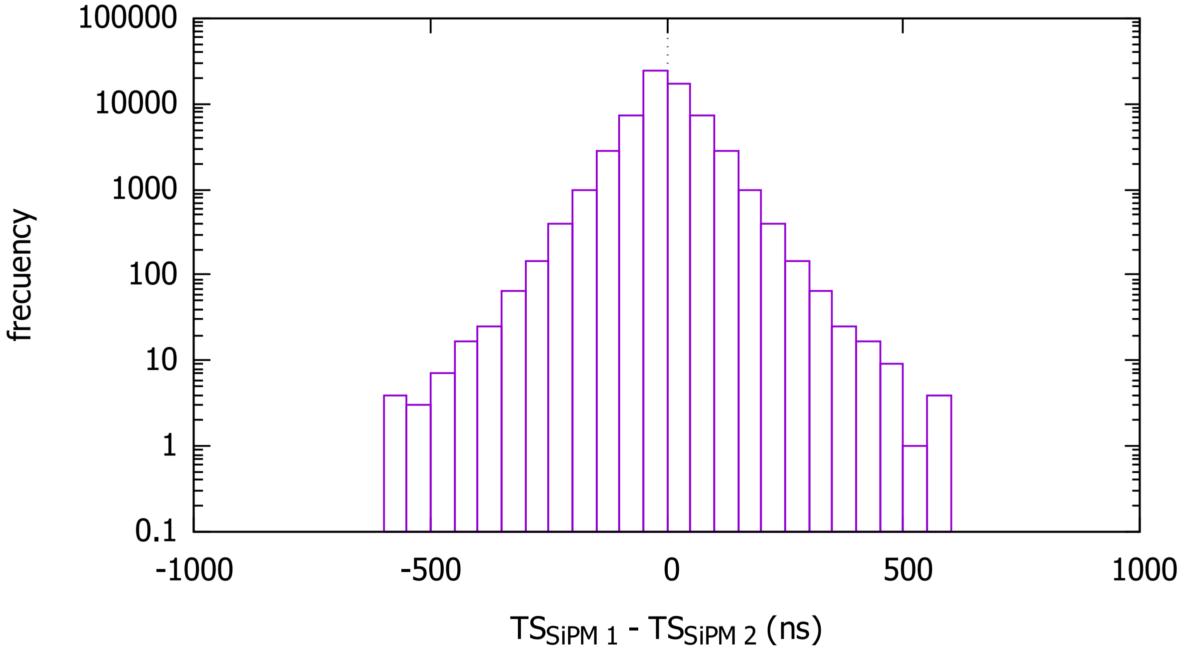

Figure 2.5: Histogram of the difference between the Timestamp of both signals.

and 2.7 show the experimental configuration.

As we can see in Figure 2.7, detectors are placed on a plate with rotational movement. In order to reduce the detection of scattered γ-rays from the plate, detectors are placed over a bridge structure. As the source cannot be moved, detectors will be rotated in order to simulate different angles of the source position. Three irradiations were performed lasting 20 min. The Compton camera was placed at 0°, 20° and $-20°$.

The DDACQ recorded the amplitude of the four signals coming from both detectors with their corresponding timestamps. A Compton camera looks for those γ-rays that interact via Compton scattering and then the scattered photons are fully absorbed in the absorber via the photoelectric effect. These kinds of events are selected according to their timestamp. To this end, signals from each detector (S_1 and S_2) must be in coincidence, as was explained in Section 2.4.1. When a pair of signals are found to be in coincidence, the average timestamps associated with S_1 and S_2 are calculated. These average timestamps are then compared in order to determine which events from different detectors are in coincidence (see Fig. 2.8). The flat regions with differences lower than 0 and greater than about 460 ns correspond to unrelated events. Therefore, those events with a difference of average timestamps greater than 0 and less than or equal to 460 ns are accepted.

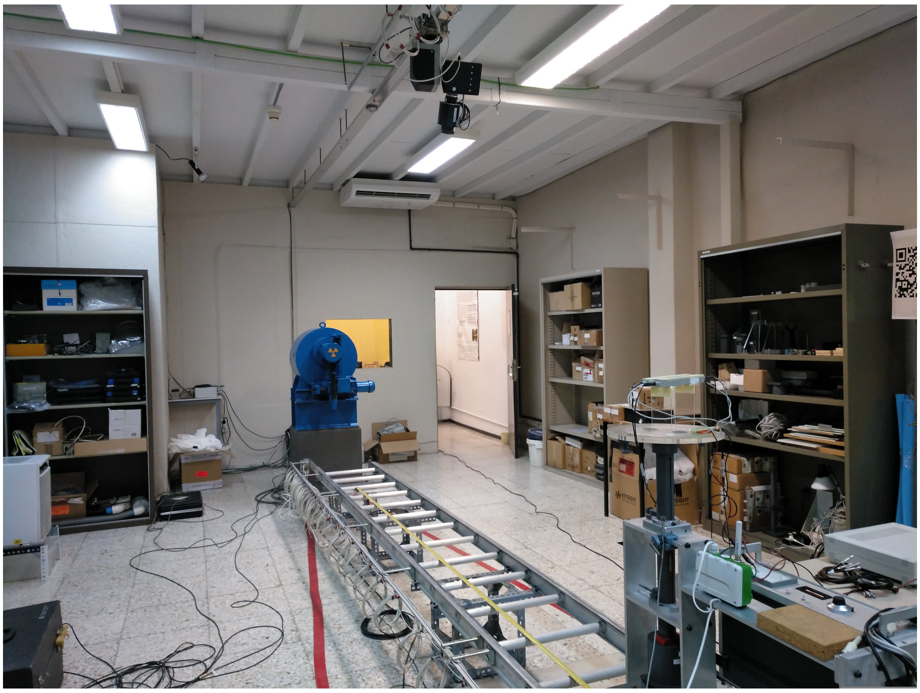

Figure 2.6: Photo of the experimental configuration at LCD. Detectors are placed on top of a rotary plate, which is 5 m away from the source.

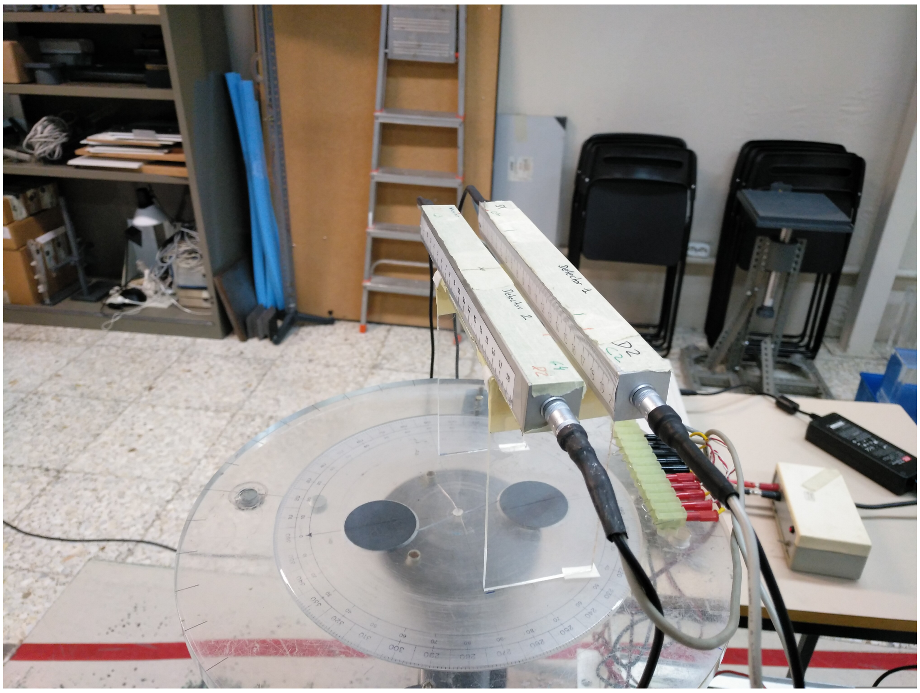

Figure 2.7: Two CsI(Tl) scintillator bars are placed on top of a methacrylate structure, which is on a rotary plate. The distance between the surfaces of both detectors is 1.5 cm.

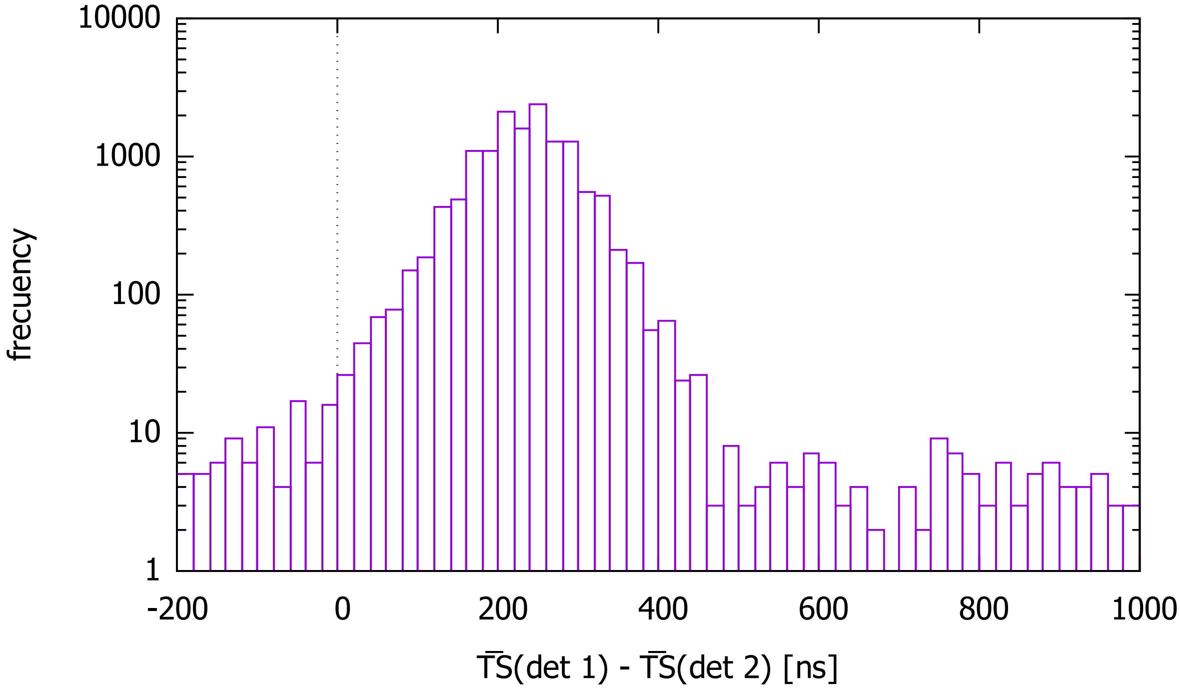

Figure 2.8: Histogram of the difference between the average timestamps of both detectors. When a pair of signals are validated, the average value of their timestamps (TS) is calculated. $\overline{TS}$(det 1) and $\overline{TS}$(det 2) represent the average value of timestamps for detector 1 and detector 2, respectively.

2.5 Monte Carlo simulations with PENELOPE/penEasy code

Monte Carlo simulations with the PENELOPE/penEasy code (Sempau et al., 2011) are used to design a Compton camera based on scintillator bars. PENELOPE (Salvat, 2015) is a Monte Carlo simulation package that describes coupled electron-photon transport for arbitrary geometries and materials. PENELOPE is an acronym for PENetration and Enegy Loss of Positrons and Electrons. It is freely distributed by the OECD Nuclear Energy Agency Data Bank[3]. The penEasy (Sempau et al., 2011) code is a general-purpose main program for PENELOPE. It is important to note that penEasy is a modular code that facilitates the modification of routines to user needs without having to change the main program. The PENELOPE/penEasy code, which was fully developed in the EU, is both free and open source; it can be modified, adapted, extended and exploited without requiring explicit permission from the authors or a license.

Before designing a Compton camera based on long scintillator bars with Monte Carlo simulations, PENELOPE/penEasy simulations should be validated. This task is carried out

---

[3] http://www.oecd-nea.org/databank/

by comparing Monte Carlo simulations with the basic experimental irradiation described in Sections 2.4.1 and 2.4.2. In the following sections, the considerations taken in Monte Carlo simulations are described and the geometries defined in PENELOPE/penEasy are shown.

2.5.1 Adaptation of PENELOPE/penEasy

The outcome of PENELOPE/penEasy simulation should provide a file with the magnitudes that are needed for the Compton imaging algorithm. Therefore, the penEasy code was adapted in order to provide deposited energies and position interactions of the simulated γ-rays in a separate file. These two magnitudes are written in a file when γ-rays interact in coincidence both in the scatter and absorber layers.

In the simulations the transport of electrons was turned off because it would lengthen the simulation time. As a result, energy is deposited at a point after a γ-ray interaction. However, this is not the case in experimental measurements since deposited energy is distributed in a certain volume. In order to consider this factor and other statistical factors, energy and position resolutions should be introduced in simulations. The energy and position along the bar obtained with simulations were spread out by assuming that their resolutions follow a Gaussian distribution with standard deviations of σ_E and σ_y, respectively. The standard deviations σ_E and σ_y were calculated experimentally for a deposited energy of 662 keV when detectors were irradiated with a collimated ^{137}Cs source, as described in Section 2.4.1. For other deposited energies, the position standard deviation, σ_y, was calculated with Eq. 2.12; and the energy standard deviation was calculated by assuming that $\sigma_E = w/\sqrt{E}$, where w is a constant calculated with the experimental measurements. It is important to point out that the use of long scintillator bars does not provide information about the position of interaction in the cross-section of the crystals. These two position coordinates, x and z, are recalculated using random numbers generated by a uniform distribution in the cross-section of the crystal.

When a simulated γ-ray undergoes scattering or a photoelectric effect, there is no production of electrons and the energy is absorbed at the point of interaction. For example, after Compton scattering, the energy will be deposited at the interaction point and the scattered γ-ray will be the only outcome. This later γ-ray may again interact in the same crystal, through another Compton scattering or the photoelectric effect. Considering that several interactions in the same crystal give a single interaction in experimental measurements, the position of interaction associated with several simulated interactions in the same crystal is estimated with a weighted mean, as Eq 2.13 shows. Note that the production of photons in a scintillator is proportional to the energy deposited by the γ-ray.

$$\overline{y} = \frac{\sum y_i E_i}{\sum E_i} \tag{2.13}$$

Where y_i is the position of interaction i and E_i is the deposited energy of interaction i. In addition, the experimental threshold used to reduce noise, which does not allow events with $E \leq 20$ keV, was also included in simulations.

2.5.2 Geometry

Two groups of simulations were performed, which tried to reproduce the experimental measurements described in Sections 2.4.1 and 2.4.2. In the following sections the two geometries defined in PENELOEPE/penEasy simulations are described.

Geometry of individual detectors

The CsI(Tl) scintillator detector was defined in the PENELOPE/penEasy simulations according to the purchased detectors described in Section 2.1. Fig. 2.9 (bottom) shows an image of the cross section of a single detector. The image was obtained with the GVIEW2D tool included in the PENELOPE code. The materials of the detector components are specified in parentheses in Fig. 2.9.

In order to emulate the experimental measurements used to characterize the detectors (Section 2.4.1), a lead collimator was defined above the detector, as Fig. 2.9 (top) shows. The collimator defined in the simulated geometry has a circular opening of 3.5 mm and a thickness of 8.4 cm, as in the case of the experimental collimator. An isotropic ^{137}Cs point source is simulated at the top of the collimator.

Geometry of a simple Compton camera

The geometry defined in the PENELOPE/penEasy simulations consists of two identical CsI(Tl) scintillator bars. Each detector was defined in the geometry following the purchased CsI(Tl) detector, as described in Section 2.1. A cross section of the detector is shown in Fig 2.9 (bottom). The distance between detectors is 1.5 cm, as in the case of experimental

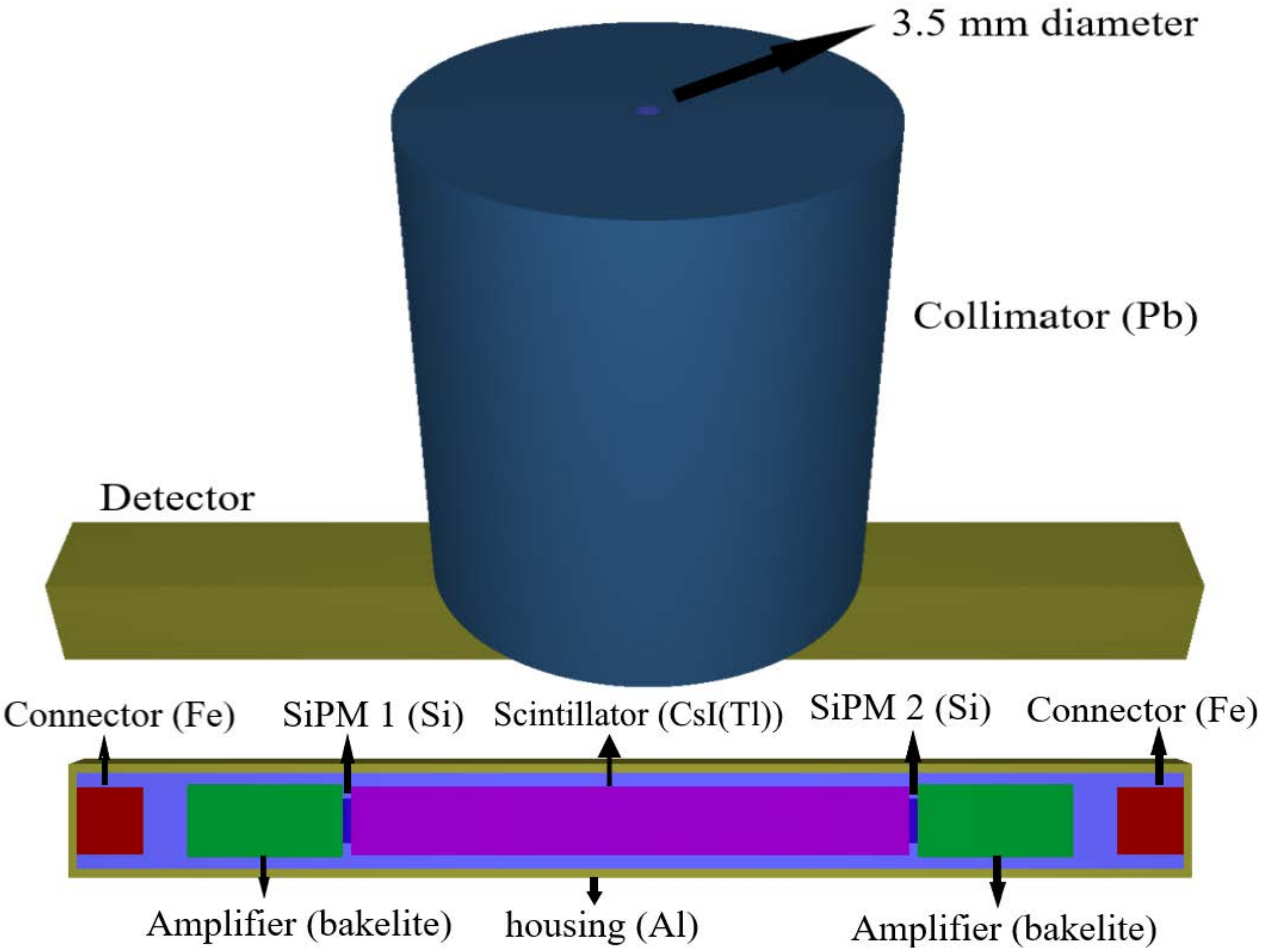

Figure 2.9: Geometry defined in the PENELOPE/penEasy simulations. Above: CsI(Tl) detector with a 3.5 mm collimator placed at the bar centre. Below: Cross section of a single detector. A SiPM, an amplifier and a connector have been defined on each side of the CsI(Tl) crystal. The enclosure is made of aluminium with a thickness of 1.5 mm. The materials are specified in parentheses. The GVIEW2D tool included in the PENELOPE code was used in order to obtain an image of the geometry.

measurements (see Section 2.4.2). An isotropic ^{137}Cs point source is placed at a distance of 500 cm from the surface of the nearest detector. In the experimental measurements the ^{137}Cs point source of the LCD is within a stainless-steel capsule, which is located in the lead shielding of the LCD. Due to the fact that only the events that deposit 662 keV when an interaction occurs in both detectors in coincidence are considered, there is no need to simulate the entire capsule of the source and surrounding material of the LCD, such as the irradiator shielding, the floor and the methacrylate structure that supports the detectors. Just a sheet of 3 mm thickness was defined in front of the source (Vargas et al., 2015). The sheet material defined in the simulation was iron. Both detectors and the source were surrounded by air.

2.6 Compton camera

Gamma-rays with energy up to 1 GeV mainly interact in matter through the photoelectric effect, coherent or Rayleigh scattering, incoherent or Compton scattering or electron-positron pair-production.

The photoelectric effect consists of the absorption of a gamma-ray with energy E_γ and an emission of an electron with energy $E_e = E_\gamma - U_i$, where U_i is the ionisation energy of shell i. The photoelectric effect is more likely to occur when gamma-ray energies are low and when the absorbent material has a high atomic number, Z.

The absorption of a gamma-ray in the vicinity of a massive particle can create an electron-positron pair. When this positron is annihilated, two photons of 511 keV are emitted. The direction of these two photons is independent of the direction of the incident γ-ray. Thus, this process cannot be used to determine the source position. The minimum energy of γ-rays to produce an electron-positron pair in the field of a nucleus is $2m_ec^2$.

In coherent or Rayleigh scattering, the γ-ray is scattered by a bound atomic electron without energy being transferred. The energies of the incident and scattered γ-rays are the same. However, if part of the energy of the γ-ray is transferred to the electron, which is ejected from the atom with a certain energy, the process is called incoherent or Compton scattering. If the electron is assumed to be free and at rest, the energy of the scattered γ-ray, E_2, is obtained by applying the laws of energy and momentum conservation (see Fig. 2.10):

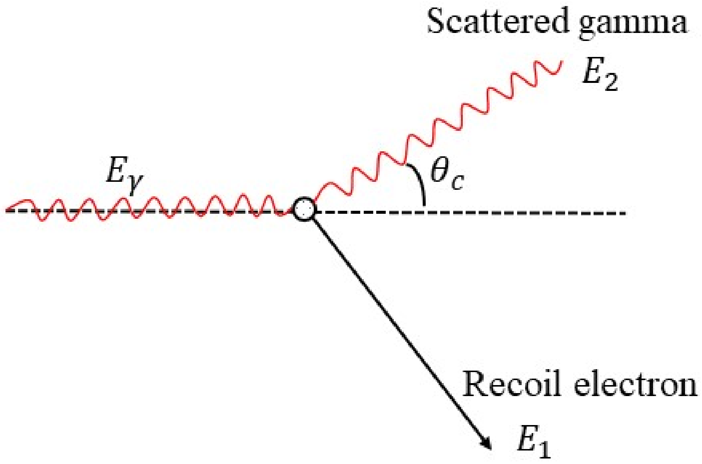

Figure 2.10: Diagram of the Compton scattering. A γ-ray with energy E_γ is scattered by a bound electron. The outcome of the interaction is a scattered γ-ray with energy E_2 and a recoil electron with energy E_1.

$$E_2 = \frac{E_\gamma}{1 + k(1 - \cos\theta_c)} \tag{2.14}$$

Where E_γ is the energy of the γ-ray incident, θ_c is the scattering angle and $k = E_\gamma / m_e c^2$. Compton scattering is likely to occur for the CsI(Tl) material for energies greater than 300 keV up to several MeV.

The Compton camera uses Compton scattering to determine the initial direction of the γ-ray. As was explained above, a Compton camera usually consists of two layers of detectors, called the scatter and absorber layers (see Fig. 2.11). Ideally, γ-rays should interact once in the scatter layer via Compton scattering and the scattered photon should be absorbed in the absorber via the photoelectric effect. Detectors must be both energy and position sensitive in order to determine the deposited energies and the position of interaction in both layers. Thus, the energy of the recoil electron, E_1, and the energy of the scattered photon, E_2, are determined. The scattering angle, θ_c, can be calculated with the Compton equation, as Eq. 2.15 shows.

$$\cos\theta_c = 1 - m_e c^2 \left(\frac{1}{E_2} - \frac{1}{E_1 + E_2} \right) \tag{2.15}$$

Where,

$$E_\gamma = E_1 + E_2 \tag{2.16}$$

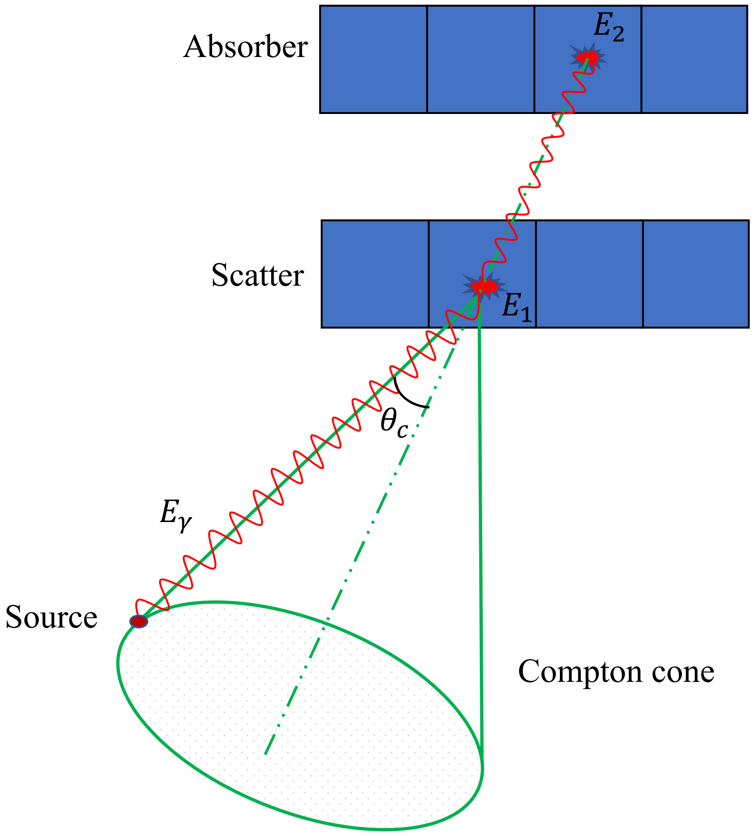

Figure 2.11: Schematic representation of a typical Compton camera. It consists of two layers of detectors: the scatter and the absorber layers. A gamma-ray emitted from a source interacts in the scatter layer via Compton scattering. The scattered photon is completely absorbed in the absorber. The surface of a cone, called a Compton cone, indicates where the source might be found. The opening angle of the cone is $2\theta_c$ and its axis is the straight line that joins the two interaction points.

Ideally, the source can be found on the surface of a cone with an opening angle of $2\theta_c$ (see Fig. 2.11), which is called a Compton cone. Its axis is defined by the interaction points of the Compton scattering and the photoelectric effect. Its vertex is set at the interaction point of the Compton scattering. Each pair of validated events provide a Compton cone. Since the source can be located at any point of the Compton cone, the source position is obtained by overlapping a certain number of Compton cones in the image plane. This method is called the simple back-projection method (Wilderman et al., 1997).

The positions of interaction in the scatter and absorber detectors are denoted by (x_1, y_1, z_1) and (x_2, y_2, z_2), respectively. The intersection of the Compton cone with the image plane $z = z_0$ is given by

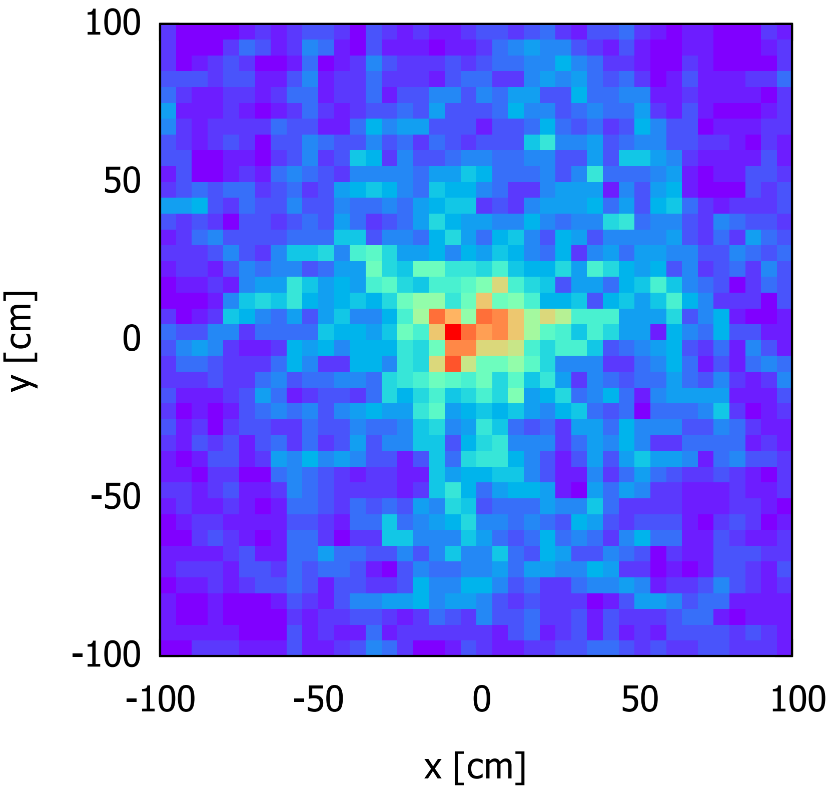

Figure 2.12: Image of a ^{137}Cs source obtained with the List mode back-projection method. The number of ellipses used were 100 cones.

$$[n_x(x-x_1)+n_y(y-y_1)+n_z(z-z_1)]^2 = (\cos\theta_c)^2[(x-x_1)^2+(y-y_1)^2+(z-z_1)^2] \tag{2.17}$$

where (n_x, n_y, n_z) is the unit vector of the cone axis. The vertex of the cone is defined by the point (x_1, y_1, z_1).

The image plane is divided into pixels by a series of grid lines. The reconstruction method used is based on the intersection of the grid lines from the image plane with the ellipse calculated using Eq. 2.17. When an ellipse passes over a pixel, which is determined by the intersection of the grid lines with the ellipse, the intensity of this pixel increases by one unit. It is a simple and fast algorithm that does not need a huge amount of memory. Fig. 2.12 show an image reconstructed with the method using 100 ellipses for a ^{137}Cs source located at $(x=0, y=0)$.

The back-projection method has a fast response and, therefore it is convenient to be used in real time measurements. However, the images are more blurred than the images reconstructed using other more complex techniques. Due to its speed and simplicity, this method is used in the thesis.

Other more complex techniques for image reconstruction described in the literature are the Filtered back-projection algorithm and the List-mode Maximum Likelihood method. They can produce better images than the back-projection method. These two algorithms together with the simple back-projection method were compared by Xu et al. (2004). The Filtered back-projection algorithm is a technique that deconvolutes the blurring out of the simple back-projection image. This algorithm can also be applied event by event, so that it can also be implemented in real time measurements. It provides images with better resolution than those obtained with the simple back-projected method with a slightly higher computational cost. The List-mode maximum likelihood algorithm (Wilderman et al., 1998) is an interactive estimation-maximization algorithm that uses the back-projection method to calculate the coefficients of the response matrix. It uses the interactive technique Maximum Likelihood Expectation Maximization (MLEM), which requires an enormous matrix to evaluate the response of the imaging system. The List-mode maximum likelihood algorithm only calculates the matrix coefficients on the back-projection cone, which considerably reduces the stored data. This algorithm is usually run offline because it needs a considerable amount of computing resources.

In order to reduce noise in the images, coincident events should be selected according to their deposited energy. In the following section the energy windows applied in order to select events are described. Furthermore, the Compton camera parameters, such as efficiency, angular resolution and image resolution are also described.

2.6.1 Energy windows

Events should be selected according to their deposited energies in order to neglect those events that degrade images. First, those γ-rays that interact in the scatter and absorber layers in coincidence are chosen. The sum of the deposited energies of these two interactions must be within $E_\gamma \pm 3\sigma_E$, where E_γ is the energy of the incident γ-ray and σ_E is the energy standard deviation.

The γ-rays that interact first in the scatter layer, via one or several Compton scatterings, and then the scattered photons that subsequently interact in the absorber layer are called forward-scattering events (FSE). On the other hand, the γ-rays that interact first in the absorber via Compton scattering and scattered photons that subsequently interact in the

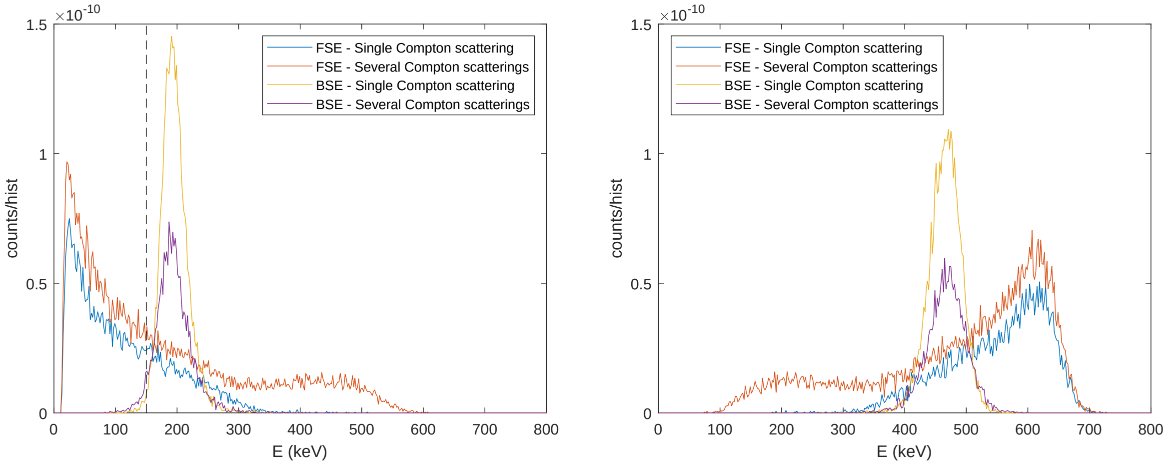

(a) Scatter layer

(b) Absorber layer

Figure 2.13: Energy deposited in the a) scatter layer and b) absorber layer when γ-rays interact in both layers and deposit a total energy of 662 keV. Forward scattering events (FSE) and backward scattering events (BSE) are plotted. Events are separated into those that interact only once in both layers (Single Compton scattering) from those that interact more than once in one or both layers (Several Compton scatterings). A Compton camera consisting of two CsI(Tl) scintillator bars of $1.2 \times 1.2 \times 10$ cm^3 is simulated. A source of ^{137}Cs was placed both in the centre and 5 m away from the scatter layer. The selected threshold (150 keV) is plotted with a black dashed line.

scatter layer via the photoelectric effect are called backward-scattering events (BSE). In order to achieve the best possible image, BSE should not be considered in the image reconstruction as far as possible because BSE contributes to degradation of the image (Xiaofeng et al., 2017). This requirement is achieved by applying an energy threshold in the deposited energy in scatter detectors.

In order to analyse the threshold energies, simulations with two and eight detectors were performed. Simulations of the two detectors were used to reproduce the experimental measurements described in Section 2.4.2. Simulations with eight detectors were done in order to both optimize and characterize the Compton camera. In the first case a source of 662 keV (^{137}Cs) was simulated, while in the second case sources of 364 keV (^{131}I), 662 keV (^{137}Cs), 1173 keV (^{60}Co) and 1332 keV (^{60}Co) were modelled. The thresholds defined in the scatter layers are determined in the following sections for the sources mentioned.

Two detectors

A Compton camera consisting of two CsI(Tl) scintillator bars separated by 1.5 cm was simulated in order to determine the threshold for a 662-keV (^{137}Cs) point source. An isotropic source ^{137}Cs was placed 5 metres away from the scatter detector. Fig. 2.13 shows the deposited energy in the scatter and absorber layers when γ-rays deposit a total energy of 662 keV summing both layers. Gamma-rays that interact once in each layer (Single Compton scattering) are separated from those that interact several times in one or both layers (Several Compton scatterings). Gamma-rays are also sorted according to the order of interaction, i.e. those gamma-rays that interact first in the scatter layer (FSE) are separated from those that interact first in the absorber layer (BSE). Paying attention to the deposited energy in the scatter detector (Fig. 2.13a), the BSE are concentrated at a peak of around 200 keV. Above this peak, gamma-rays mainly deposit energy through more than one Compton scattering when a source of 662 keV was simulated. These events might also degrade the image because information about the initial gamma-ray direction might be lost. Therefore, only those gamma-rays that deposit energies lower than 150 keV in the scatter layer are accepted for a source of 662 keV (^{137}Cs). This threshold is plotted in Fig. 2.13a using a black dashed line.

Eight detectors

In this section, sources of 364 keV, 662 keV, 1173 keV and 1332 keV are simulated by using a Compton camera consisting of eight detectors of $1.2 \times 1.2 \times 10$ cm^3 with four detectors in each layer. The separation between layers is 10 cm. Sources were placed both in the centre and 1 metre away from the scatter layer. The objective is to determine the threshold that is to be set in the scatter detector in order to disregard the γ-rays that interact first in the absorber layer and are fully absorbed in the scatter layer. This threshold depends on the energy of the incident γ-rays as can be observed in Fig. 2.14. Results are shown for (a) 364 keV, (b) 662 keV, (c) 1173 keV and (d) 1332 keV. Fig. 2.14 shows the deposited energy in the scatter detectors when gamma-rays deposit a total energy of E_γ between both layers. Gamma-rays that interact once in each layer are also separated from those that interact several times in either one or both layers. Gamma-rays are also sorted according to the order of interaction, i.e. BSE and FSE are counted separately.

As we can see in Fig. 2.14, the BSE are concentrated at a peak of around 200 keV, which is called the backscatter peak. Above this peak, γ-rays deposit energy through more than one Compton scattering when sources of 364 keV and 662 keV are simulated. These events might degrade the image because information about the initial gamma-ray direction might be lost. Therefore, only those γ-rays that deposit energies lower than 125 keV and 150 keV

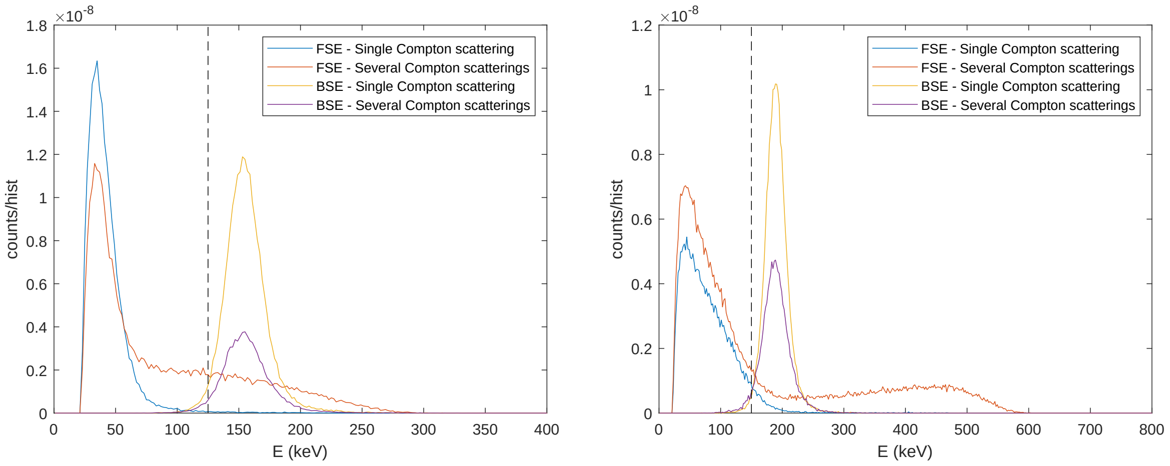

(a) 364 keV

(b) 662 keV

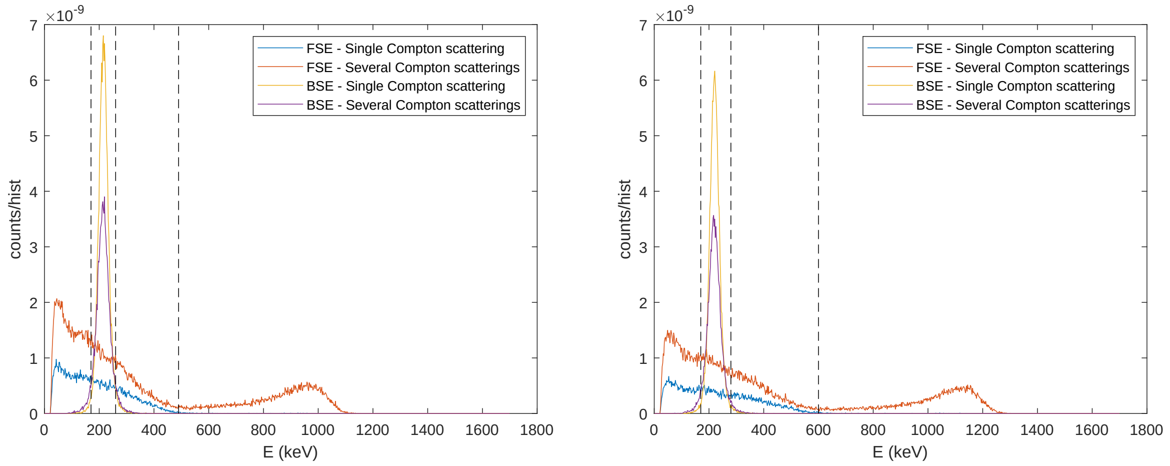

(c) 1173 keV

(d) 1332 keV

Figure 2.14: Energy deposited in scatter detectors when γ-rays interact in both layers and deposit a total energy of E_γ. Forward scattering events (FSE) and backward scattering events (BSE) are plotted. Events are separated into those that interact only once in both layers (Single Compton scattering) from those that interact more than once in one or both layers (Several Compton scatterings). Simulations were done with a Compton camera consisting of 8 CsI(Tl) detectors of $1.2 \times 1.2 \times 10$ cm^3. Results are shown for γ-ray sources of (a) 364 keV, (b) 662 keV, (c) 1173 keV and (d) 1332 keV, which were placed in the centre and 1 m away from the scatter layer. The selected threshold is plotted with a black dashed line. Events with energies (a) $E \leq 125$ keV, (b) $E \leq 150$ keV, (c) $E \leq 170$ keV; 260 keV$\leq E \leq 490$ keV and (d) $E \leq 170$ keV; 280 keV $\leq E \leq 600$ keV are selected in order to obtain the Compton cones.

in the scatter layer will be accepted for sources of 364 keV and 662 keV, respectively. These thresholds are plotted with black dashed lines in Fig. 2.14a and 2.14b, respectively.

On the other hand, when γ-rays of 1173 keV and 1332 keV are simulated, there are γ-rays that interact once in both layers above the backscatter peak. Therefore, events above this peak might provide important information about the position of sources. In order to include the events that interact once in both layers, two energy ranges were defined when γ-rays of 1173 keV and 1332 keV are emitted. These energy ranges, which are indicated in Fig. 2.14c and 2.14d with black dashed lines, are $E < 170$ keV and $260 < E < 490$ keV for γ-rays of 1173 keV; and $E < 170$ keV and $280 < E < 600$ keV for γ-rays of 1332 keV. Gamma-rays that deposit energies $E > 490$ keV for γ-rays of 1173 keV and $E > 600$ keV for γ-rays of 1332 keV are not considered.

2.6.2 Basic parameters of a Compton camera

The parameters used to determine the performance of a Compton camera, i.e., the efficiency, the angular resolution and the image resolution are described in the following sections.

Efficiency

The Compton camera efficiency is defined as the ratio between the selected events (Section 2.6.1) and the γ-rays emitted by the source. The efficiency depends on several factors:

- The distance of the source to the detector
- The field of view of the scatter layer from the source, i.e. the subtended solid angle of the scatter layer by the source. This solid angle should be as large as possible, which is achieved by enlarging the surface of the scatter layer
- Probability of Compton scattering in the scatter layer
- Probability that the scattered gamma-ray will escape from the scatter layer. This is related to self-absorption of photons in the material, which, in turn, depends on photon energy, as well as the material and thickness of the scatter detectors.
- Probability of the scattered photon to fall within the solid angle of the absorber. It depends on the Compton camera geometry. It can be maximized by reducing the distance between the scatter layer and absorber and maximizing the absorber surface.

- Probability that the scattered photon is completely absorbed through the photoelectric effect in the absorber. This depends on the photon energy and the atomic number, Z, of the absorber. It can be maximized by choosing a material with high Z and by increasing the absorber thickness.

Angular resolution

The angular resolution measurement (ARM) is defined as

$$ARM = \theta_c - \theta_{geo} \tag{2.18}$$

where θ_c is the scatter angle calculated with Eq. 2.15 and θ_{geo} is the angle determined geometrically from the positions of the two interaction points and the incident direction of the γ-ray.

Uncertainties in the determination of deposited energies and positions of interaction mean that the cone does not pass exactly over the source position. The ARM distribution is related to the minimum distance between the cone and the source position. It can be used to show the ability of the Compton camera to determine the position of the source. The Full Width at Half Maximum ($FWHM$) of the ARM distribution is a measurement of the angular resolution of the Compton camera. The angular resolution is affected mainly by uncertainties of the deposited energy and the position of γ-ray interactions.

The scattering angle, θ_c, is calculated with the measured energies using Eq. 2.15. Therefore, uncertainties in the determination of deposited energies cause uncertainties in the scattering angle. There are two contributions to the energy uncertainties: the energy resolution of detectors and Doppler broadening. The former depends on the detection material and electronics for signal processing. For example, inorganic scintillators have a worse energy resolution than semiconductor detectors. Doppler broadening is caused by the fact that in Compton scattering γ-rays interact with bounded electrons, which have a certain momentum. It depends on the material and on the γ-ray energy. For example, Doppler broadening might be an important contribution to the angular resolution for γ-rays with low energies in detectors with good energy resolution, such as semiconductor materials (Ordonez et al., 1997).

The axis of the Compton cone is defined by the points of γ-ray interactions. The vertex of the cone is placed at the γ-ray interaction position in the scatter detector. Uncertainties

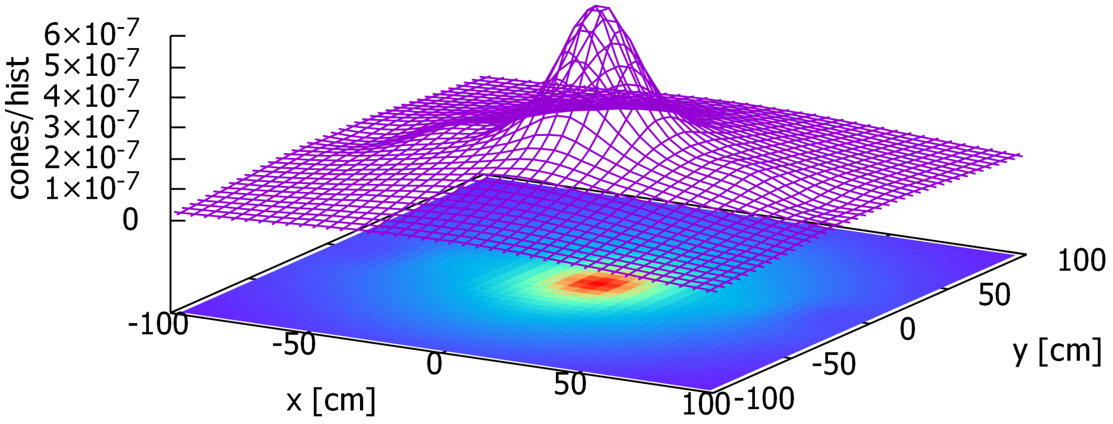

Figure 2.15: Image of a point source of 662 keV placed at the centre, 1 metre away from a Compton camera. The Compton camera consists of eight CsI(Tl) scintillator detectors. The image was obtained with the simple back-projection method. The z axis indicates the number of cones per history that pass over a certain pixel, where histories is the number of γ-rays simulated.

in the determination of these points may cause uncertainties in the determination of the Compton cone. The spatial resolution depends mainly on two factors: the statistical position resolution, which is calculated in Section 2.3.3, and the geometrical resolution, which depends on the size of detectors and location of detectors, such as the distance between the scatter and absorber layers. For example, the geometrical resolution can be improved by using small detectors and increasing the distance between the scatter and absorber layers (Ordonez et al., 1999). This will produce an improvement in the angular resolution of the Compton camera.

Image resolution

In order to analyse the uncertainty introduced by the simple-back projection method, the width of the distribution of counts in images was analysed. One example of an image obtained with the simple back-projection method is shown in Fig. 2.15. It was obtained by simulating a Compton camera consisting of eight CsI(Tl) scintillator detectors. A point source of 662 keV was placed at the centre, 1 metre away from the scatter layer. The width of the peak shown in Fig. 2.15 is calculated on both the x and y axes. To this end, a Region of Interest (ROI) was selected from the image. In the case of the image shown in Fig. 2.15 an area of 50×50 cm^2 was selected. Two curves are obtained, one for each axis. The curve on the x-axis was obtained by summing pixel counts with a value of x constant, while the profile on the y-axis was obtained by summing counts of pixels with a value of y constant. The Full Width at Half Maximum ($FWHM$) on both axes were calculated by fitting the data to Gaussian functions. The image resolution is defined as the $FWHM$ of these curves. Image resolution depends on the reconstruction method, as well as both energy resolution and position resolution.

2.7 Design of the Compton camera with Monte Carlo simulations

A Compton camera based on scintillator bars has been designed with Monte Carlo simulations using the PENELOPE/penEasy code. The design was done with 8 scintillator bars because the digital data acquisition system available had 16 input channels (see Section 2.2). In addition, the weight of 8 detectors will be around 1.5kg, since each acquired detector has a weight of 158 g. Therefore, the total weight of this Compton camera together with the electronics might be between 2 and 3 kg. It is expected that a detection system of this weight could be mounted on a rotary wing unmanned aerial system (RWUAS). The geometry of each detector defined in the simulations is shown in Fig. 2.9 (bottom). The energy resolution, σ_E, and position resolution, σ_y, introduced in the PENELOPE/penEasy simulations are the same for the eight detectors.

The main parameters that describe the ability of a Compton camera are the angular resolution, image resolution and efficiency (see Section 2.6.2). The angular resolution depends on the uncertainties of deposited energies and position of interaction. Monte Carlo simulations are used mainly to study the geometrical contribution to the total angular resolution using CsI(Tl) scintillator bars. It is affected by both location and size of detectors. Image resolution depends on the same factors that affect angular resolution, while it also depends on the image reconstruction algorithm. The efficiency of a Compton camera is affected by the position and size of detectors.

Therefore, efficiency, angular resolution and image resolution were analysed using PENELOPE/penEasy simulations for different positions and sizes of detectors. The position of detectors and their cross-section sizes were evaluated by simulating γ-rays of 364 keV (^{131}I), 662 keV (^{137}Cs), 1173 keV (^{60}Co) and 1332 keV (^{60}Co).

2.8 Characterization of the Compton camera

Once the geometry of the Compton camera was chosen, characterization of the Compton camera was done by simulating the main energy lines emitted by ^{131}I, ^{137}Cs and ^{60}Co sources. Parameters, such as the Field of View (FOV) and the minimum number of cones needed to locate a source were estimated. The variation of efficiency with distance between the Compton camera and sources was also analysed. Furthermore, the ability to locate several point and surface sources using the back-projection method was studied.

2.9 Conclusions

Two $1.2 \times 1.2 \times 10$ cm^3 CsI(Tl) scintillator bars with two silicon photomultipliers (SiPM) each were acquired from the Scionix company. These detectors are both position and energy sensitive. They were treated superficially in order to improve the position resolution.

In order to characterise the detectors, experimental measurements with a collimated source of ^{137}Cs (662 keV) were described. The source was placed at different positions along the bar in order to obtain a relationship between the signals from both SiPMs and the source position. These measurements enabled us to determine the attenuation coefficient, as well as the position and energy resolutions. Other experimental measurements were carried out by using the two CsI(Tl) scintillator detectors. Measurements with a simple Compton camera using the two scintillator bars were carried out at the Calibration and Dosimetry Laboratory (LCD) of the Institute of Energy Technologies (INTE) of the Technical University of Catalonia (UPC). Three measurements were done with different orientations of the detectors with respect to the source. These experimental measurements were used to validate Monte Carlo simulations.

The code used in the Monte Carlo simulations is PENELOEPE/penEasy. The penEasy code has been adapted in order to provide deposited energies and position interactions in a file when the simulated gamma-rays interact in both layers. Furthermore, uncertainties in position and energy were also introduced. The geometries defined in simulations were also described.

The operation of a Compton camera has also been explained. The simple back-projection method used to calculate the images was described. It consists of the intersection of cones with the image plane, which is divided into a certain number of pixels.

Each time a conic passes over a pixel, the intensity of this pixel grows by one unit. The selection of events according to the deposited energy allow us to reduce the noise that comes from the background or an initial scattered gamma-ray. Two energy windows were defined: i) the sum of deposited energies in both layers must be inside the interval $E_\gamma \pm 3\sigma_E$ and ii) the deposited energy in the scatter layer must be $E < 125$ keV; $E < 150$ keV; $E < 170$ keV, $260 < E < 490$ keV; and $E < 170$ keV, $280 < E < 600$ keV for γ-rays of 364 keV, 662 keV, 1173 keV and 1332 keV, respectively.

The main parameters that will be used in this thesis to analyse the performance of a Compton camera were also defined. They are efficiency, angular resolution and image resolution. The design of a Compton camera based on eight CsI(Tl) scintillator bars was carried out based on the optimization of these three parameters. The design consists mainly of the determination of the position of detectors and in the size of CsI(Tl) crystals. Finally, a characterization of the Compton camera selected is briefly described. The parameters that are determined are field of View (FOV) and the minimum number of cones needed to locate a source. The dependence of efficiency on the distance between the source and the Compton camera has also been analysed for sources of ^{131}I, ^{137}Cs and ^{60}Co. In addition, the ability of the Compton camera to use the simple back-projection is also analysed by simulating simultaneously several point and surface sources.

Chapter 3

Experimental results and validation of MC simulations

In this chapter two experimental measurement campaigns in laboratory conditions were done to i) characterize the CsI(Tl) scintillator bars and ii) to validate Monte Carlo simulations. The first measurement campaign was done by irradiating the scintillator bars with a point collimated source. The second measurement campaign, a simple Compton camera made of two detectors, was irradiated at the reference irradiation facility of the UPC. The validation of PENELOPE/penEasy Monte Carlo code was carried out by comparing the experimental data with their equivalent simulated data.

3.1 Characterization of Cs(Tl) bars

In this section a characterization of the CsI(Tl) scintillator bars was done. To this end, detectors were irradiated with a collimated ^{137}Cs source with an activity of 185 kBq (19/10/2018). The point source was collimated with a lead brick with a circular opening, 3.5 mm in diameter, and a thickness of 8.4 cm. Several measurements were taken by placing the collimated source at different positions along the bar. Considering that the length of the crystals is 10 cm, eleven measurements were taken with a separation of 1 cm, as described in Section 2.4.1. The characterization of the bars consisted of determining the αL parameter, as well as the energy and position resolutions.

3.1.1 Determination of αL

Detectors 1 and 2 were irradiated with a collimated ^{137}Cs source, which was placed at different positions along the bar. Fig. 3.1 shows the ratio of both signals, S_2/S_1, for a deposited energy of 662 keV, when the source is placed at a certain position y. As was described in Section 2.3.1, the attenuation coefficient can be obtained by fitting the data to exponential functions. Data shown in Fig. 3.1 were fitted to Eq. 2.4 in order to calculate the parameter, 2α.

Fits were made when the source was placed at positions with $|y| \leq 4$, because data tends to deviate from exponential attenuation when $y \approx 5$ cm. The attenuation coefficients are equal to half of the exponential coefficients. Attenuation coefficients of 0.056 ± 0.0015 cm^{-1} and 0.091 ± 0.0011 cm^{-1} were then calculated for detectors 1 and 2, respectively. The CsI(Tl) scintillator bars have a length, L, of 10 cm, thus $\alpha L = 0.55 \pm 0.015$ and $\alpha L = 0.91 \pm 0.011$ for detectors 1 and 2, respectively. Surface treatments were similar for both crystals, but there is a significant difference between attenuation coefficients for the two bars of about 50%. For some reason, either the surface reflectivity of detector 1 ($\alpha L < 1$) might have changed or the optical transmission from the crystal to the SiPMs is not the same for both detectors (internal comment from the manufacturer of the detectors, Scionix). This result highlights the need for carrying out quality control for each detector.

3.1.2 Energy resolution

The energy deposited in the crystals was calculated by summing both signals, $S_1 + S_2$. A pulse height spectrum was acquired for each position of the collimated source. The photopeaks from each pulse height spectrum were then fitted to Gaussian functions in order to calculate their $FWHM$. Fig. 3.2 shows the energy resolution in percentage, $FWHM/E$, for both detectors. As we can see, both energy resolutions are almost constant along the bars for $|y| \leq 4$ cm. However, the energy resolution at the edges of the bars grows quickly. For example, when the source is placed at $y = 5$ cm, energy resolution values of 10% and 11% were found for detectors 1 and 2, respectively. The average values for the energy resolution are 7.6 ± 0.2% and 7.74 ± 0.10% for detectors 1 and 2, respectively. These resolution values are in agreement with the common resolution for CsI(Tl) detectors found in the literature (Gilmore, 2008).

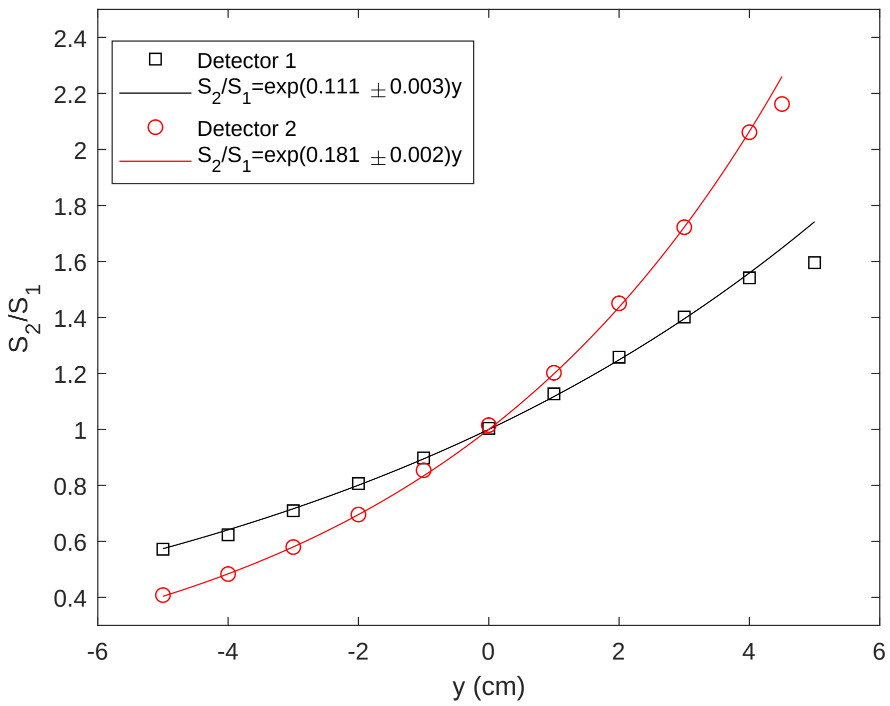

Figure 3.1: Ratio of both signals (S_2/S_1) versus the position of the source, y, when γ-rays deposit 662 keV. Results are shown for detector 1 (black squares) and detector 2 (red circles). Data with $|y| \leq 4$ were fitted to exponential functions, with an exponent of 2α.

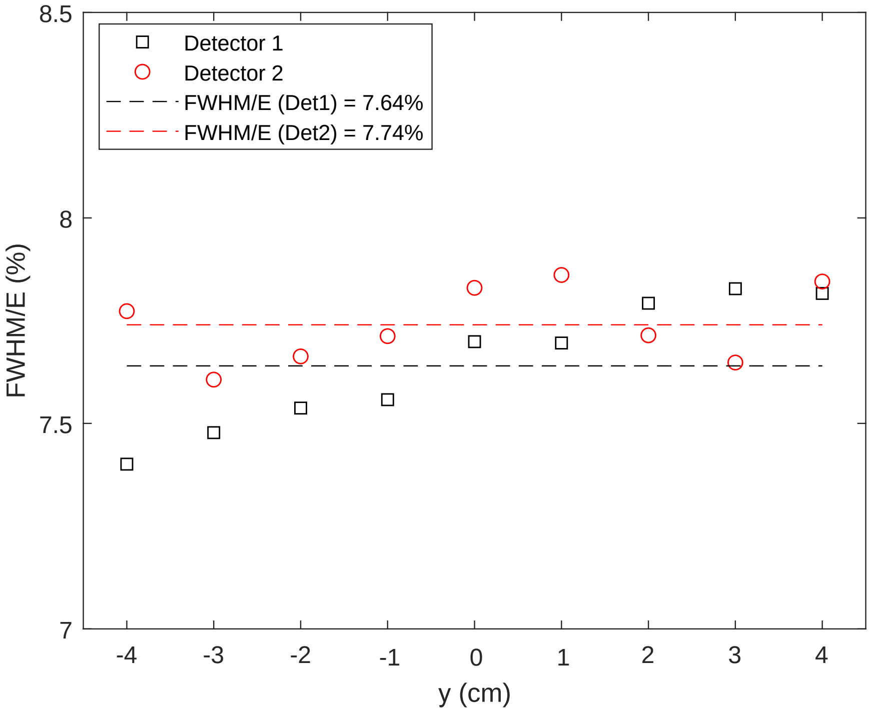

Figure 3.2: Energy resolution of detector 1 (black squares) and detector 2 (red circles). The collimated ^{137}Cs source was placed at different positions, y, along the bar. Average energy resolution values of 7.6±0.2% and 7.74±0.10% were found for detectors 1 and 2, respectively.

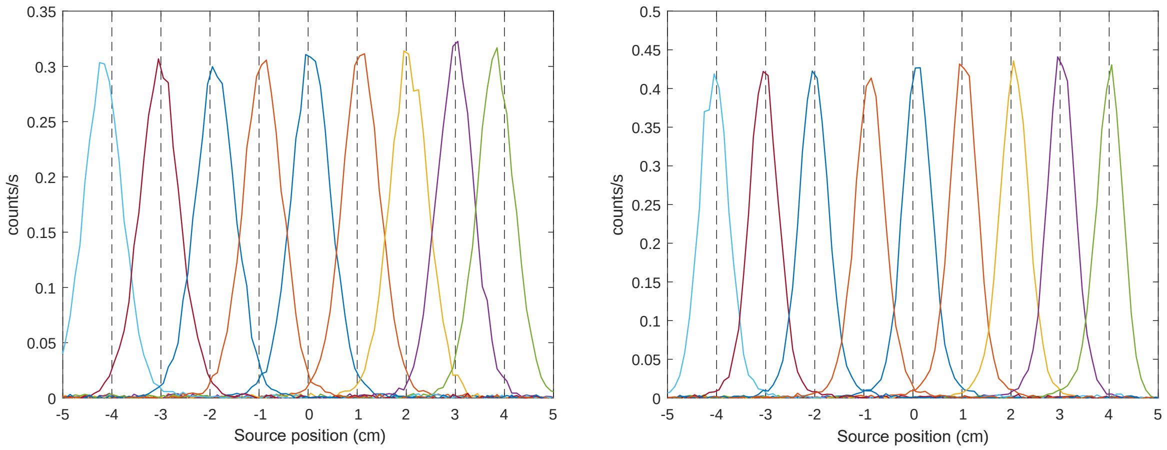

(a) Detector 1

(b) Detector 2

Figure 3.3: Histograms of the calculated position as a function of the true source position. Results are shown for (a) detector 1 and (b) detector 2. Each curve corresponds to one position of the 3.5 mm collimated ^{137}Cs source. Only events with deposited energies of $661.6 \pm 3\sigma_E$ keV were considered.

3.1.3 Position resolution

The positions of γ-ray interactions along the crystal were calculated by using Eq. 2.3. For each pair of validated signals, S_1 and S_2, the corresponding position was calculated and stored in a histogram. Fig. 3.3 shows these histograms for photopeak events ($661.6 \pm 3\sigma_E$ keV) for (a) detector 1 and (b) detector 2.

For each irradiated position shown in Fig. 3.3, data were fitted to Gaussian functions. Fig. 3.4 shows the standard deviations of the calculated Gaussian functions, σ_y, which were found to be independent of position for almost all the length of the crystal bar. The average standard deviations were 0.409 ± 0.007 cm and 0.291 ± 0.009 cm for detector 1 and detector 2, respectively. Position resolution for detector 1 is worse than for detector 2 due to the fact that the attenuation coefficient is higher for detector 2. Position resolution at the edges of the bars grows quickly. If the source is placed at $y = -5$ cm, standard deviations of 0.7 cm and 0.4 cm are found for detectors 1 and 2, respectively.

3.2 Validation of PENELOPE/penEasy simulations

This section describes the validation of PENELOPE/penEasy simulations. To this end, experimental measurements and simulated data are compared. This validation is divided into three subsections. The first and second subsections are concerned with the validation

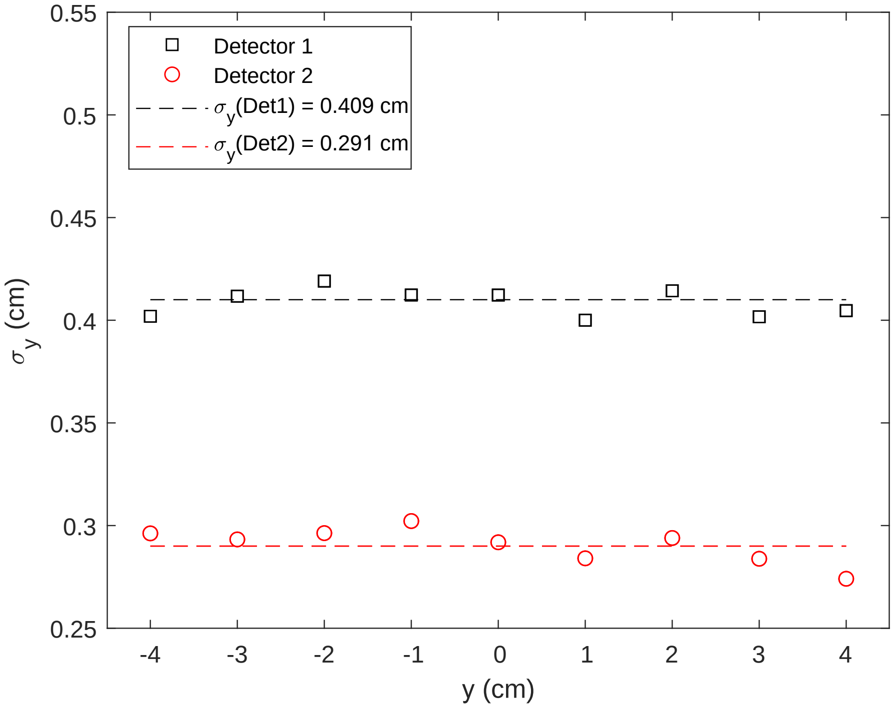

Figure 3.4: Standard deviation, σ_y, of the position calculated for detector 1 (black squares) and detector 2 (red circles) for deposited energies of $661.6 \pm 3\sigma_E$ keV. Results are shown for different positions, y, of the collimated source. Average values of position resolution of 0.409 ± 0.007 cm and 0.291 ± 0.009 cm were found for detectors 1 and 2, respectively.

of the geometry defined in the MC simulations and the position resolution calculated with Eq. 2.12, described in Section 2.3.3. Measurements carried out with the collimated ^{137}Cs source are used to perform these two validations. The third subsection consists of comparing data from experimental and simulated measurements taken with a simple Compton camera consisting of two CsI(Tl) scintillator bars. This latter comparison allowed us to validate the selection of events, angular resolution and method of reconstruction

3.2.1 Geometry validation

Experimental and simulated pulse height spectra and their photopeak count rates were compared as a means to validate the detector geometry defined in PENELOPE/penEasy simulations. Experimental irradiations consisted of irradiating the CsI(Tl) scintillator bars with a collimated ^{137}Cs source, as Section 2.4.1 describes. The geometry defined in simulations is explained in Section 2.5.2.

The experimental photopeak count rates are obtained by averaging the count rates when detectors are irradiated at positions $|y| \leq 4$. The simulated photopeak count rate is obtained

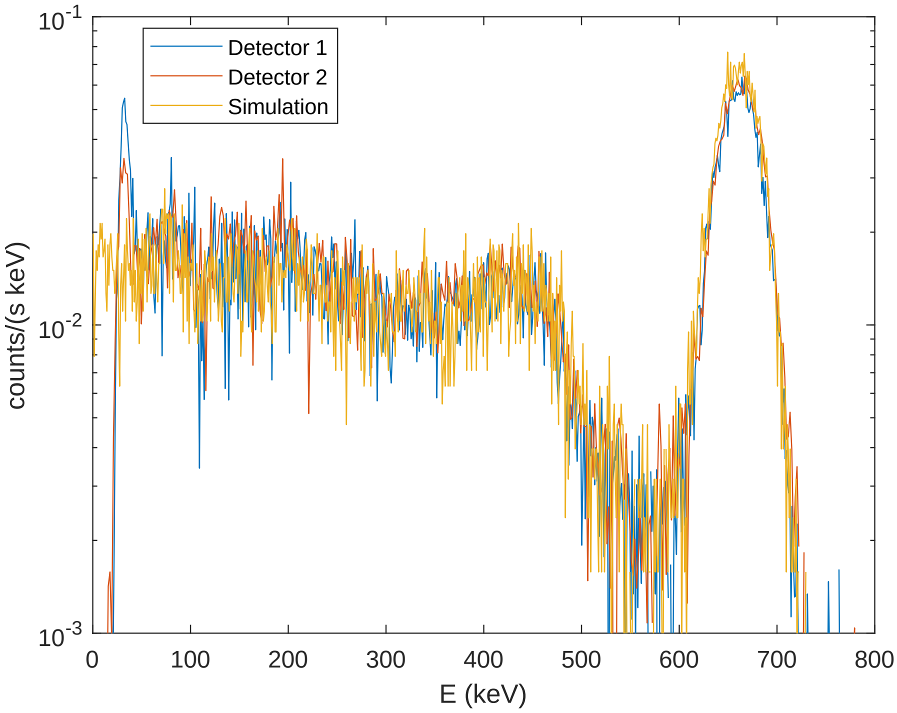

Figure 3.5: Experimental and simulated pulse height spectra when the collimated ^{137}Cs source was placed at the bar centre. The count rate is divided by the bin width.

by irradiating the detector at the bar centre. The simulated photopeak count rate is 3.4 ± 0.2 s^{-1}, while the experimental count rates were 3.1 ± 0.2 s^{-1} and 3.3 ± 0.2 s^{-1} for detectors 1 and 2, respectively. Uncertainties are expressed with a coverage factor of $k = 2$. The experimental and simulated count rates are in good agreement.

In Fig. 3.5 both the experimental and simulated pulse height spectra obtained when irradiations take place at the bar centre are compared. Energy resolutions were obtained for a deposited energy of 662 keV in Section 3.1.2. Energy resolutions for energies different to 662 keV are calculated by assuming that $\sigma_E = w/\sqrt{E}$, where w is a constant equal to 0.83 ± 0.02 keV$^{3/2}$ and 0.847 ± 0.011 keV$^{3/2}$ for detector 1 and 2, respectively. These values of w are calculated with the experimental results provided in Section 3.1.2. Energy resolution is then introduced in simulations using Eqs. 3.1 and 3.2 for detectors 1 and 2, respectively.

$$\sigma_E = \frac{0.83}{\sqrt{E}} \tag{3.1}$$

$$\sigma_E = \frac{0.847}{\sqrt{E}} \tag{3.2}$$

As we can see in Fig. 3.5, agreement over all the energy range of the spectrum is good considering that X-rays emitted by the ^{137}Cs source were not simulated.

3.2.2 Position resolution

The standard deviation, σ_y, is introduced in simulations with Eq. 2.12, which depends on the attenuation coefficient, energy resolution and intrinsic energy resolution (see Section 2.3.3). The attenuation coefficient and energy resolution were calculated experimentally for both detectors in Sections 3.1.1 and 3.1.2. Energy resolutions for deposited energies different to 662 keV were calculated with Eqs. 3.1 and 3.2. As was described in Section 2.3.2 the intrinsic energy resolution is calculated for different energy ranges: 20keV$\leq E_{dep} < 30$ keV, 30 keV $\leqslant E_{dep} < 510$ keV and $E_{dep} \geq 510$ keV. Each section was fitted to a function $\left(\frac{FWHM}{E}\right)^2_{int} = a + \frac{b}{\sqrt{E}}$, and parameters are shown in Eqs. 2.7, 2.8 and 2.9.

The position resolution calculated with simulations, i.e. using Eq. 2.12, is determined for a 3.5-mm collimated ^{137}Cs source in order to compare it with experimental results. The geometry defined in simulations was described in Section 2.5.2 and validated in Section 3.2.1. Standard deviation, σ_y, was introduced in MC simulations using Eqs. 2.12, 3.1, 3.2, 2.7, 2.8 and 2.9. Standard deviations of 0.42 ± 0.03 cm and 0.28 ± 0.02 cm were found for detectors 1 and 2, respectively.

The experimental position resolutions for the same geometry as those used in simulations were 0.409 ± 0.007 cm and 0.291 ± 0.009 cm for detector 1 and detector 2, respectively, as was described in Section 3.1.3. Experimental and simulated results are in clear agreement.

3.2.3 Compton camera consisting of two scintillator bars

As described in Section 2.4.2, a simple Compton camera (sCC) made of two CsI(Tl) scintillator bars was exposed at the irradiation facility of the UPC (LCD). It was also explained in Section 2.6.1 that the interaction in the scatter and absorber detectors should be in a specific range of energies in order to choose the events that are used to calculate the image. Two energy windows were used, which consisted of i) the sum of deposited energies in both detectors had to be within $662 \pm 3\sigma_E$, and ii) deposited energies in the scatter detector had to be lower than or equal to 150 keV for an incoming γ-ray of 662 keV in order to build the Compton cones. Section 3.3 will show that position resolution is poorer for low deposited energies (see Fig. 3.9). Selecting events should mean that energies deposited in the scatter layer will be lower than 150 keV and therefore deposited energies in the absorber detector should be higher than 512 keV. Position and energy resolutions of scatter detectors have a greater influence than energy and position resolutions of absorber detectors. As Section 3.1.3 shows, detector 2 has a better position resolution than detector 1. Therefore, detector 2 was used as the scatter detector and detector 1 as the absorber.

In the LCD, the sCC was placed on a rotary methacrylate plate 5 metres away from the source. Three irradiations were carried out for a duration of 20 min. As described in detail in Section 2.4.2, the sCC was placed at 0°, 20° and $-20°$ from the source point view. The source used was a ^{137}Cs source with an activity of 299 MBq on 03/03/2020, and the dose rate was $1.16 \cdot 10^{-3}$ mSv/h. Pile-up was observed when the dose rate was $8.05 \cdot 10^{-2}$ mSv/h, while if dose rate was lowered to $7.32 \cdot 10^{-3}$ mSv/h, there was no pile-up.

These experimental measurements were compared to their corresponding simulated calculations in order to validate the MC code and the codes used to calculate the image for a Compton camera based on CsI(Tl) scintillator bars. The number of histories emitted by the source in the simulations was equivalent to the number of γ-rays emitted by a source of 299 MBq for 20 min. The comparison between the experimental and simulated results can be separated into three sections: choice of events, angular resolution and reconstruction of images.

Choice of events

In this section, results from the selection of those γ-rays that interact in both detectors in experimental and simulated measurements are compared. For the experimental measurements, the choice of events that interact in both detectors are determined by using the coincidence windows described in Sections 2.4.1 and 2.4.2. Furthermore, the energy windows, described in Section 2.6.1, are applied in order to select the events that are used to build the Compton cones and, in consequence, to create the image. Validation of the MC simulations and the developed codes was done by comparing experimental and simulated pulse height spectra and the number of cones per second calculated.

First, the response of each individual detector is compared with the response calculated with the simulation. Table 3.1 shows that the experimental and simulated photopeak count rates of the scatter and the absorber detectors are in good agreement.

Experimental and simulated pulse height spectra calculated by summing up the

Table 3.1: Experimental and simulated photopeak count rates detected by the scatter and absorber detectors. The uncertainties are presented with a 95% confidence interval ($k = 2$).

	Count rate (s^{-1})			
Rotation	Scatter Experimental	Absorber Experimental	Scatter Simulation	Absorber Simulation
0°	86.6 ± 0.5	54.6 ± 0.4	86.7 ± 0.5	53.8 ± 0.4
20°	85.6 ± 0.5	54.6 ± 0.4	84.8 ± 0.5	53.4 ± 0.4
−20°	85.7 ± 0.5	54.6 ± 0.4	84.8 ± 0.5	53.4 ± 0.4

Table 3.2: Photopeak count rates from the pulse height spectra obtained by summing deposited energies from events that occur in coincidence in both detectors. Experimental and simulated results are shown. The uncertainties are presented with a 95% confidence interval ($k = 2$).

	Count rate (s^{-1})	
Rotation	Experimental	Simulation
0°	4.18 ± 0.12	3.98 ± 0.12
20°	3.91 ± 0.11	3.76 ± 0.11
−20°	4.01 ± 0.11	3.76 ± 0.11

deposited energies from events that occur in coincidence in both detectors are then compared, as shown in Fig. 3.6. This figure shows that the simulated spectrum is able to properly reproduce the photopeak. However, a difference in the scattering energy region is observed. The reason for this difference can be explained due to the geometry of the photonic irradiator that consists of a roulette of sources. Therefore, it is not possible to avoid gamma scattering as a consequence of neighbouring sources. Fig. 3.6 shows the results when the sCC was irradiated at 0°. Comparisons for the other angles are not shown, but results are similar. The experimental and simulated photopeak count rates are in reasonable agreement as shown in Table 3.2.

Another comparison for validating the MC and developed codes are the spectra of the scatter and the absorber detectors when the emitted γ-rays interact in both detectors in coincidence and their deposited energies sum $662 \pm \sigma_E$. Fig. 3.7 shows the results obtained with the scatter detector (left column) and absorber detector (right column), and for different angles of incidence, 0° (top), 20° (middle) and −20° (bottom). Good agreement between measurements and simulations for both detectors is shown.

The number of Compton cones per second are calculated from those γ-rays that interact in both detectors in coincidence and it is verified that i) their deposited energies sum

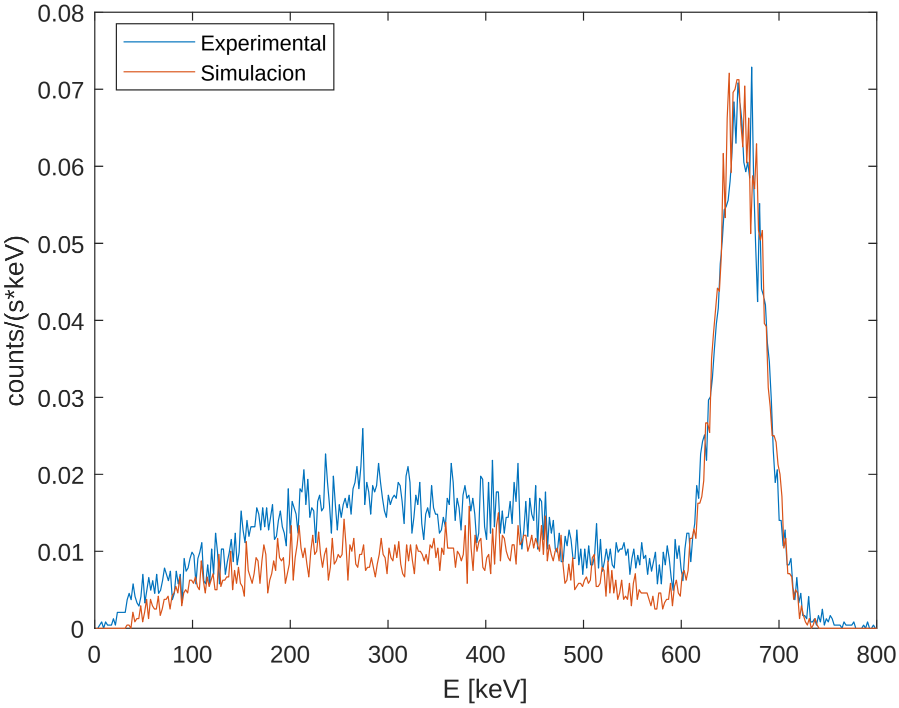

Figure 3.6: Experimental and simulated pulse height spectra obtained by summing deposited energies from events that occur in coincidence in both detectors. Measurements were obtained by placing the detectors at 0° from the point of view of the source. The count rate is divided by the bin width.

$661.6 \pm 3\sigma_E$ keV, and ii) the deposited energy in the scatter detector is less than 150 keV. The good agreement between experimental and simulated results is compared in Table 3.3. It is important to note that after selecting data using the coincidence windows and the energy windows, there is no significant influence of the natural background and of the gamma scatterings from neighbouring sources on the experimental results.

Table 3.3: Number of cones per second accepted in the experimental and simulated measurements. The uncertainties are presented with a 95% confidence interval ($k = 2$).

	Count rate (s^{-1})	
Rotation	Experimental	Simulation
0°	1.57 ± 0.07	1.64 ± 0.07
20°	1.36 ± 0.07	1.40 ± 0.07
−20°	1.42 ± 0.07	1.40 ± 0.07

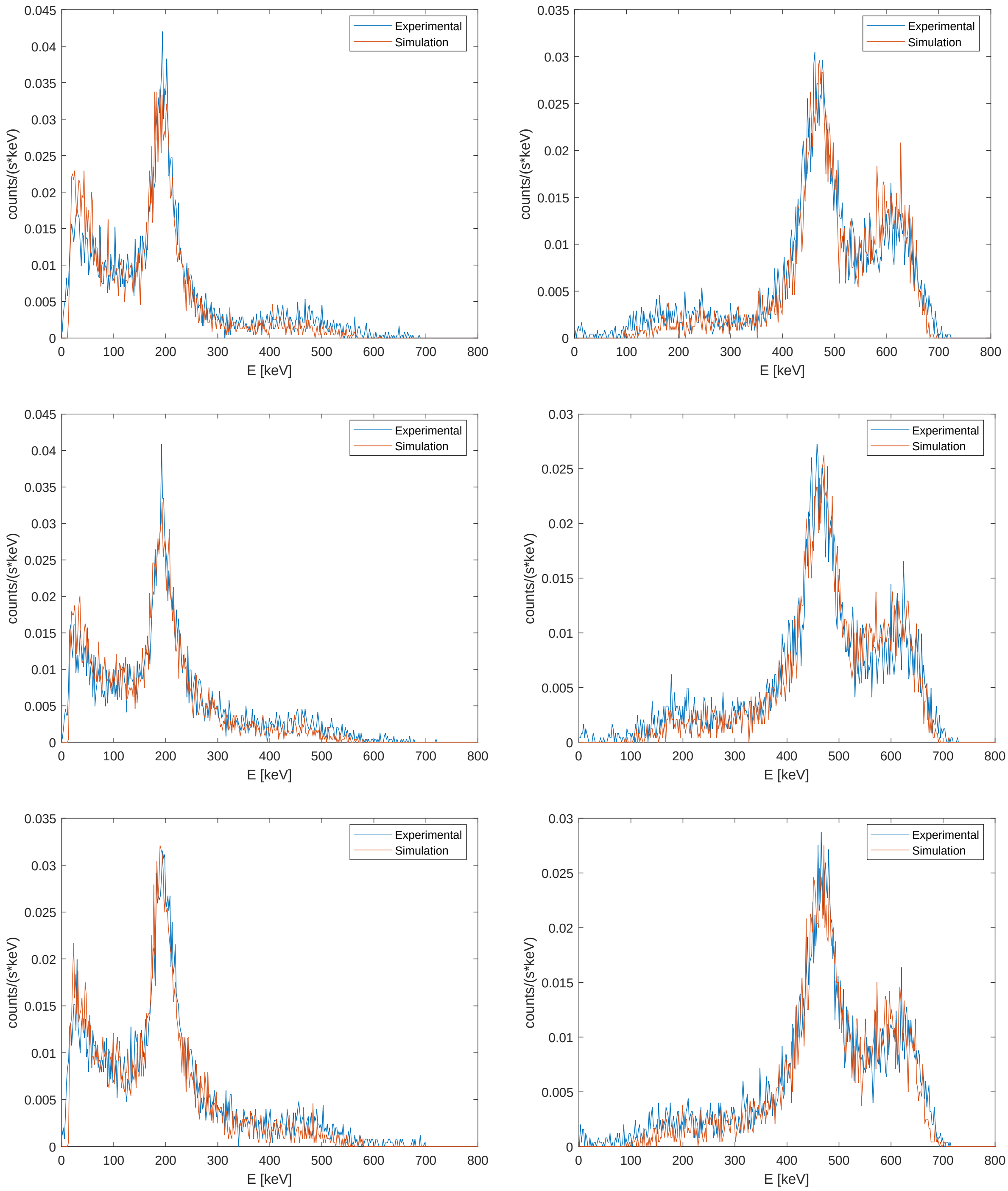

Figure 3.7: Pulse height spectra of those gamma-rays that interact in both detectors in coincidence and their deposited energies sum $661.6 \pm 3\sigma_E$ keV. Results from the scatter detector are plotted in the first column, while results from the absorber detector are plotted in the second. Simulated and experimental results are shown for the three irradiations: 0° (top), 20° (middle) and −20° (bottom). The count rate is divided by the bin width.

Table 3.4: Experimental and simulated standard deviation of ARM. The uncertainties are presented with a 95% confidence interval ($k = 2$).

	$FWHM_{ARM}$ (degrees)	
Rotation	Experimental	Simulation
0°	28 ± 2	33 ± 3
20°	27 ± 2	29 ± 2
−20°	29 ± 3	29 ± 2

Angular resolution

The angular resolution ($ARM = \theta_c - \theta_{geo}$) has been calculated for experimental and simulated results. Once events have been selected to generate the Compton cones, the experimental position of interaction on the y-axis (along the bar), in both crystals is calculated using Eq. 2.3. The scattering angle was calculated with the deposited energies using the Compton equation. The geometric angle was calculated with the position of the γ-ray interactions and the source position. In the MC simulations, the deposited energies and position of interaction, y, are values that do not include uncertainties. In order to compare them with experimental results, they should be recalculated before calculating the Compton scattering angle together with the geometric angle to evaluate the corresponding uncertainties. Therefore, before calculating these angles, the energy and the position calculated by simulations were spread out by assuming that their resolutions follow a Gaussian distribution with standard deviations of σ_E and σ_y, respectively (see Section 2.5.1). In order to simulate the position of interaction in the crystal cross-section, random numbers generated by a uniform distribution were used in both the cases of experimental and simulated calculations.

Angular resolution was then calculated for the experimental and the simulated measurements and are then compared in order to validate the values of the resolutions σ_E and σ_y, used in the simulations. The experimental and simulated standard deviations of ARM are in good agreement, as shown in Table 3.4.

As was explained in Section 2.6.2, ARM is affected mainly by energy resolution, position resolution and Doppler broadening. Their contributions to ARM can be analysed by doing PENELOPE/penEasy simulations. PENELOPE considers Doppler broadening and binding effects in order to simulate Compton scattering (Salvat, 2015). Thus, the error introduced when the Compton equation is used can be evaluated with PENELOPE/penEasy. The

Table 3.5: Standard deviation of ARM when Doppler broadening, energy resolution (σ_E), uncertainties in the position of the crystal cross-section (u_{xz}) and position resolution along the bar (σ_y) are considered separately. The proportion of each contribution to the total angular resolution is shown in parenthesis.

	$FWHM_{ARM}$ (degrees)			
Rotation	Doppler	Doppler $+\sigma_E$	Doppler $+u_{xz}$	Doppler $+\sigma_y$
0°	3.2 ± 0.3 $(0.93 \pm 0.17\%)$	5.9 ± 0.2 $(3.2 \pm 0.3\%)$	13.3 ± 0.2 $(16.0 \pm 1.2\%)$	29.7 ± 1.2 $(79.9 \pm 1.4\%)$

effect of Doppler broadening on the angular resolution is examined by comparing the true scattering angle, which is determined with the real position interactions and the position of the source, with the scattering angle calculated by the Compton equation. The effect of position resolution and energy resolution on the angular resolution is evaluated by considering such resolutions separately. Due to the fact that Doppler broadening is included in the PENELOPE code, its contribution to the angular resolution will be considered when the contributions of energy and positions resolutions have been evaluated.

A long simulation was carried out with detectors placed at 0° from the source point of view in order to have good statistics. Table 3.5 shows the results. Doppler broadening and energy resolution, σ_E, are the components that contribute the least to ARM. If both contributions are considered together, they represent 3.2% of the angular resolution. On the other hand, the position resolution introduces important uncertainties to the angular resolution. The position resolution is divided into two components: uncertainties in the crystal cross-section (u_{xz}) and position resolution along the bar (σ_y). The contribution of Doppler broadening together with u_{xz} is 16%, while the contribution of Doppler broadening with σ_y is 79.9%. Therefore, position resolution along the bar introduces the greatest uncertainty to ARM for a Compton camera consisting of two CsI(Tl) scintillator bars of $1.2 \times 1.2 \times 10$ cm^3. Doppler broadening of the scattering angle can be considered negligible compared with the effect of position resolutions, since Doppler broadening only contributes 0.93% to the angular resolution.

Image reconstruction

In order to reconstruct and compare images for both experimental and simulated measurements, the list mode Simple Back-Projection method described in Section 2.6 was used. Experimental and simulated images are shown in Fig. 3.8. The left column

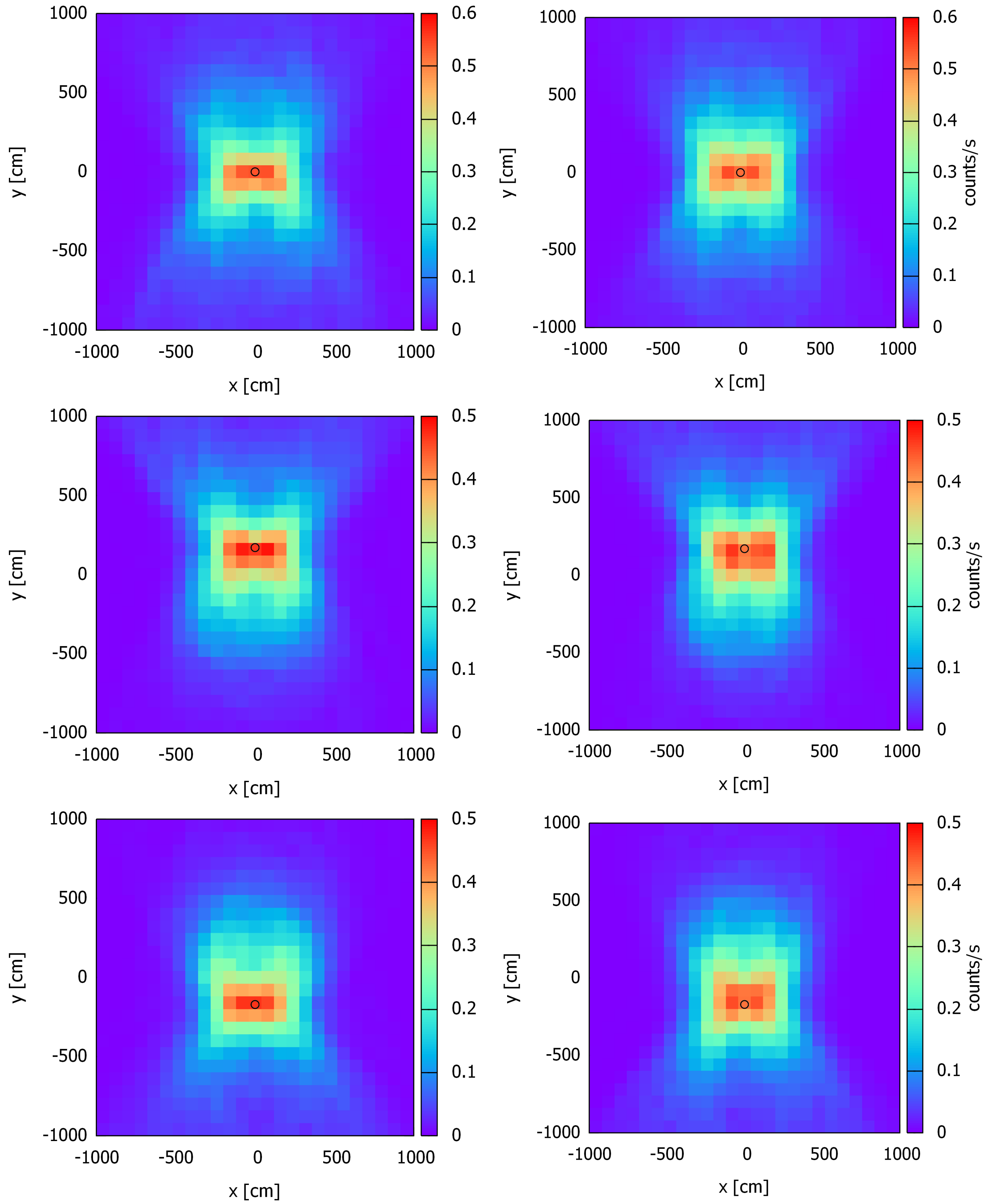

Figure 3.8: Images obtained with the Simple Back projection method. Experimental images are shown in the left column, while simulated images are shown in the right column. Results are shown for the three irradiations: 0° (top), 20° (middle) and −20° (bottom). The position of the source is indicated with circles. The bar colour indicates the number of cones per second that pass over a given pixel.

Table 3.6: Image resolution on both axes, x and y, for a Compton camera consisting of two CsI(Tl) scintillator bars. Experimental and simulated results are shown with a 95% confidence interval ($k = 2$).

	Experimental		Simulation	
Rotation	$FWHM_x$ (cm)	$FWHM_y$ (cm)	$FWHM_x$ (cm)	$FWHM_y$ (cm)
0°	784 ± 62	423 ± 54	715 ± 53	471 ± 32
20°	732 ± 56	541 ± 83	679 ± 56	557 ± 69
−20°	719 ± 52	594 ± 61	685 ± 51	637 ± 67

corresponds to the experimental images, while the right column corresponds to the simulated images. Results for different angles of incidence, 0° (top), 20° (middle) and −20° (bottom), are shown. The position of the source is indicated with circles. The bar colour indicates the number of cones per second that pass over a given pixel. As we can see, experimental and simulated images are in good agreement.

As was described in Section 2.6.2, the image resolution is estimated from images. A ROI was selected in order to obtained two curves from the images, one for each axis. The widths of these two curves are calculated by fitting data to Gaussian functions. Table 3.6 shows the $FWHM$ of these curves for experimental and simulated results. This $FWHM$ is a measure of the image resolution of a Compton camera based on two CsI(Tl) scintillator bars when images are obtained by applying the simple back projection method. Results show good agreement between experimental and simulated results.

3.3 Dependence of position resolution with deposited energy

In order to find out the dependence of standard deviation, σ_y, on deposited energy, simulations of collimated γ-ray beams with energies of 59.54 keV, 122 keV, 364.5 keV, 661.6 keV, 1173.2 keV and 1332.5 were done. Energy resolution for energies different to 661.6 keV was calculated using Eqs. 3.1 and 3.2. The standard deviation, σ_y, was introduced in simulations with Eq. 2.12. The standard deviation, σ_y, was plotted in Fig. 3.9 as a function of deposited energy. Data were fitted to the function $\sigma_y = q + r/\sqrt{E}$, where q and r are constants. Values of -0.16 ± 0.05 and 15.4 ± 0.7 were found for detector 1, while values of -0.08 ± 0.03 and 9.5 ± 0.4 were found for detector 2, as Eqs. 3.3 and 3.4 show.

$$\sigma_y = -0.16 \pm 0.05 + \frac{15.4 \pm 0.7}{\sqrt{E}} \tag{3.3}$$

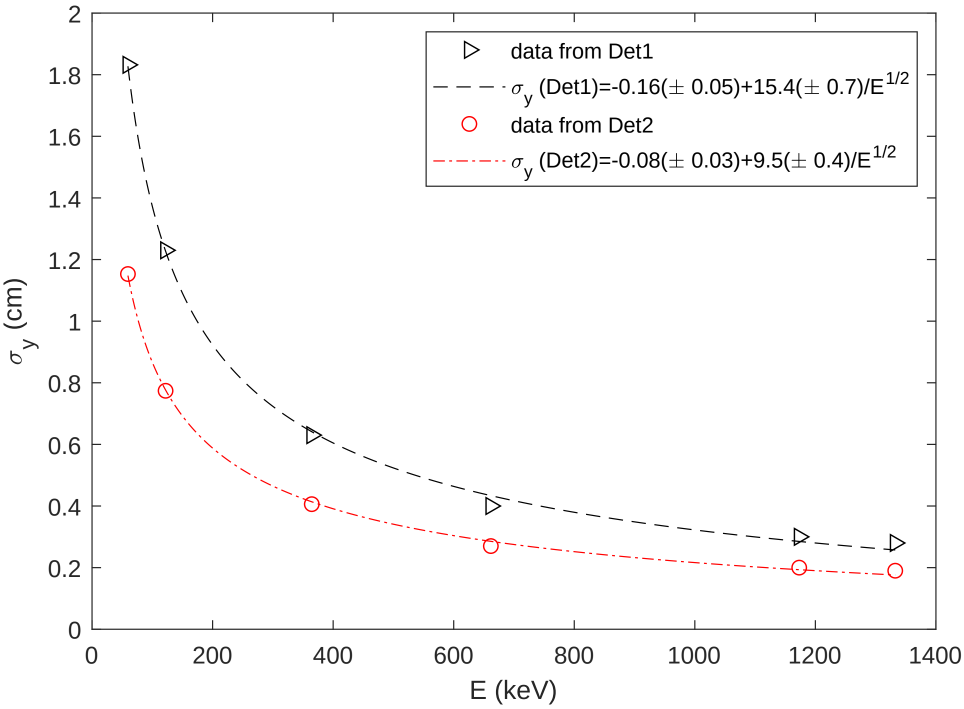

Figure 3.9: Position resolution, σ_y, versus the energy deposited for both detectors. Data were fitted to the function $\sigma_y = q + r/\sqrt{E}$. Data were obtained by simulated collimated γ-ray beams with energies of 59.54 keV, 122 keV, 364.5 keV, 661.6 keV, 1173.2 keV and 1332.5 keV.

$$\sigma_y = -0.08 \pm 0.03 + \frac{9.5 \pm 0.4}{\sqrt{E}} \tag{3.4}$$

As was expected, simulations provide a better resolution for detector 2. Thus, detector 2 would be preferable over detector 1. As we can see in Fig. 3.9, position resolution worsens for low deposited energies. The standard deviation, σ_y, is assumed constant for a given deposited energy and independent of the position of interaction.

3.4 Conclusions

Characterization of the CsI(Tl) scintillator bars with SiPMs and the validation of Monte Carlo simulations have been done in this chapter. The characterization of detectors was carried out by irradiating the CsI(Tl) scintillator bars with a 3.5-mm collimated ^{137}Cs point source. Several measurements were taken by placing the collimated source at different positions along the bar. The characterization of the bars consisted of determining the attenuation coefficient, together with the energy and position resolutions. Attenuation coefficients of

0.056 ± 0.0015 cm^{-1} and 0.091 ± 0.0011 cm^{-1} were found for detectors 1 and 2, respectively. There is a difference between them of about 50%. This might indicate that one of the detectors suffered a change of the surface reflectivity or the optical transmission from the crystal to the SiPMs is not the same for both detectors. Energy resolution and position resolution were found to be almost independent of the position of γ-ray interactions. The energy resolutions found was $7.6 \pm 0.2\%$ $(FWHM)$ and $7.74 \pm 0.10\%$ $(FWHM)$ for detectors 1 and 2, respectively. The position resolutions along the bar were 0.409 ± 0.007 cm (σ_y) and 0.291 ± 0.009 cm (σ_y) for the same detectors. The position resolution for detector 1 is not as good as for detector 2, which is consistent with the fact that the attenuation coefficient is higher for detector 2.

The validation of PENELOPE/penEasy Monte Carlo code was done by comparing experimental data with their equivalent simulated data. First, the validation of the geometry defined in MC simulations was carried out by comparing experimental and simulated pulse height spectra when the collimated source of ^{137}Cs was placed at the bar centre. Simulations were able to reproduce experimental results.

The standard deviation σ_y was calculated in MC simulations using Eq. 2.12, which depends on the attenuation coefficient α, the standard deviation of energy σ_E and the intrinsic standard deviation of energy σ_E^{int}. The attenuation coefficient was calculated experimentally for both detectors in Section 3.1.1. The standard deviation of energy was calculated using Eqs. 3.1 and 3.2. The intrinsic energy resolution was obtained from the literature, as was shown in Section 2.3.2. The simulated and experimental position resolutions were compared when detectors were irradiated at the bar centre with a collimated ^{137}Cs source. Simulations are able to reproduce experimental results

Finally, validation of the MC code and the codes used to calculate the image for a Compton camera consisting of CsI(Tl) scintillator bars was done. To this end, a simple Compton camera made of two CsI(Tl) scintillator bars was irradiated at the reference irradiation facility of the UPC. Equivalent MC simulations were done in order to compare the main results. The validation was carried out in three steps. The first step consisted of comparing the response of each individual detector with the response calculated with the simulation and comparing the experimental and simulated number of Compton cones. Results show good agreement between experimental and simulated data.

In the second step the standard deviations of the ARM distribution were compared.

ARM is mainly affected by energy resolution, position resolution and Doppler broadening. The position of interaction and deposited energy calculated with MC simulations were spread out assuming that their resolutions follow a Gaussian distribution with standard deviations of σ_y (Eq. 2.12) and σ_E (Eqs. 3.1 and 3.2), respectively. Doppler broadening was also considered in the PENELOPE/penEasy simulations. The recalculation of position and deposited energy was validated by comparing the experimental and simulated standard deviations of ARM, which were in good agreement. MC simulations allow us to determine the contribution of Doppler broadening, position resolution and energy resolution to ARM. Doppler broadening together with u_{xz} is 16.1%, while the contribution of Doppler broadening with σ_y is 79.7%. The position resolution along the bar is the main contribution to the angular resolution of a Compton camera consisting of two CsI(Tl) scintillator bars of 1.2 × 1.2 × 10 cm^3. Doppler broadening can be considered negligible compared with the effect of position resolutions, since Doppler broadening contributes 0.95% to the angular resolution.

The last step focuses on validating the codes used to calculate the images, which was done with the simple back-projection method. Experimental and simulated images are in good agreement. It is important to note that there is no significant influence of the background on experimental results after selecting data using the coincidence and energy windows. Experimental and simulated image resolutions, which were estimated from images, were also compared.

In addition, a relationship of position resolution with energy deposited was calculated in order to simplify the introduction of the position resolution into Monte Carlo simulations. Collimated γ-ray beams with energies of 59.54 keV, 122 keV, 364.5 keV, 661.6 keV, 1173.2 keV and 1332.5 keV were used in order to obtained the dependence of standard deviation, σ_y, on deposited energy. As expected, detector 2 has a better position resolution than detector 1. The standard deviation, σ_y, is assumed constant for a given deposited energy and independent of the position of interaction.

Chapter 4

Design of a Compton camera

The design of a Compton camera consisting of two layers of CsI(Tl) detectors, called the scatter and absorber layers, was done by Monte Carlo simulations. The Compton camera efficiency, the angular resolution and the image resolution were descreibed in Section 2.6.2. They were analysed for different configurations of Compton cameras to choose the optimum one. Efficiency is the ratio of the selected events used to calculate the image and the gamma-rays emitted by the source. Angular resolution of a Compton camera is defined as the Full Width at Half Maximum (FWHM) of the ARM distribution. Image resolution is defined from the calculated images. It is defined as the FWHM of the two curves obtained by integrating counts along both axes in the image.

The Compton camera design was done in three stages. First, the optimum geometric arrangement of the scintillator detectors was analysed. The optimum sizes of the scatter and absorber detectors were then studied. Finally, the best distance between the scatter and absorber layers was analysed. The optimum geometric arrangement was found by simulating gamma-rays of 662 keV (^{137}Cs), while optimization of the size of detectors and the distance between layers was done over a wide energy range by simulating γ-rays of 364 keV (^{131}I), 662 keV (^{137}Cs), 1173 keV (^{60}Co) and 1332 keV (^{60}Co).

4.1 Geometric arrangement

As was explained in Section 2.6.2, the Compton camera efficiency improves when the surfaces of the scatter and absorber layers are maximized. This is achieved by siting the maximum number of detectors in both layers. As the number of independent available

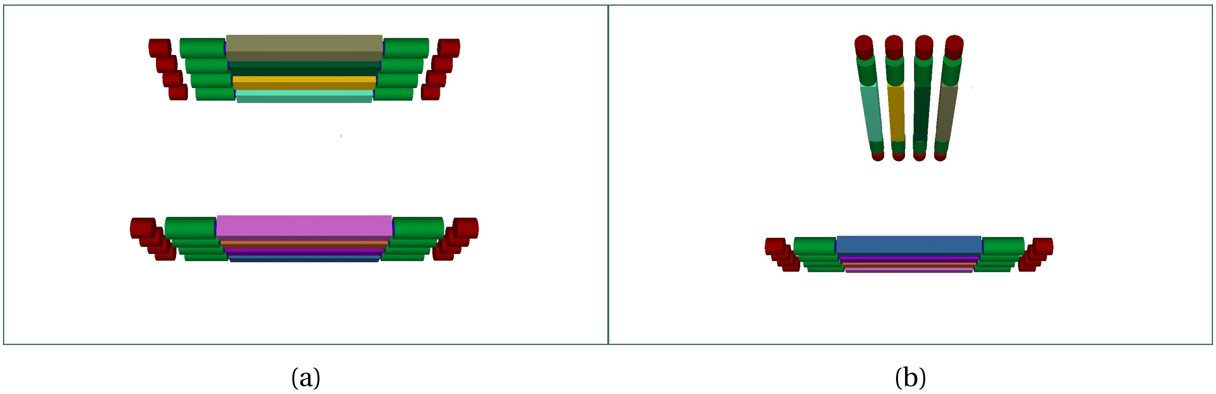

(a) (b)

Figure 4.1: Geometry of two Compton cameras consisting of (a) two parallel layers and (b) two perpendicular layers. Each layer has 4 scintillator bars. The detailed geometry of each detector can be seen in Fig. 2.9 (bottom) from Section 2.5.2. The aluminium detector housings are not shown for illustration purposes.

signal channel inputs of the digitizer was 16, the total number of detectors in the Compton camera was eight (see Section 2.2). Therefore, both layers have four scintillator bars each. The two layers can be arranged in parallel, in a perpendicular configuration or in an intermediate geometric arrangement. In order to evaluate these geometric configurations, extreme geometries were analysed. Fig. 4.1a and Fig. 4.1b show Compton cameras consisting of two parallel layers and two perpendicular layers, respectively. The aluminium detector housings are not shown in Fig. 4.1 in order to distinguish the individual detectors. The geometry of each detector is shown in Fig. 2.9 (bottom) in Section 2.5.2 with crystal dimensions of $1.2 \times 1.2 \times 10$ cm^3.

The cartesian coordinate system was chosen in such a way that the xy plane is centred in the scatter layer, $z = 0$ at the centre of scatter detectors. The z axis is oriented towards the absorber plane, i.e. the absorber layer is placed in the half space with $z > 0$. An isotropic point source of 662 keV was simulated using both geometries of Fig. 4.1 for comparison purposes. The point source was placed at the centre ($x = y = 0$) and 100 cm away from the surface of the scatter crystals ($z = -100.6$ cm). Simulations were done for different distances between the scatter and absorber layers in order to see how efficiency, ARM and image resolution change using either geometry.

In Fig. 4.2, efficiencies of the parallel and perpendicular configurations are shown for different distances between the scatter and absorber layers. It is clearly seen that there is not a significant difference between both configurations.

As regards the angular resolution, $FWHM_{ARM}$, the perpendicular Compton camera

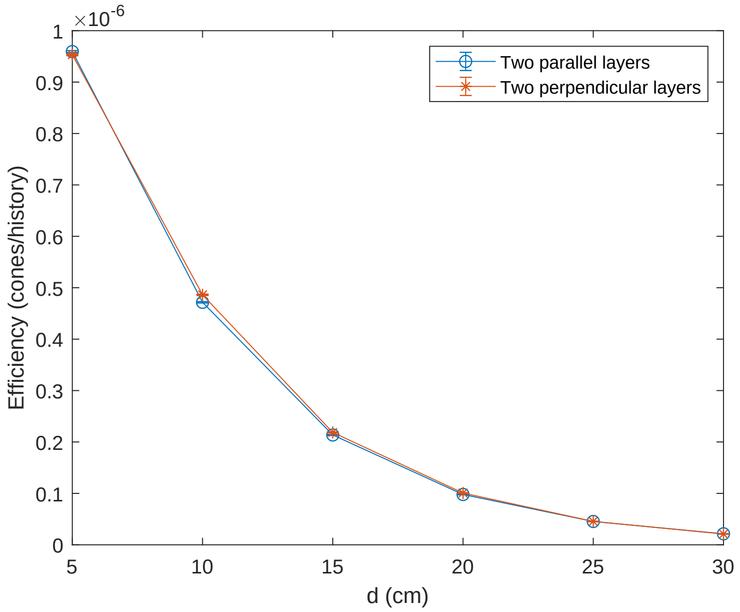

Figure 4.2: Efficiencies calculated from simulations carried out with the geometries consisting of two parallel layers (Fig. 4.1a) and two perpendicular layers (Fig. 4.1b). Simulations were done for different distances, d, between layers (from surface to surface). The source was an isotropic source of 662 keV located at 1 m from the scatter layer. The number of γ-rays emitted by the source is denoted by the term histories.

configuration is slightly better than the parallel one, as Fig. 4.3a shows. However, the image resolution on the y-axis (Fig. 4.3b), $FWHM_y$, is not as good for the perpendicular configuration as for the parallel configurations. Furthermore, Fig. 4.3b shows that for the parallel configuration the image resolution along both axes is more similar than for the perpendicular array, which led to better image symmetry.

An example of the reconstructed images is shown in Fig. 4.4 for a distance between layers of 15 cm. Fig. 4.4a is the image obtained by the Compton camera consisting of two parallel layers, while Fig. 4.4b is the image for the Compton camera consisting of two perpendicular layers. As we can see in Fig. 4.4, the asymmetry of images is more important for the perpendicular configuration than the parallel array. Image resolution was 21.6 ± 1.1 cm ($FWHM_x$) and 27.4 ± 0.5 cm ($FWHM_y$) for the parallel configuration, while image resolution found for the perpendicular configuration was 21.2 ± 0.9 cm ($FWHM_x$) and 29.5 ± 0.8 cm ($FWHM_y$).

There is no clear advantage between either geometric arrangement. From a mechanical point of view, the parallel configuration means it could be easier to mount on a drone than a perpendicular configuration. Therefore, in order to continue with the study, the parallel geometry arrangement was chosen.

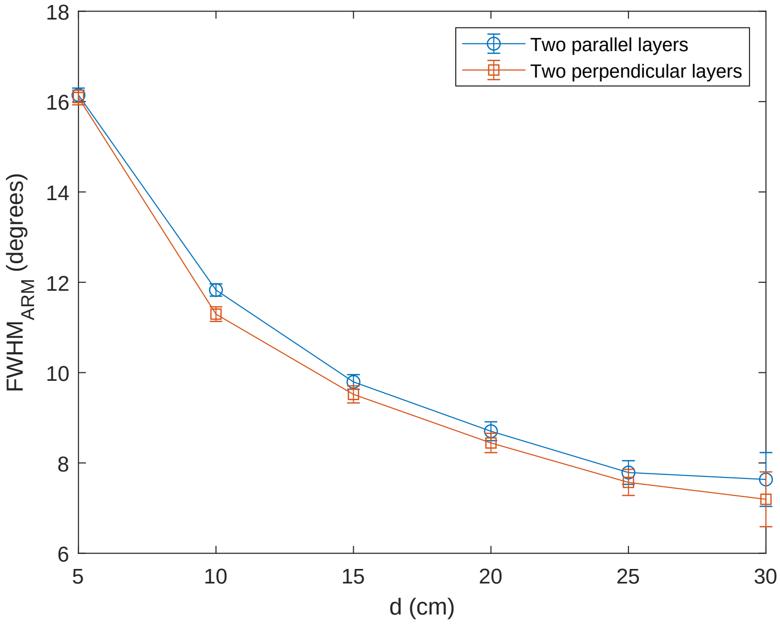

(a) Angular resolution

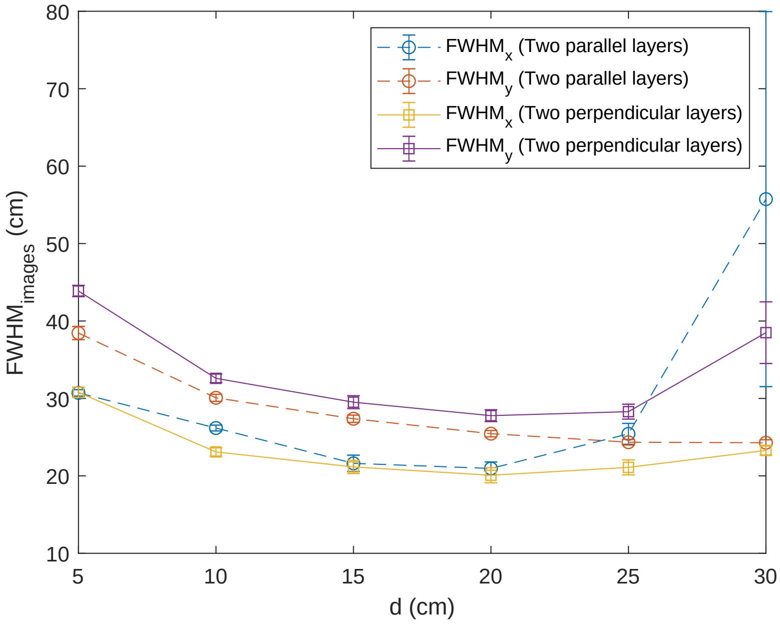

(b) Image resolution

Figure 4.3: Angular resolution and image resolution obtained with PENELOPE/penEasy simulations. Two geometries were used: two parallel layers (Fig. 4.1a) and two perpendicular layers (Fig. 4.1b). Simulations were done for different distances, d, between layers (from surface to surface). The source was an isotropic source of 662 keV located at 1 m from the scatter layer. The number of γ-rays emitted by the source is called histories.

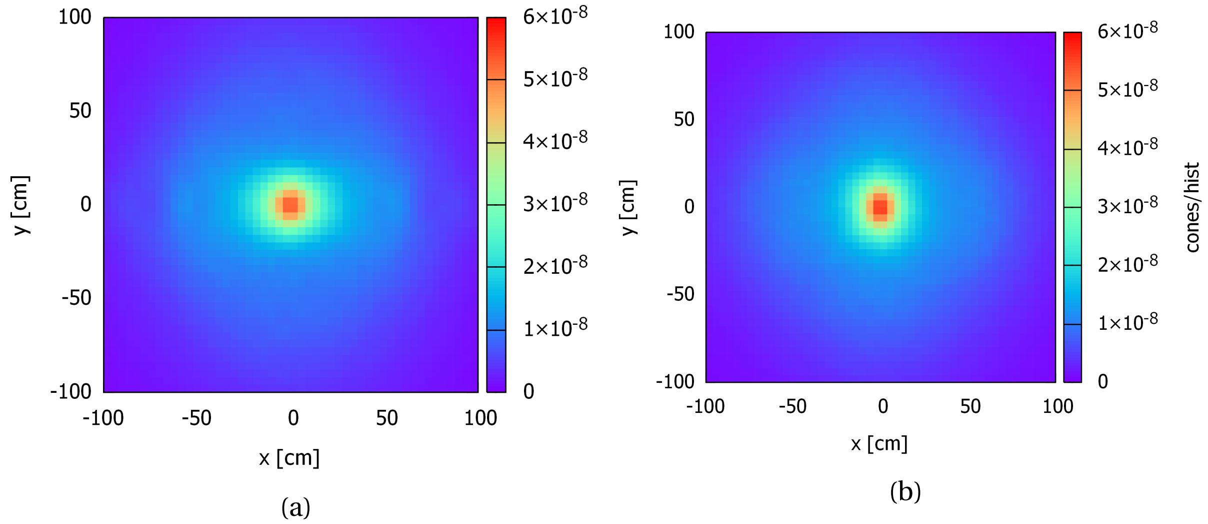

(a)

(b)

Figure 4.4: Reconstructed images using the Compton camera based on (a) two parallel layers and (b) two perpendicular layers. Results are shown for distances between layers of 15 cm. The bar colour indicates the number of cones per number of histories or γ-rays emitted by the source that pass over a given pixel. The source is an isotropic source of 662 keV located at 1 m from the scatter layer.

4.2 Crystal sizes

Crystal sizes are an important factor in the design of a Compton camera. Sizes of scatter detectors and absorber detectors have been studied separately. First, the thickness of scatter detectors was selected. In order to analyse the optimum size of scatter detectors, γ-rays that interact once in both layers, without taking into account deposited energy, were recorded. These kinds of events can be called single Compton scattering events (SCE). The crystal thickness of scatter detectors is selected according to the maximization of SCE. Once the size of scatter detectors has been chosen, the size of absorber detectors was decided based on the Compton camera efficiency, angular resolution and image resolution. The optimization of detector sizes was done by simulating γ-rays of 364 keV, 662 keV, 1173 keV and 1332 keV.

4.2.1 Size of scatter detectors

The evaluation of the thickness of scatter detectors using PENELOPE/penEasy simulations is explained in this section. The cartesian coordinate system was set at the centre of the scatter layer. The xy plane was centred at the scatter layer, with $z = 0$ at the centre of the scatter detectors. The z-axis was oriented towards the absorber plane, i.e. the absorber layer is placed in the half space with $z > 0$. The thickness of the scatter detectors was evaluated by increasing the crystal size along the z-axis without changing the crystal sizes of the absorber

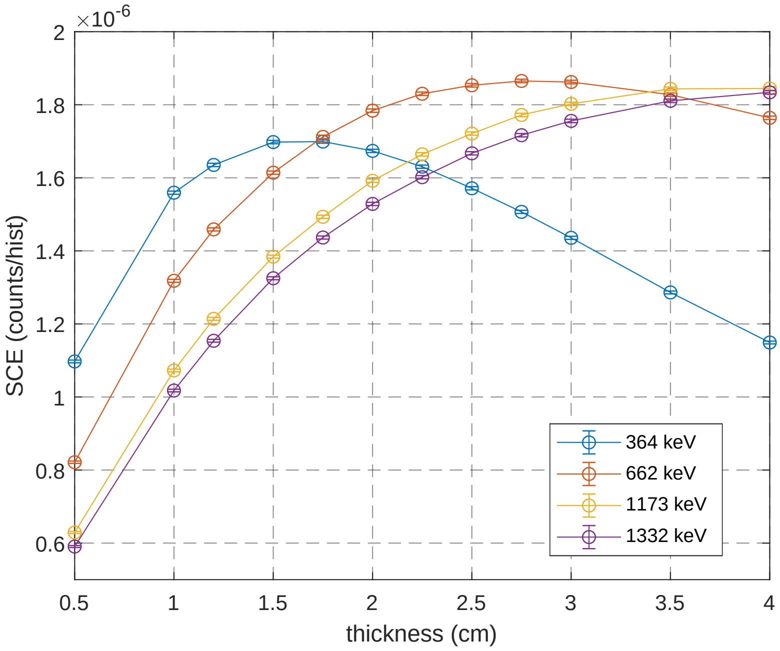

Figure 4.5: Single Compton scattering events (SCE) per γ-ray emitted by the source (histories). This quantity was calculated for different thicknesses of scatter detectors, while the size of absorber detectors was kept constant and equal to $1.2 \times 1.2 \times 10$ cm^3. Isotropic sources of 364 keV, 662 keV, 1173 keV and 1332 keV were simulated. Sources were placed at the centre and 1 metre away from the scatter layer. Energy windows are not considered.

detectors, which was $1.2 \times 1.2 \times 10$ cm^3. The isotropic sources of 364, 662, 1173 and 1332 keV were placed at the centre ($x = y = 0$) and 1 metre away from the surface of the scatter layer. Distance between layers was kept constant and equal to 10 cm because it was the distance chosen in the final design of the Compton camera, determined in Section 4.3.

Fig. 4.5 shows the number of γ-rays that interact once in both layers per γ-ray emitted by the source (histories), i.e., SCE were only included. Energy windows were not considered, i.e. events are only selected when γ-rays interact once in both layers and there is no limitation in energy. Fig. 4.5 shows the results for 364 keV, 662 keV, 1173 keV and 1332 keV. As can be seen, the thickness where the single Compton scattering events reach a maximum value depends on the energy of the incoming γ-ray. The SCE parameter reaches maximum values when the thicknesses of scatter detectors are around 1.5 cm, 2.5 cm, 3.5 cm and 4 cm for 364 keV, 662 keV, 1173 keV and 1332 keV, respectively. Therefore, in order to detect energies of 300 keV and to have a certain sensitivity to energies around 1000 keV, a thickness of 2 cm was chosen for scatter detectors. Table 4.1 shows the SCE when the optimum thickness is chosen for each energy and the SCE when a thickness of 2 cm is selected. It also shows the variation in the SCE when both thicknesses are considered. Decreases of 1.4%, 3.7%, 13.6% and 16.7% were

Table 4.1: Single Compton scattering events (SCE) obtained using the optimum thickness of scatter detectors and a thickness of 2 cm. The optimum thicknesses were 1.5 cm, 2.5 cm, 3.5 cm and 4 cm for 364 keV, 662 keV, 1173 keV and 1332 keV, respectively. The variation between the SCE obtained with the optimum thicknesses and the SCE obtained with a thickness of 2 cm is shown for each energy.

	SCE (counts/hist)			
	364 keV	662 keV	1173 keV	1332 keV
Optimum thickness	$1.698\cdot10^{-6}\pm5\cdot10^{-9}$	$1.853\cdot10^{-6}\pm5\cdot10^{-9}$	$1.844\cdot10^{-6}\pm5\cdot10^{-9}$	$1.834\cdot10^{-6}\pm5\cdot10^{-9}$
Thickness of 2 cm	$1.674\cdot10^{-6}\pm5\cdot10^{-9}$	$1.784\cdot10^{-6}\pm5\cdot10^{-9}$	$1.592\cdot10^{-6}\pm4\cdot10^{-9}$	$1.529\cdot10^{-6}\pm4\cdot10^{-9}$
Variation	−1.4%	−3.7%	−13.6%	16.7%

found for 364 keV, 662 keV, 1173 keV and 1332 keV, respectively.

The parameters that affect the Compton camera efficiency were described in Section 2.6.2. One of these parameters is the surface on the xy plane of the scatter and absorber layers. Increasing the surface of the scatter layer results in greater efficiency because the subtended solid angle of the scatter layer by the source is greater. In order to increase the surface of the scatter layer, the crystal cross-section is defined with a square shape of side 2 cm. In addition, it is usual for the manufacturer of these detectors to have a square section. The size of scatter detectors was thus set to $2\times2\times10$ cm^3.

4.2.2 Size of absorber detectors

The optimum size of absorber detector was determined by looking at efficiency, together with angular and image resolution obtained for a Compton camera made of four CsI(Tl) scintillator bars of $2\times2\times10$ cm^3 in the scatter layer and four CsI(Tl) scintillator bars of $L\times L\times10$ cm^3 in the absorber layer, where L is the side of the crystal cross-section. The distance between layers is kept constant and is equal to 10 cm. The study was done in the energy range of 360-1330 keV in order to analyse the effect of energy on Compton camera efficiency, together with angular and image resolution. Isotropic sources were placed at the centre ($x=y=0$) and 1 metre away from the surface of the scatter layer ($z=-101$ cm). The different sources emitted gamma-rays with the following energies: 364 keV, 662 keV, 1173 keV and 1332 keV.

Fig 4.6 shows the efficiencies of a Compton camera for different sizes of absorber detectors, $L\times L\times10$ cm^3. As expected, efficiency increases with L. The highest efficiency

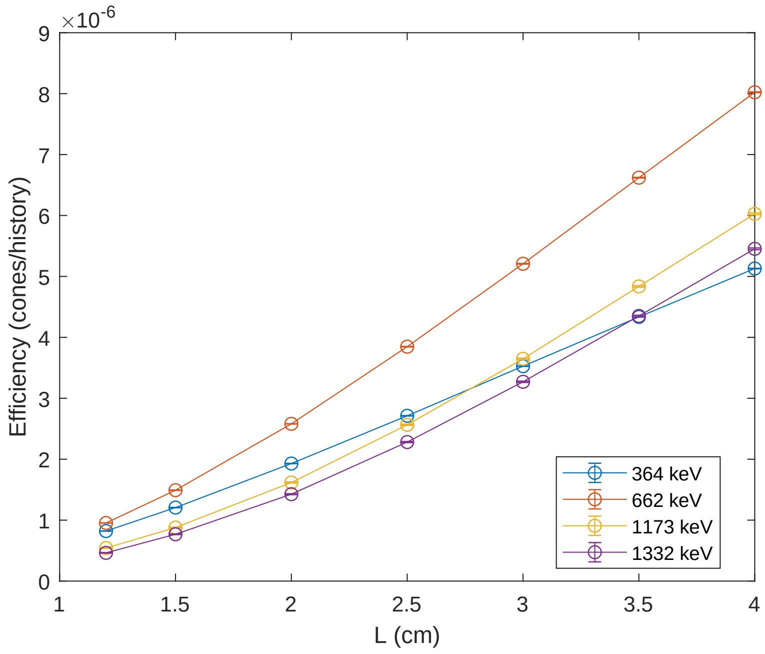

Figure 4.6: Efficiency of a Compton camera consisting of CsI(Tl) scintillators bars of $2 \times 2 \times 10$ cm^3 in the scatter layer and CsI(Tl) scintillator bars of $L \times L \times 10$ cm^3 in the absorber layer. The distance between layers was kept constant and equal to 10 cm. Isotropic sources of 364 keV, 662 keV, 1173 keV and 1332 keV were simulated. Sources were placed at the centre and 1 metre away from the scatter layer.

is obtained for 662-keV γ-rays because the number of SCE is the highest for 662 keV when a thickness of 2 cm is used in the scatter layer (see Fig. 4.5).

Fig. 4.7 shows the angular resolution for different sizes of absorber detectors simulating γ-ray energies of (a) 364 keV, (b) 662 keV, (c) 1173 keV and (d) 1332 keV. In order to analyse the different uncertainty contributions to the ARM, the corresponding $FWHM$s were calculated considering i) the uncertainties in the crystal cross-section, u_{xz}, ii) position resolution along the bar, σ_y, and iii) all the uncertainty sources, i.e., both energy and position resolution in all directions. Doppler broadening was always taken into account. Fig. 4.7 shows that the total angular resolution increases with L, which is due to uncertainties in the crystal cross-section, u_{xz}. This behaviour is shown for the four energies. These uncertainties increased with L because the position of the gamma-ray interactions in the crystal cross-section is unknow and it was calculated using random numbers generated by a uniform distribution (see Section 2.5.1). One can observe from Fig. 4.7 that angular resolution improves with energy. This is due to the fact that both energy and position resolution along the bar, σ_y, improves with deposited energies.

Image resolution, $FWHM_x$ and $FWHM_y$, is plotted in Fig. 4.8 for γ-ray energies of (a)

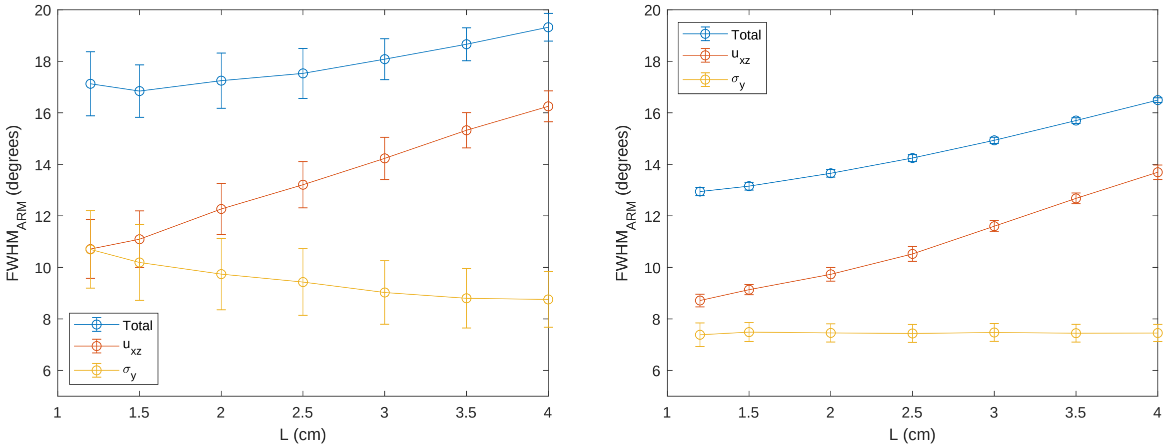

(a) 364 keV (b) 662 keV

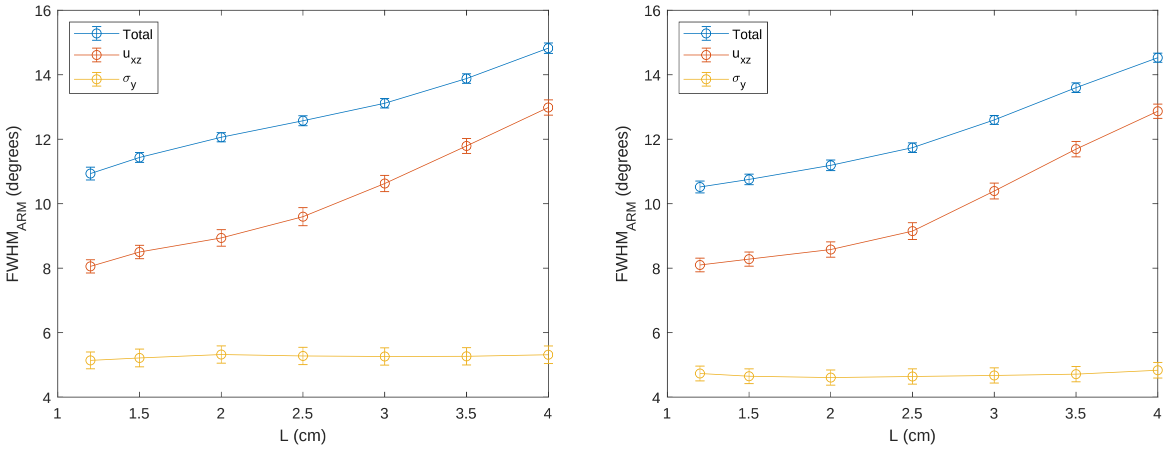

(c) 1173 keV (d) 1332 keV

Figure 4.7: The angular resolution, $FWHM_{ARM}$, was calculated considering all the uncertainties that affect the Compton camera (Total), the uncertainties in the crystal cross-section (u_{xz}) and the position resolution along the bar (σ_y). The geometry consists of four CsI(Tl) scintillators bars of $2 \times 2 \times 10$ cm^3 in the scatter layer and four CsI(Tl) scintillator bars of $L \times L \times 10$ cm^3 in the absorber layer. The distance between layers was kept constant and equal to 10 cm. Gamma-ray sources of (a) 364 keV, (b) 662 keV, (c) 1173 keV and (d) 1332 keV were simulated. Sources were placed at the centre and 1 metre away from the scatter layer

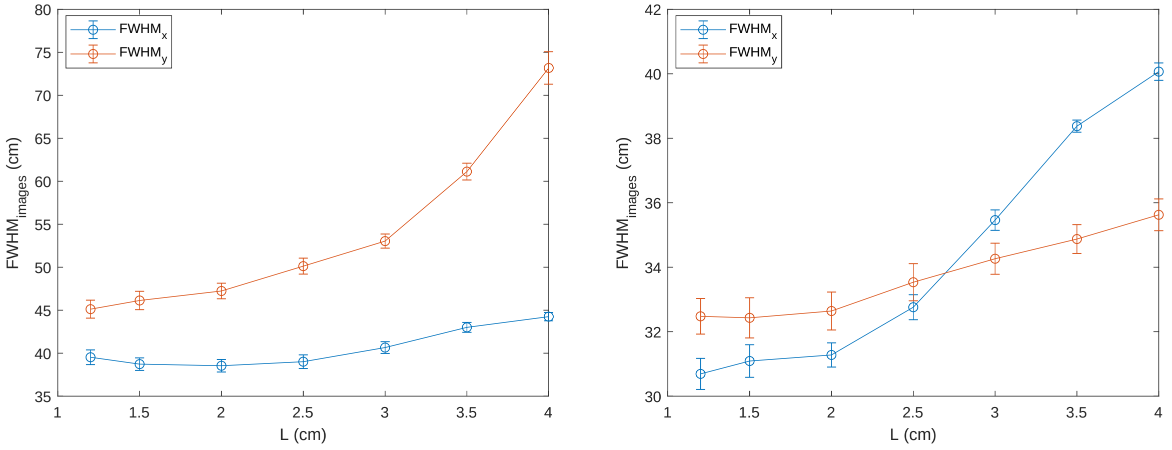

(a) 364 keV

(b) 662 keV

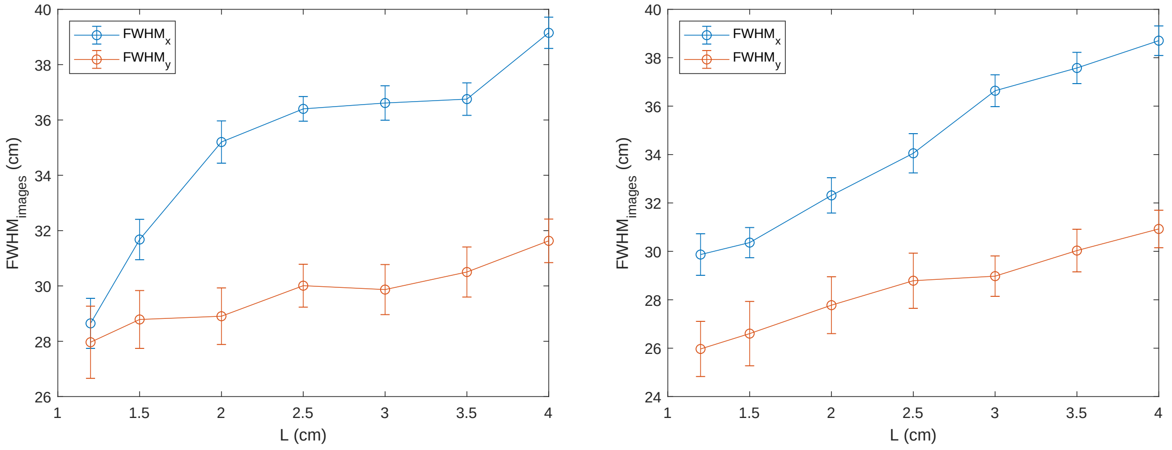

(c) 1173 keV

(d) 1332 keV

Figure 4.8: Image resolution along both axes, $FWHM_x$ and $FWHM_y$, are plotted for different sizes of absorber detectors. The geometry consists of four CsI(Tl) scintillators bars of $2 \times 2 \times 10$ cm^3 in the scatter layer and four CsI(Tl) scintillator bars of $L \times L \times 10$ cm^3 in the absorber layer. The distance between layers was kept constant and equal to 10 cm. Isotropic sources of (a) 364 keV, (b) 662 keV, (c) 1173 keV and (d) 1332 keV were simulated. Sources were located at the centre and 1 metre away from the scatter layer

Table 4.2: Comparison between two Compton cameras. One has four CsI(Tl) detectors of $1.2 \times 1.2 \times 10$ cm^3 in the absorber layer, while the other has four CsI(Tl) detectors of $2 \times 2 \times 10$ cm^3 in the same layer. Both Compton cameras have 4 CsI(Tl) scintillator bars of $2 \times 2 \times 10$ cm^3 in the scatter layer. Efficiency, angular resolution ($FWHM_{ARM}$) and image resolution ($FWHM_x$ and $FWHM_y$) are compared for different energies (364 keV, 662 keV, 1173 keV and 1332 keV)

	364 keV		
	$1.2 \times 1.2 \times 10$ cm^3	$2 \times 2 \times 10$ cm^3	Variation
Efficiency (cones/hist)	$8.209 \cdot 10^{-7} \pm 1.7 \cdot 10^{-9}$	$1.929 \cdot 10^{-6} \pm 3 \cdot 10^{-9}$	+135%
$FWHM_{ARM}$ (degrees)	17.1 ± 1.2	17.2 ± 1.1	–
$FWHM_x$ (cm)	39.5 ± 0.9	38.5 ± 0.7	–
$FWHM_y$ (cm)	45.1 ± 1.1	47.2 ± 0.9	+4.7%
	662 keV		
	$1.2 \times 1.2 \times 10$ cm^3	$2 \times 2 \times 10$ cm^3	Variation
Efficiency (cones/hist)	$9.531 \cdot 10^{-7} \pm 1.8 \cdot 10^{-9}$	$2.580 \cdot 10^{-6} \pm 3 \cdot 10^{-9}$	+170%
$FWHM_{ARM}$ (degrees)	12.94 ± 0.16	13.65 ± 0.15	+5.5%
$FWHM_x$ (cm)	30.7 ± 0.5	31.3 ± 0.4	–
$FWHM_y$ (cm)	32.5 ± 0.6	32.6 ± 0.6	–
	1173 keV		
	$1.2 \times 1.2 \times 10$ cm^3	$2 \times 2 \times 10$ cm^3	Variation
Efficiency (cones/hist)	$5.42 \cdot 10^{-7} \pm 4 \cdot 10^{-9}$	$1.617 \cdot 10^{-6} \pm 8 \cdot 10^{-9}$	+198%
$FWHM_{ARM}$ (degrees)	10.93 ± 0.19	12.06 ± 0.14	+10.3%
$FWHM_x$ (cm)	28.6 ± 0.9	35.2 ± 0.8	+23%
$FWHM_y$ (cm)	28.0 ± 1.3	28.9 ± 1.1	–
	1332 keV		
	$1.2 \times 1.2 \times 10$ cm^3	$2 \times 2 \times 10$ cm^3	Variation
Efficiency (cones/hist)	$4.63 \cdot 10^{-7} \pm 4 \cdot 10^{-9}$	$1.426 \cdot 10^{-6} \pm 7 \cdot 10^{-9}$	+208%
$FWHM_{ARM}$ (degrees)	10.52 ± 0.18	11.19 ± 0.16	+6.4%
$FWHM_x$ (cm)	29.9 ± 0.9	32.3 ± 0.8	+8%
$FWHM_y$ (cm)	26.0 ± 1.1	27.8 ± 1.2	–

364 keV, (b) 662 keV, (c) 1173 keV and (d) 1332 keV. In general, image resolution worsens when the crystal size is increased. Table 4.2 shows how efficiency, angular resolution and image resolution varies using CsI(Tl) detectors of $1.2 \times 1.2 \times 10$ cm^3 and $2 \times 2 \times 10$ cm^3 in the absorber layer, with CsI(Tl) detectors of $2 \times 2 \times 10$ cm^3 in the scatter layer. The size of absorber detectors is set to $2 \times 2 \times 10$ cm^3 because the use of these detectors increases efficiency between 135 and 200% with a worsening of the angular resolution between 5 and 10%, depending on the energy and a decline in the image resolution between 4 and 20%, also depending on the energy. In addition, a Compton camera consisting of CsI(Tl) detectors of only $2 \times 2 \times 10$ cm^3 will probably mean that mounting the Compton camera on a drone would be easier.

4.3 Distance between layers

The distance, d, between the scatter and absorber layers plays an important role in the performance of a Compton camera. Increasing d causes a reduction in efficiency, but angular resolution improves. Therefore, the distance between layers should be optimized. Efficiency, angular resolution and image resolution have been analysed for different distances. The Compton camera consists of eight CsI(Tl) scintillator bars of $2 \times 2 \times 10$ cm^3. The study was done using point sources that emit gamma-rays of 364 keV, 662 keV, 1173 keV and 1332 keV placed at 1 m from the surface of the scatter detectors.

Fig. 4.9 shows how the Compton camera efficiency decreases with distance between layers, d. The angular resolution for different distances, d, is shown in Fig. 4.10. It is calculated by including the influence of different sources of uncertainty: i) uncertainties in the crystal cross-section, u_{xz}, and ii) position resolution along the bar, σ_y. The angular resolution when all uncertainties are considered (both energy and position resolution in the three coordinates) was also calculated and is shown in Fig. 4.10. Doppler broadening has always been taken into account. Angular resolution was calculated for the γ-ray energies of (a) 364 keV, (b) 662 keV, (c) 1173 keV and (d) 1332 keV. Fig. 4.10 shows how angular resolution improves with increasing distance between layers.

Image resolution along both axes, $FWHM_x$ and $FWHM_y$, are plotted in Fig. 4.11 for (a) 364 keV, (b) 662 keV, (c) 1173 keV and (d) 1332 keV. As we can see, $FWHM_x$ and $FWHM_y$ decrease with distance between layers. However, when a source of 364 keV is simulated, the $FWHM_y$ increases rapidly for distances between layers $d > 10$ cm. An energy threshold of 20 keV was implemented in simulations in order to simulate the experimental detector threshold, which reduces the noise. This means that deposited energies lower than 20 keV were not considered. Scattering angles with $\theta_c < 23°$ were not accepted for incident γ-rays of 364 keV. As the distance between layers increases, the accepted γ-rays would be scattered at smaller angles. For example, when d is set to 8 cm, 60% of γ-rays that interact once in both layers are not considered because their scattering angles are lower than 23°, while if this distance is 12 cm the proportion of events that are not considered grows to 75.6%. This causes images to become noisier on the y axis when $d > 10$ cm. Note that this did not happen for the other energies analysed because the limitation on the scattering angle is lower. This limit was 13°, 7° and 6° for γ-ray energies of 662 keV, 1173 keV and 1332 keV, respectively.

Therefore, the distance between layers was set to 10 cm in order to keep image

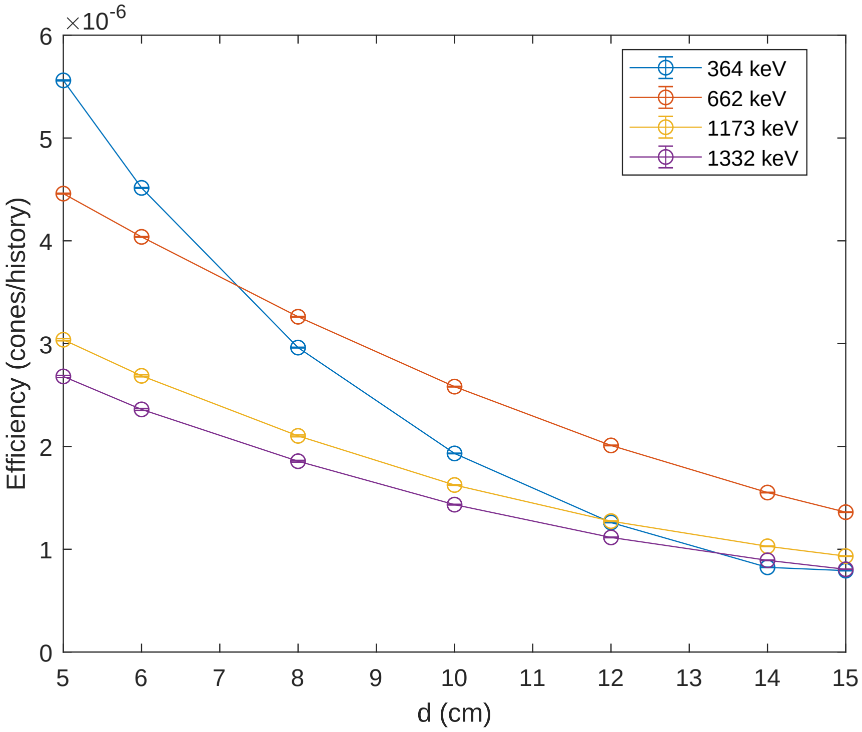

Figure 4.9: Efficiency of a Compton camera consisting of CsI(Tl) scintillators bars of $2 \times 2 \times 10$ cm^3 in both layers. Results are plotted for different distances *d* between layers (from surface to surface). Sources of 364 keV, 662 keV, 1173 keV and 1332 keV were simulated. Sources were placed at the centre and 1 metre away from the scatter layer.

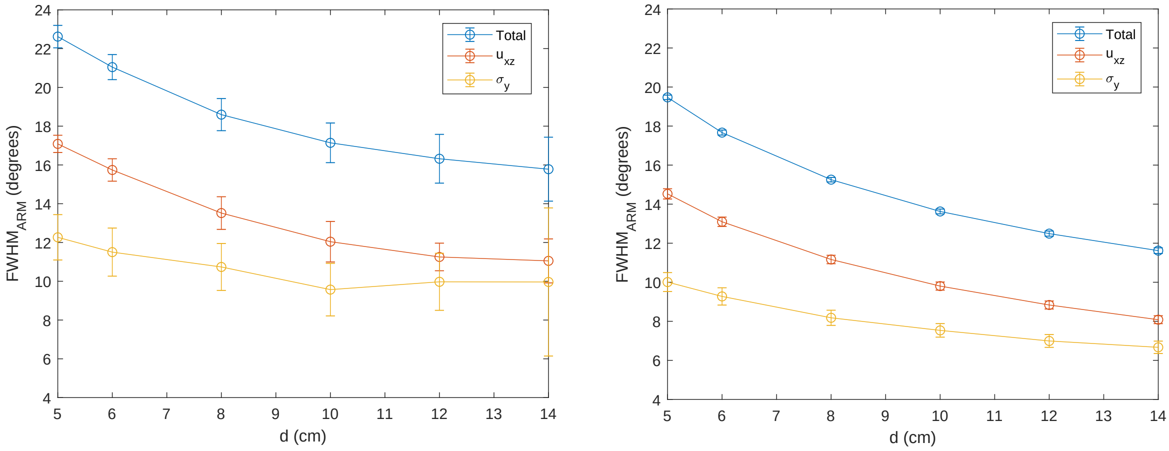

(a) 364 keV

(b) 662 keV

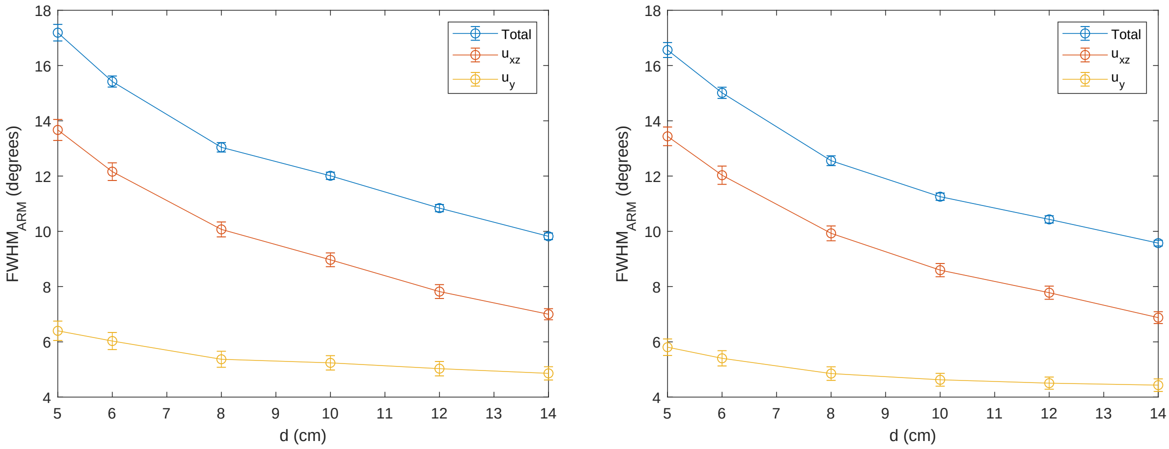

(c) 1173 keV

(d) 1332 keV

Figure 4.10: Angular resolution, $FWHM_{ARM}$, of a Compton camera consisting of two layers with four CsI(Tl) scintillators bars of $2 \times 2 \times 10$ cm^3 each. The angular resolution was evaluated for different distances d between layers (from surface to surface). Angular resolution was calculated by considering all the uncertainties that affect the Compton camera (Total), the uncertainties in the crystal cross-section (u_{xz}) and the position resolution along the bar (σ_y). Results were plotted by simulating gamma-rays of different energies: (a) 364 keV, (b) 662 keV, (c) 1173 keV and (d) 1332 keV. Sources were placed at the centre and 1 metre away from the scatter layer.

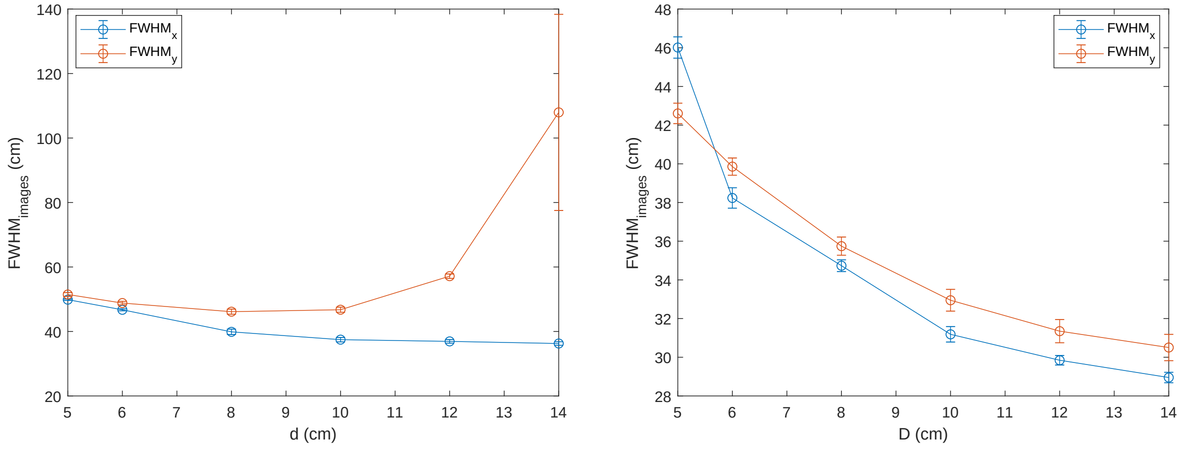

(a) 364 keV

(b) 662 keV

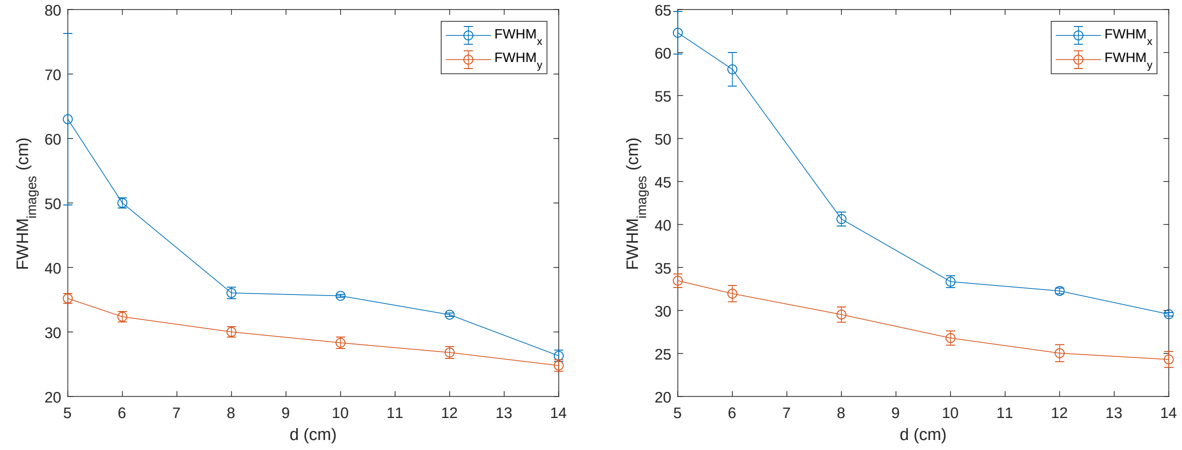

(c) 1173 keV

(d) 1332 keV

Figure 4.11: Image resolution along both axes. $FWHM_x$ and $FWHM_y$ are plotted for different distances d between layers (from surface to surface). The geometry consists of two layers of four CsI(Tl) scintillators bars of $2 \times 2 \times 10$ cm^3 each. Results were plotted for four different γ-ray energies: (a) 364 keV, (b) 662 keV, (c) 1173 keV and (d) 1332 keV. Sources were placed at the centre and 1 metre away from the scatter layer.

Table 4.3: Compton camera efficiency, angular resolution ($FWHM_{ARM}$) and image resolution along both axes ($FWHM_x$ and $FWHM_y$) obtained for a Compton camera consisting of two layers of CsI(Tl) scintillator detectors of 2 × 2 × 10 cm^3. The distance between layers was 10 cm. Results are shown for energies of 364 keV, 662 keV, 1173 keV and 1332 keV. Sources are placed at the centre ($x = y = 0$) and 1 metre away from the scatter layer.

	364 keV	662 keV	1173 keV	1332 keV
Efficiency (cones/hist)	$1.932 \cdot 10^{-6} \pm 3 \cdot 10^{-9}$	$2.582 \cdot 10^{-6} \pm 3 \cdot 10^{-9}$	$1.625 \cdot 10^{-6} \pm 4 \cdot 10^{-9}$	$1.434 \cdot 10^{-6} \pm 3 \cdot 10^{-9}$
$FWHM_{ARM}$ (degrees)	17.1 ± 1.1	13.63 ± 0.12	12.01 ± 0.13	11.25 ± 0.13
$FWHM_x$ (cm)	37.5 ± 0.7	31.2 ± 0.4	35.6 ± 0.2	33.35 ± 0.7
$FWHM_y$ (cm)	46.7 ± 0.8	32.9 ± 0.6	28.3 ± 0.9	26.8 ± 0.9

resolution between 30 and 47 cm for the energy range analysed. Table 4.3 shows the main characteristics of a Compton camera composed of two layers of CsI(Tl) scintillator bars of 2 × 2 × 10 cm^3 separated by 10 cm when sources were placed at the centre ($x = y = 0$) and 1 metre away from the scatter layer.

4.4 Conclusions

The design of a Compton camera consisting of two layers was done using PENELOPE/penEasy simulations. The geometry arrangement, size of detectors and distance between layers were optimized based on Compton camera efficiency, angular resolution and image resolution.

A comparison between results obtained with two geometric arrangements of detectors was made. The scatter and absorber layers were arranged both in a parallel and perpendicular configuration. Since no significant differences were observed between both configurations the parallel configuration was chosen. Optimization was then carried out with a Compton camera based on two parallel layers of CsI(Tl) scintillator detectors, called the scatter and absorber layers.

First, the sizes of scatter and absorber detectors were optimized separately. This study was done by simulating the energies corresponding to typical radionuclides that cover a wide energy range in the environmental research of ^{131}I (364 keV), ^{137}Cs (662 keV) and ^{60}Co (1173 keV and 1332 keV). The optimum thickness of detectors from the scatter layer was calculated based on the number of γ-rays that interact once in both layers, which was called single Compton scattering events (SCE). The optimum thickness depends on the energy of the incident γ-ray. The optimum thickness values of scatter detectors were approximately 1.5 cm, 2.5 cm, 3.5 cm and 4 cm for 364 keV, 662 keV, 1173 keV and 1332 keV, respectively. A thickness of 2 cm was chosen to avoid loss of sensitivity for energies around 300 keV. Comparing the SCE obtained using the optimum thickness and a thickness of 2 cm, lower values of 1.4%, 3.7%, 13.6% and 16.7% were found for 364 keV, 662 keV, 1173 keV and 1332 keV, respectively. In order to increase efficiency, the crystal cross-section was defined as a square of side 2 cm. The size of scatter detectors was set to $2 \times 2 \times 10$ cm^3.

Once the size of scatter detectors was chosen, the size of the absorber detectors was evaluated based on efficiency, angular resolution and image resolution. Efficiency increases with the size of absorber detectors. Angular resolution worsens with size due to the uncertainties in the crystal cross-section. Image resolution tends to worsen by increasing the size of absorber detectors. The size of absorber detectors was set to $2 \times 2 \times 10$ cm^3 in order to increase efficiency to around 150% with a worsening of image resolution between 4 and 20%, depending on energy.

The optimum distance between the scatter and absorber layers was also analysed based on efficiency, angular resolution and image resolution. Sources of 364 keV, 662 keV, 1173 keV and 1332 keV were simulated to this end. The analysis was carried out with CsI(Tl) scintillator bars of $2 \times 2 \times 10$ cm^3. Efficiency decreases with distance between layers, while angular resolution improves. Image resolution also improves, but, for distances greater than 10 cm, the image resolution along the y axis increases rapidly when a source of 364 keV was simulated. This distance was thus set to 10 cm. The optimum Compton camera consists of two parallel layers separated by 10 cm. Each layer has 4 CsI(Tl) scintillator bars of $2 \times 2 \times 10$ cm^3.

Chapter 5

Characterization of the Compton camera

In this chapter the characterization of a Compton camera consisting of $2 \times 2 \times 10$ cm^3 CsI(Tl) scintillator bars was done by simulating sources of 364 keV, 662 keV, and 1173 keV and 1332 keV. These energies correspond to the main energy lines emitted by ^{131}I, ^{137}Cs and ^{60}Co sources. Henceforth, when we refer to these sources we mean that their main energy lines were simulated.

The parameters that are studied in the following sections are the Compton camera field of view (FOV) and minimum number of cones to locate a source. The variation of efficiency, angular and image resolution with distance between the source and the Compton camera was also studied. The angular resolution of a Compton camera from the literature was also compared with the results presented in this thesis. Furthermore, the ability to locate several point and surface sources using the back-projection method is also analysed.

5.1 Field of View

In order to calculate the FOV, simulations with isotropic ^{131}I, ^{137}Cs and ^{60}Co sources were done. Sources were moved on the xy plane, keeping their position on the z axis constant and equal to -100 cm. The cartesian coordinate system was chosen in such a way that the plane $z = 0$ is sited at the centre of the scatter detectors. The z axis is oriented towards the absorber plane, i.e. the absorber layer is placed in the half space with $z > 0$. The plane $z = -100$ cm, where the sources are moved, is then parallel to the scatter layer.

The FOV depends on the energy of the incident γ-ray because the energy windows used to select the events to reconstruct images are different for each source. Energy windows that

Table 5.1: Range of deposited energies that are allowed in scatter detectors for the four energies analysed (364 keV, 662 keV, 1173 keV and 1332 keV) for a Compton camera consisting of eight detectors. The range of accepted scattering angles calculated with the Compton equation (Eq. 2.15) is also shown.

Gamma-ray energy (keV)	Range of energy (keV)	Range of scattering angles (degrees)
364	$E < 125$	$\theta_c < 75$
662	$E < 150$	$\theta_c < 39$
1173	$E < 170; 260 < E < 490$	$\theta_c < 22; 29 < \theta_c < 47$
1332	$E < 170; 280 < E < 600$	$\theta_c < 19; 26 < \theta_c < 47$

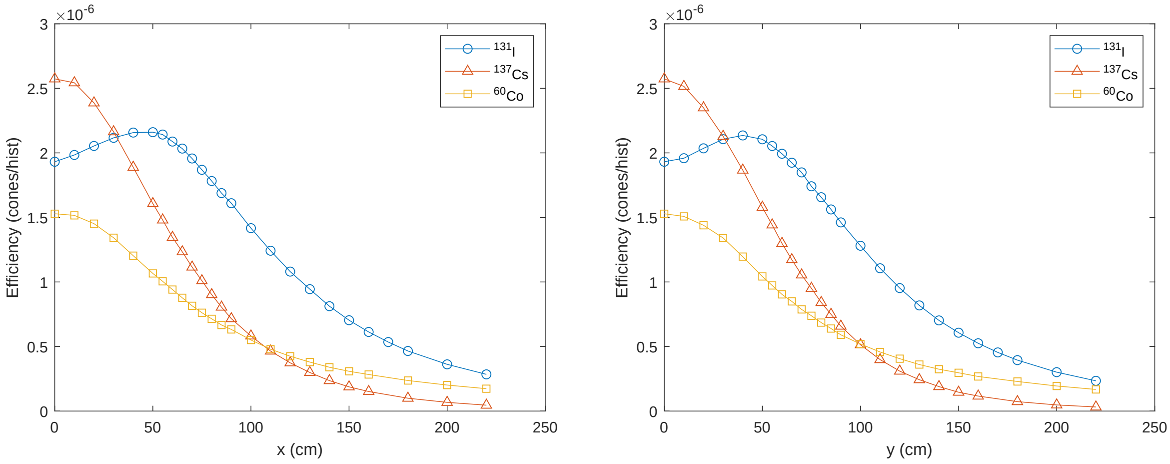

(a) (b)

Figure 5.1: Compton Camera efficiency when ^{131}I, ^{137}Cs and ^{60}Co sources are moved on the (a) x and (b) y axes. The distance between the scatter layer and sources on the z axis is 100 cm

are used in the calculation of images have previously been described in Section 2.6.1. Two energy windows are defined for each γ-ray energy emitted by the sources. First, those γ-rays that interact in both layers and deposit their entire energy are selected. Second, only those γ-rays that deposit energy in a certain range in the scatter detectors are accepted. These ranges of energies are shown in Table 5.1. Setting a limitation on the deposited energy in the scatter detector implies a limitation on the Compton scattering angle. Using the Compton equation, the thresholds in the Compton scattering angles are calculated and shown in Table 5.1. As we can see, γ-rays of 364 keV are allowed to scatter at larger angles. This means that the FOV of the Compton camera is wider for sources of ^{131}I than for the other sources analysed.

Efficiencies of the Compton camera for the simulated sources are shown in Fig. 5.1. ^{131}I, ^{137}Cs and ^{60}Co sources are moved away from the centre on the (a) x and (b) y axes. In general, efficiencies decrease when sources are moved away from the centre. As we can see, efficiency depends on the energy because the threshold in the Compton scattering angles is different for each energy. Due to the fact that the scattering angles allowed are larger for ^{131}I, efficiency is higher when this source is moved away from the centre. However, the efficiency obtained when a source of ^{137}Cs is placed at the centre is higher than for the other analysed sources. As was shown in Figs. 4.5 and 4.6 from Section 4.2, efficiency is the highest for 662 keV for detectors with a cross-section of 2×2 cm^2.

The reconstructed images from the simulated gamma-rays emitted by isotropic ^{131}I, ^{137}Cs and ^{60}Co sources are shown in Figs 5.2, 5.3, 5.4, 5.5, 5.6 and 5.7. Sources were placed at different positions along the x and y axes. The bar colour of images indicates the number of cones per number of histories that pass over a given pixel, where histories are the number of γ-rays emitted by the source. About 10^{11} histories were emitted by the three isotropic sources.

Figs. 5.2 and 5.3 show the images obtained for a ^{131}I source which is moved away from the centre along the x and y axes, respectively. Fig. 5.2 shows images when a ^{131}I source is placed at a) $x = 50$ cm (26.6°), $y = 0$, b) $x = 100$ cm (45°), $y = 0$ c) $x = 150$ cm (56.3°), $y = 0$, d) $x = 170$ cm (59.5°), $y = 0$, e) $x = 180$ cm (60.9°), $y = 0$ and f) $x = 190$ cm (62.2°), $y = 0$, while Fig. 5.3 shows images when the ^{131}I source is placed at a) $x = 0$, $y = 50$ cm (26.6°), b) $x = 0$, $y = 100$ cm (45°), c) $x = 0$, $y = 150$ cm (56.3°), d) $x = 0$, $y = 170$ cm (59.5°), e) $x = 0$, $y = 180$ cm (60.9°) and f) $x = 0$, $y = 190$ cm (62.2°). Figs. 5.4 and 5.5 show the images when a ^{137}Cs source is simulated at different positions. Fig. 5.4 shows images when a ^{137}Cs source is placed at a) $x = 50$ cm (26.6°), $y = 0$, b) $x = 80$ cm (38.7°), $y = 0$, c) $x = 100$ cm (45°), $y = 0$ and d) $x = 120$ cm (50.2°), $y = 0$, while Fig. 5.5 shows images when the ^{137}Cs source is placed at a) $x = 0$, $y = 50$ cm (26.6°), b) $x = 0$, $y = 80$ cm (38.7°), c) $x = 0$, $y = 100$ cm (45°) and d) $x = 0$, $y = 120$ cm (50.2°). Images of a ^{60}Co source are shown in Figs. 5.6 and 5.7 for a movement on the x and y axes, respectively. Fig. 5.6 shows images when the ^{60}Co source is placed at a) $x = 50$ cm (26.6°), $y = 0$, b) $x = 80$ cm (38.7°), $y = 0$, c) $x = 100$ cm (45°), $y = 0$ and d) $x = 110$ cm (47.7°), $y = 0$, while Fig. 5.7 shows images when the source is placed at a) $x = 0$, $y = 50$ cm (26.6°), b) $x = 0$, $y = 80$ cm (38.7°), c) $x = 0$, $y = 100$ cm (45°) and d) $x = 0$, $y = 110$ cm (47.7°). The position of the sources is indicated in the images with circles. The distance between the surface of the scatter layer and sources on the z axis is kept constant and equal to 100 cm in all simulations.

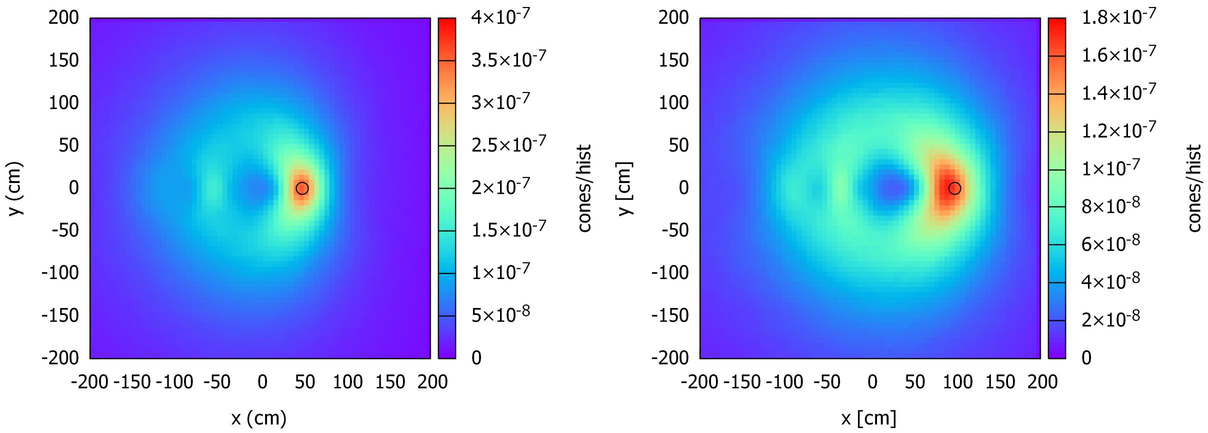

(a) $x = 50$ cm (26.6°), $y = 0$ (b) $x = 100$ cm (45°), $y = 0$

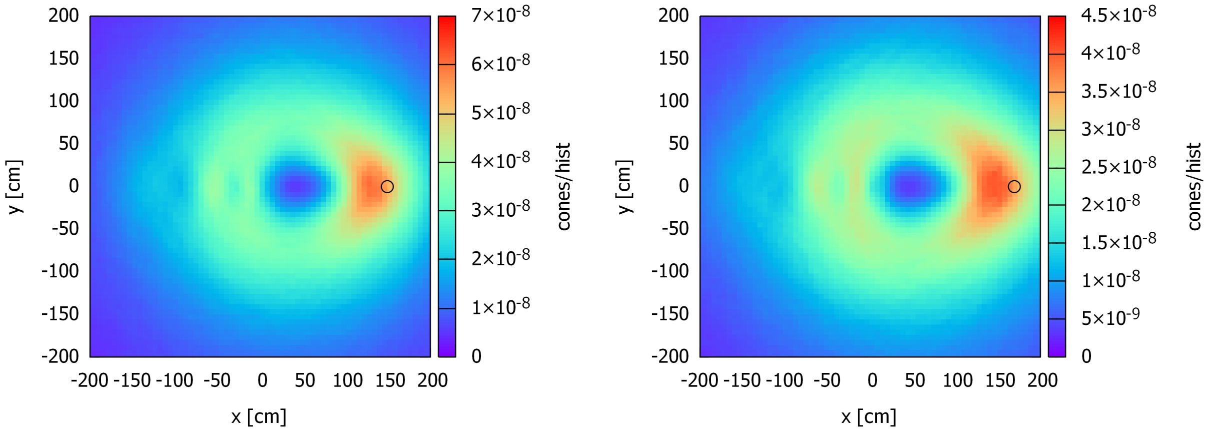

(c) $x = 150$ cm (56.3°), $y = 0$ (d) $x = 170$ cm (59.5°), $y = 0$

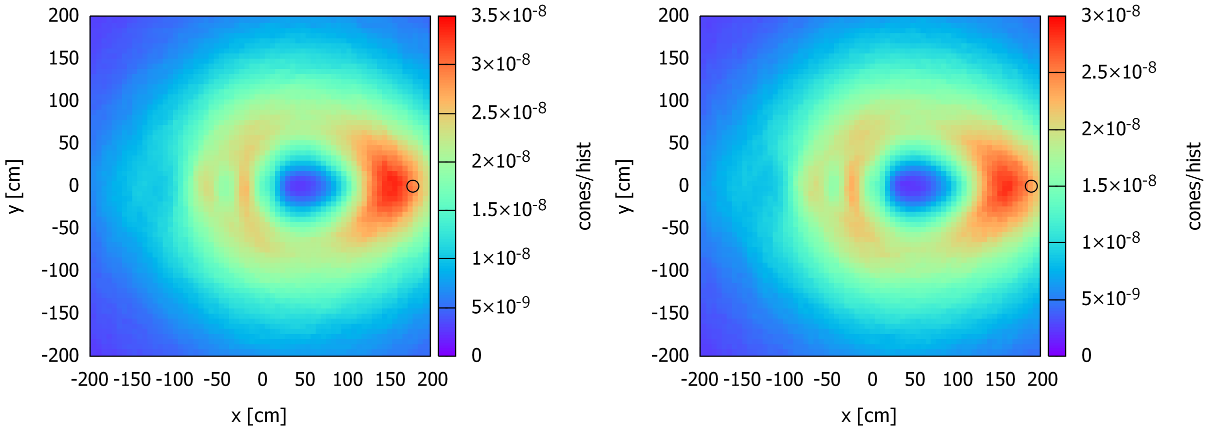

(e) $x = 180$ cm (60.9°), $y = 0$ (f) $x = 190$ cm (62.2°), $y = 0$

Figure 5.2: Reconstructed images for the simulated γ-rays of 364 keV. The source is placed at (a) $x = 50$ cm (26.6°), $y = 0$, (b) $x = 100$ cm (45°), $y = 0$ (c) $x = 150$ cm (56.3°), $y = 0$, (d) $x = 170$ cm (59.5°), $y = 0$, (e) $x = 180$ cm (60.9°), $y = 0$ and (f) $x = 190$ cm (62.2°), $y = 0$. The position of the source is indicated by circles. Distance between the surface of the scatter layer and the source on the z-axis is 100 cm. The bar colour indicates the number of cones per number of histories or γ-rays emitted by the source that pass over a given pixel

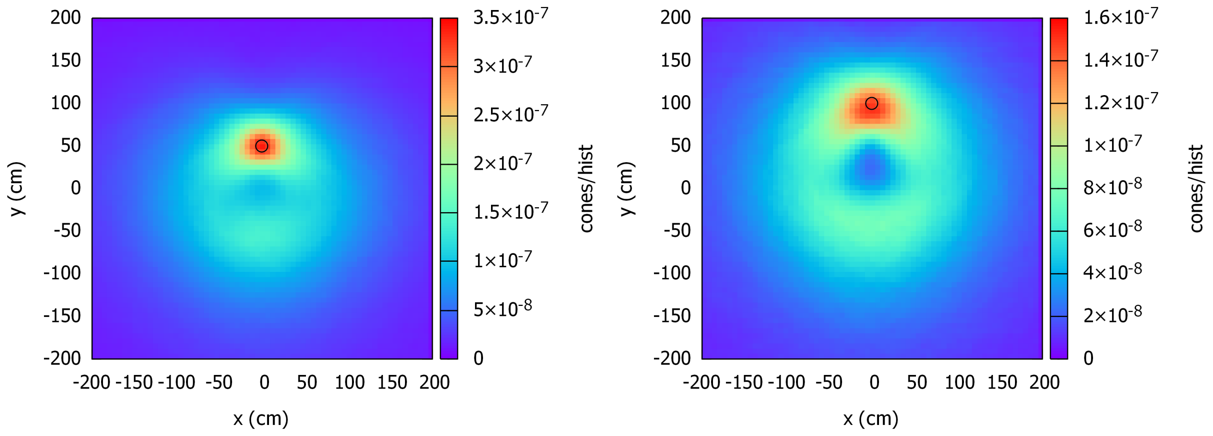

(a) $x = 0$, $y = 50$ cm (26.6°) (b) $x = 0$, $y = 100$ cm (45°)

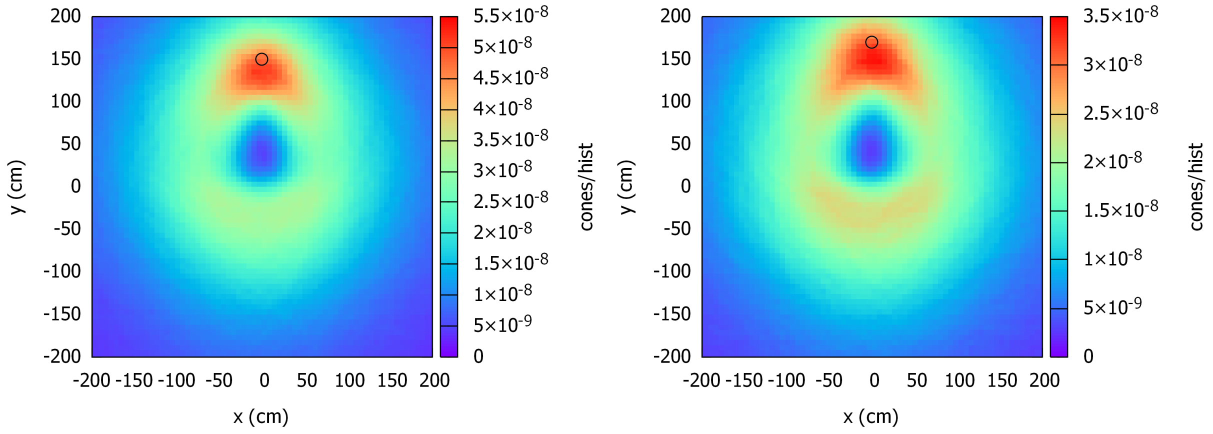

(c) $x = 0$, $y = 150$ cm (56.3°) (d) $x = 0$, $y = 170$ cm (59.5°)

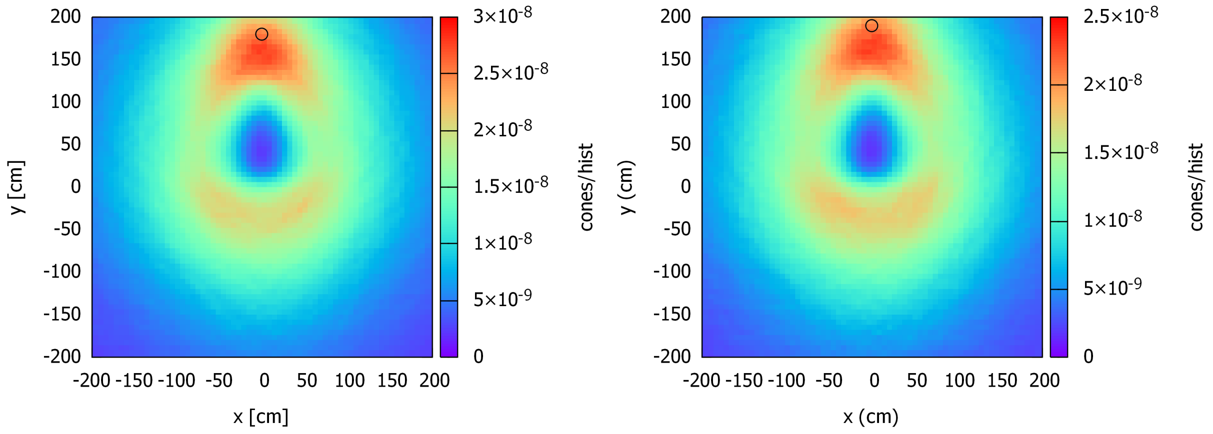

(e) $x = 0$, $y = 180$ cm (60.9°) (f) $x = 0$, $y = 190$ cm (62.2°)

Figure 5.3: Reconstructed images for the simulated γ-rays of 364 keV. The source is placed at (a) $x = 0$, $y = 50$ cm (26.6°), (b) $x = 0$, $y = 100$ cm (45°), (c) $x = 0$, $y = 150$ cm (56.3°), (d) $x = 0$, $y = 170$ cm (59.5°), (e) $x = 0$, $y = 180$ cm (60.9°) and (f) $x = 0$, $y = 190$ cm (62.2°). The position of the sources is indicated by circles. Distance between the surface of the scatter layer and the source on the z-axis is 100 cm. The bar colour indicates the number of cones per number of histories or γ-rays emitted by the source that pass over a given pixel

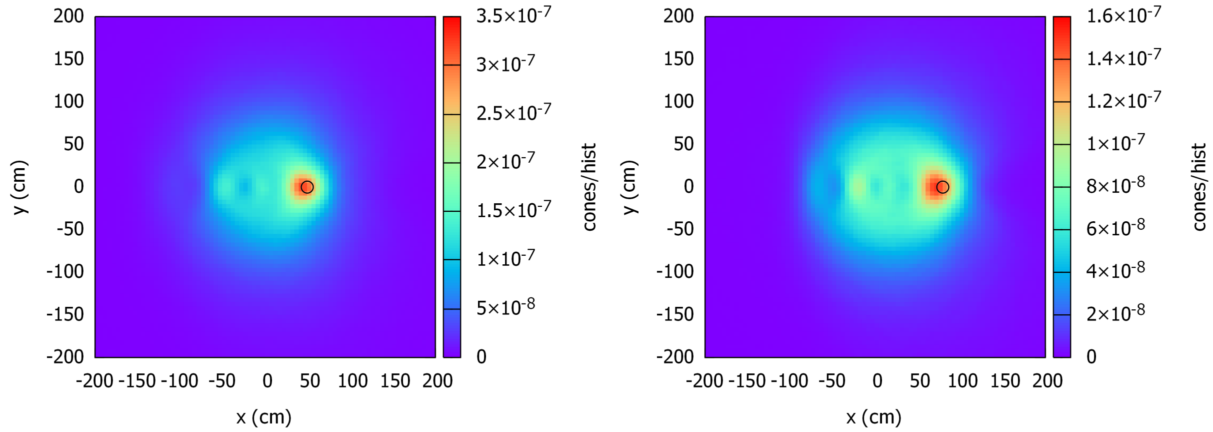

(a) $x = 50$ cm (26.6°), $y = 0$

(b) $x = 80$ cm (38.7°), $y = 0$

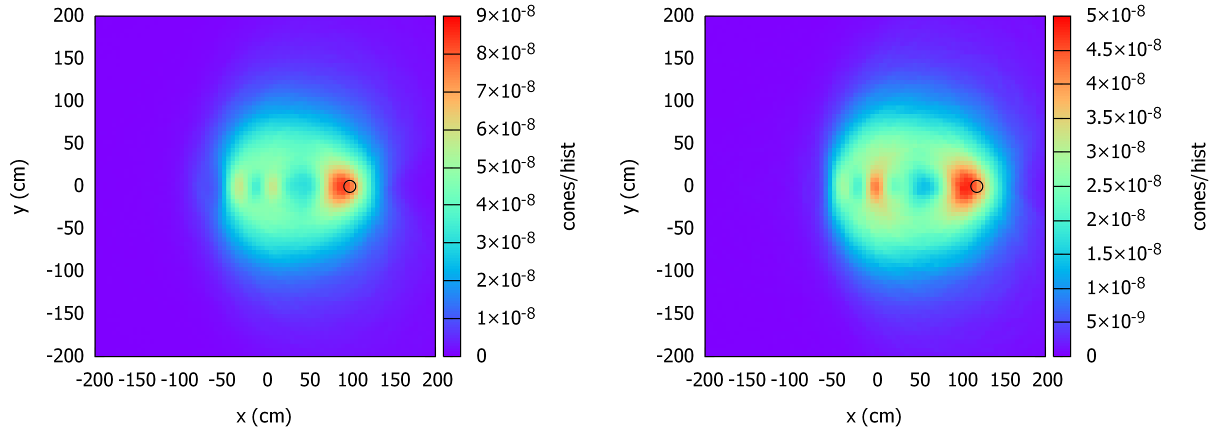

(c) $x = 100$ cm (45°), $y = 0$

(d) $x = 120$ cm (50.2°), $y = 0$

Figure 5.4: Reconstructed images for the simulated γ-rays of 662 keV. The source is placed at (a) $x = 50$ cm (26.6°), $y = 0$, (b) $x = 80$ cm (38.7°), $y = 0$, (c) $x = 100$ cm (45°), $y = 0$ and (d) $x = 120$ cm (50.2°), $y = 0$. The position of the sources is indicated by circles. Distance between the surface of the scatter layer and the source on the z-axis is 100 cm. The bar colour indicates the number of cones per number of histories or γ-rays emitted by the source that pass over a given pixel

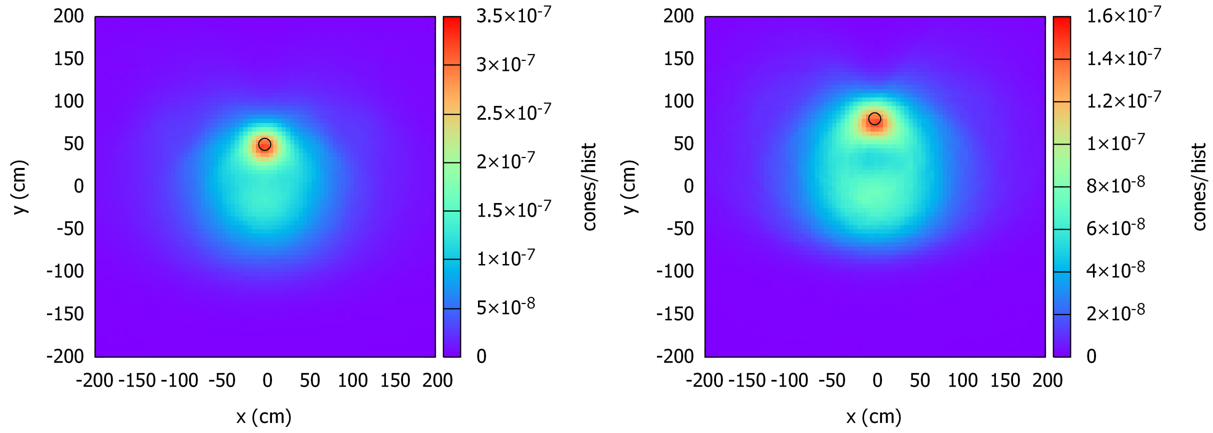

(a) $x = 0, y = 50$ cm (26.6°)

(b) $x = 0, y = 80$ cm (38.7°)

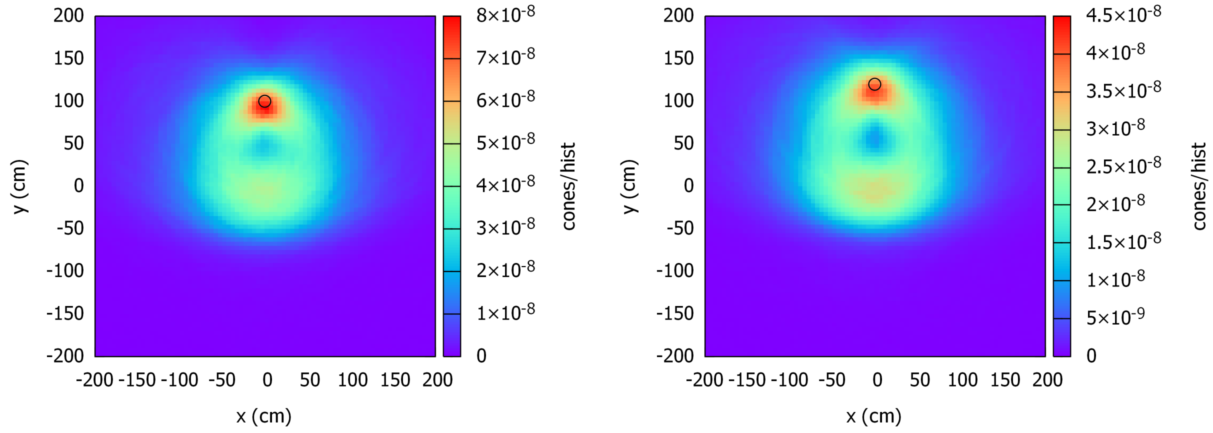

(c) $x = 0, y = 100$ cm (45°)

(d) $x = 0, y = 120$ cm (50.2°)

Figure 5.5: Reconstructed images for the simulated γ-rays of 662 keV. The source is placed at (a) $x = 0$, $y = 50$ cm (26.6°), (b) $x = 0$, $y = 80$ cm (38.7°), (c) $x = 0$, $y = 100$ cm (45°) and (d) $x = 0$, $y = 120$ cm (50.2°). The position of the sources is indicated by circles. Distance between the surface of the scatter layer and the source on the z-axis is 100 cm. The bar colour indicates the number of cones per number of histories or γ-rays emitted by the source that pass over a given pixel

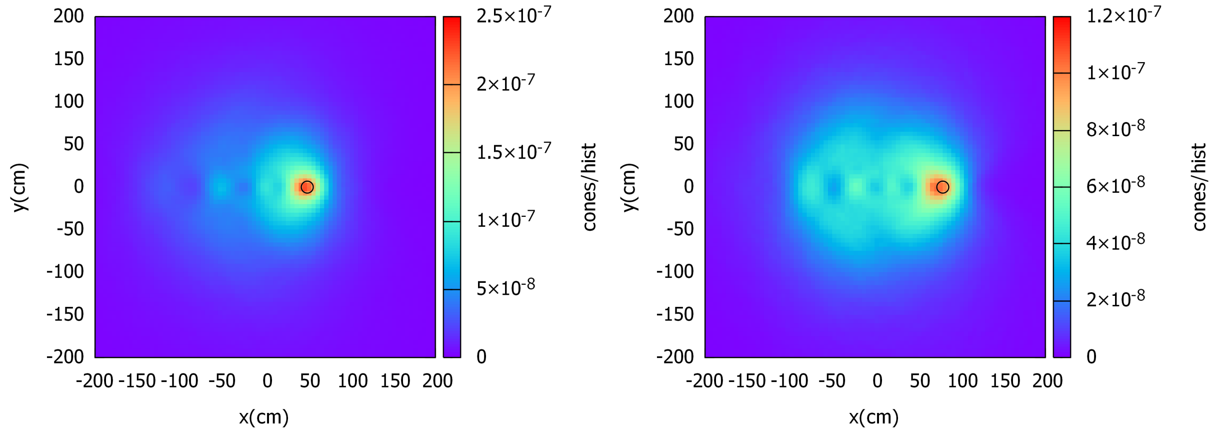

(a) $x = 50$ cm (26.6°), $y = 0$ (b) $x = 80$ cm (38.7°), $y = 0$

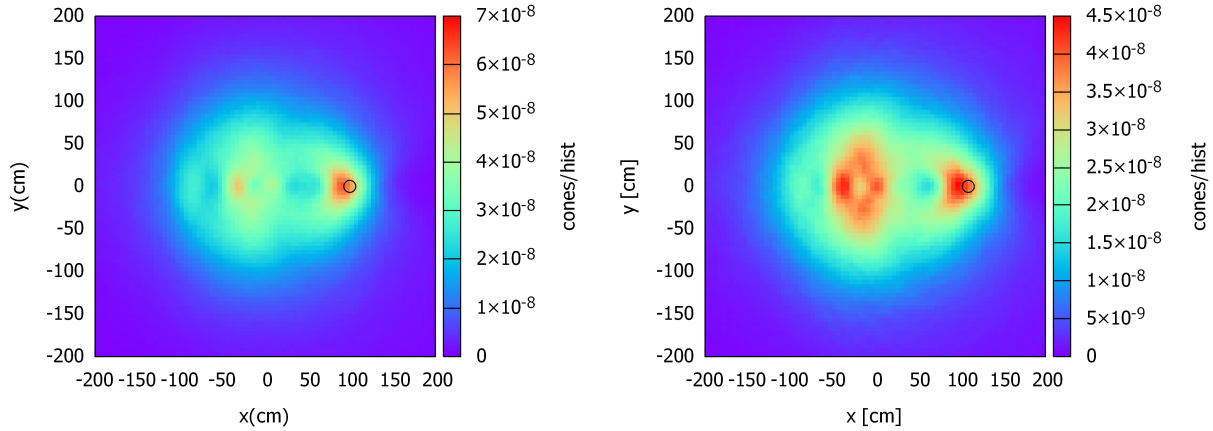

(c) $x = 100$ cm (45°), $y = 0$ (d) $x = 110$ cm (47.7°), $y = 0$

Figure 5.6: Reconstructed images for the simulated γ-rays of 1173 and 1332 keV. The source is placed at (a) $x = 50$ cm (26.6°), $y = 0$, (b) $x = 80$ cm (38.7°), $y = 0$, (c) $x = 100$ cm (45°), $y = 0$ and (d) $x = 110$ cm (47.7°), $y = 0$. The position of the sources is indicated by circles. Distance between the surface of the scatter layer and the source on the z-axis is 100 cm. The bar colour indicates the number of cones per number of histories or γ-rays emitted by the source that pass over a given pixel

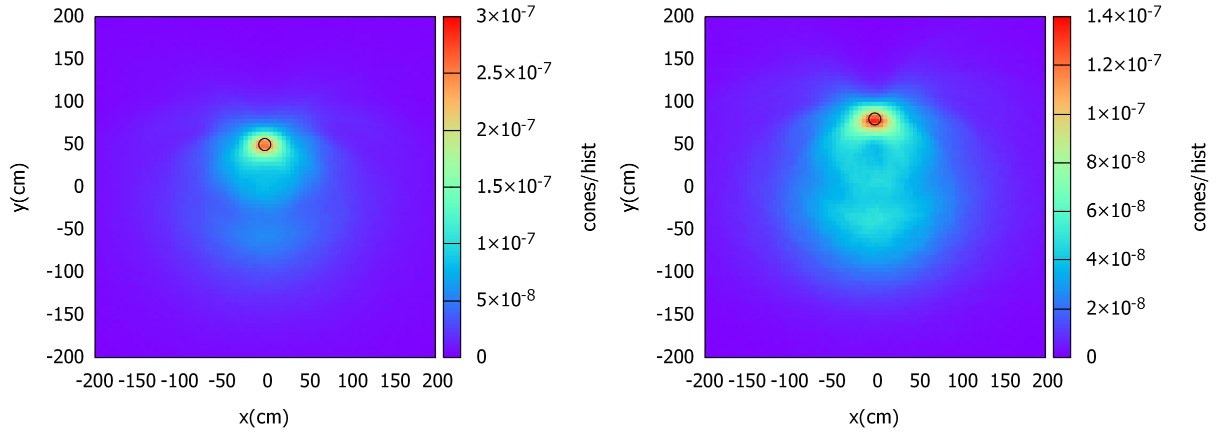

(a) $x = 0$, $y = 50$ cm (26.6°) (b) $x = 0$, $y = 80$ cm (38.7°)

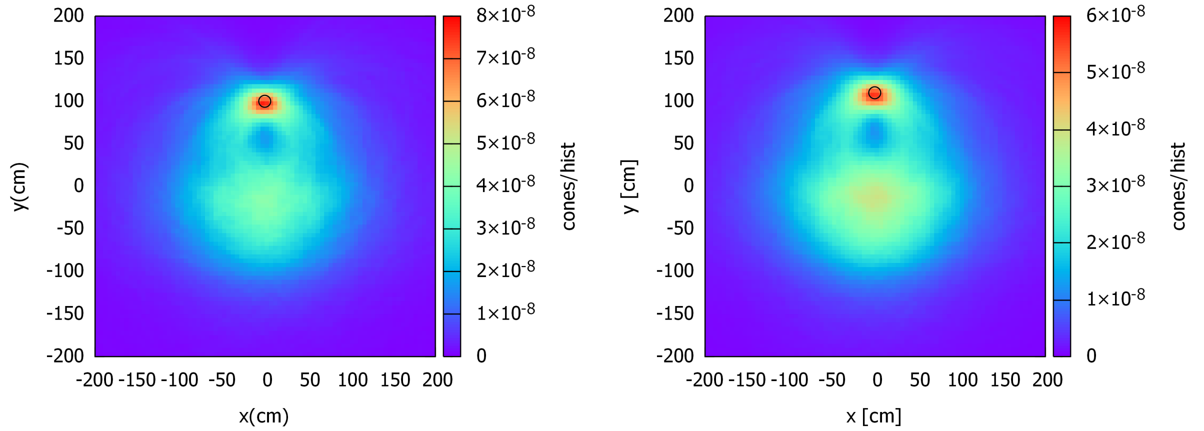

(c) $x = 0$, $y = 100$ cm (45°) (d) $x = 0$, $y = 110$ cm (47.7°)

Figure 5.7: Reconstructed images for the simulated γ-rays of 1173 and 1332 keV. The source is placed at (a) $x = 0$, $y = 50$ cm (26.6°), (b) $x = 0$, $y = 80$ cm (38.7°), (c) $x = 0$, $y = 100$ cm (45°) and (d) $x = 0$, $y = 110$ cm (47.7°). The position of the sources is indicated by circles. Distance between the surface of the scatter layer and the source on the z-axis is 100 cm. The bar colour indicates the number of cones per number of histories or γ-rays emitted by the source that pass over a given pixel

Table 5.2: Efficiency obtained when ^{131}I, ^{137}Cs and ^{60}Co sources are placed in the limit of the FOV. Distance between the scatter layer and sources on the z-axis is 100 cm

Source	Position	Efficiency (cones/hist)
^{131}I	$x = 170$ cm (59.5°), $y = 0$	$5.345 \cdot 10^{-7} \pm 1.7 \cdot 10^{-9}$
	$x = 0$, $y = 170$ cm (59.5°)	$4.543 \cdot 10^{-7} \pm 1.6 \cdot 10^{-9}$
^{137}Cs	$x = 100$ cm (45°), $y = 0$	$5.82 \cdot 10^{-7} \pm 2 \cdot 10^{-9}$
	$x = 0$, $y = 100$ cm (45°)	$5.14 \cdot 10^{-7} \pm 3 \cdot 10^{-9}$
^{60}Co	$x = 100$ cm (45°), $y = 0$	$5.51 \cdot 10^{-7} \pm 2 \cdot 10^{-9}$
	$x = 0$, $y = 100$ cm (45°)	$5.19 \cdot 10^{-7} \pm 3 \cdot 10^{-9}$

The main differences that are found between the images obtained for the simulated sources is the spreading of ellipses in the image. As was shown in Table 4.3, the angular resolution and image resolution are not as good for a source of 364 keV as for the other energies analysed. In addition, the allowed Compton scattering angles for sources of 364 keV are larger than for the other sources, as Table 5.1 shows. It is important to recall that the Compton scattering angle is the Compton cone opening angle. The intersection of Compton cones with the image plane thus gives larger ellipses when a source of ^{131}I is simulated. Therefore, images obtained with ^{137}Cs and ^{60}Co sources have less noise than those images obtained with ^{131}I sources.

Due to the overlapping of cones, there is a background in the images that is not related to the position of the source. When efficiency is low, this background becomes important compared with the area that indicates the position of the source. This produces areas with similar intensity, which can lead to misidentification of the position of the source. Efficiency should be high enough so that the background does not affect the results. Considering the images shown in Figs. 5.2, 5.3, 5.4, 5.5, 5.6 and 5.7, the FOV is around 60°, 45° and 45° for ^{131}I, ^{137}Cs and ^{60}Co sources, respectively. Table 5.2 shows the efficiencies that are obtained when sources are placed in the limit of the FOV.

5.2 Minimum number of cones

The minimum number of cones required to locate a source is approximately determined when the source can be clearly distinguished in the reconstructed image. ^{131}I, ^{137}Cs and ^{60}Co sources have been simulated. The distance between the surface of the scatter layer and the sources on the z-axis, h, was kept constant and equal to 100 cm. Images of reconstructed γ-rays are shown in Figs. 5.8, 5.9 and 5.10 when sources are placed at $x = 0$, $y = 0$; $x = 0$,

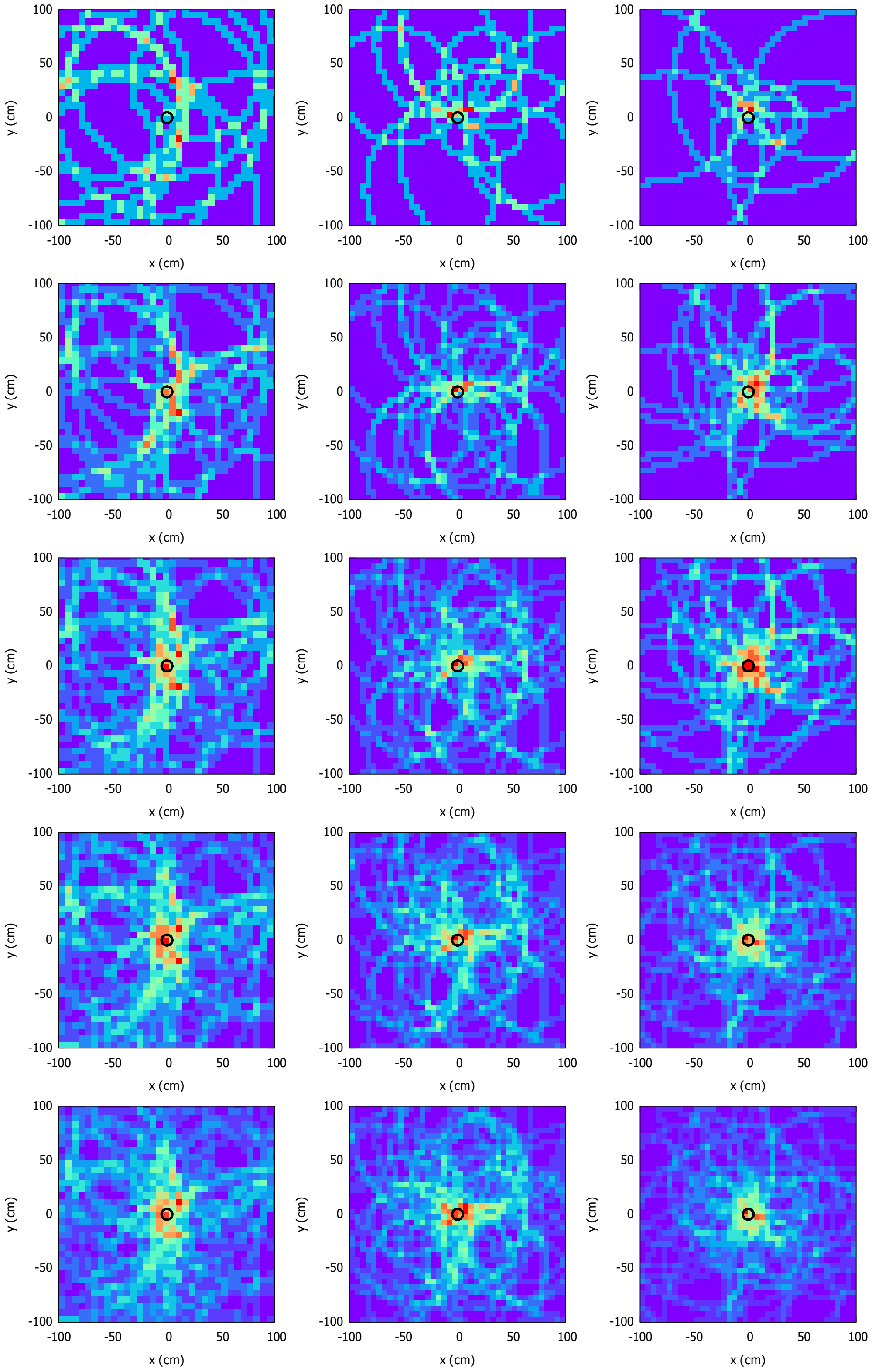

Figure 5.8: Back-projected images of ^{131}I (first column), ^{137}Cs (second column) and ^{60}Co (third column) sources, which were placed at $x = 0$, $y = 0$. Images were calculated using 10 (first row), 20 (second row), 30 (third row), 40 (fourth row) and 50 (fifth row) Compton cones. Distance between the surface of the scatter layer and the source on the z-axis is 100 cm. The pixel size was set to 3.6°, 3° and 2.6° on both axes for the sources of ^{131}I, ^{137}Cs and ^{60}Co, respectively.

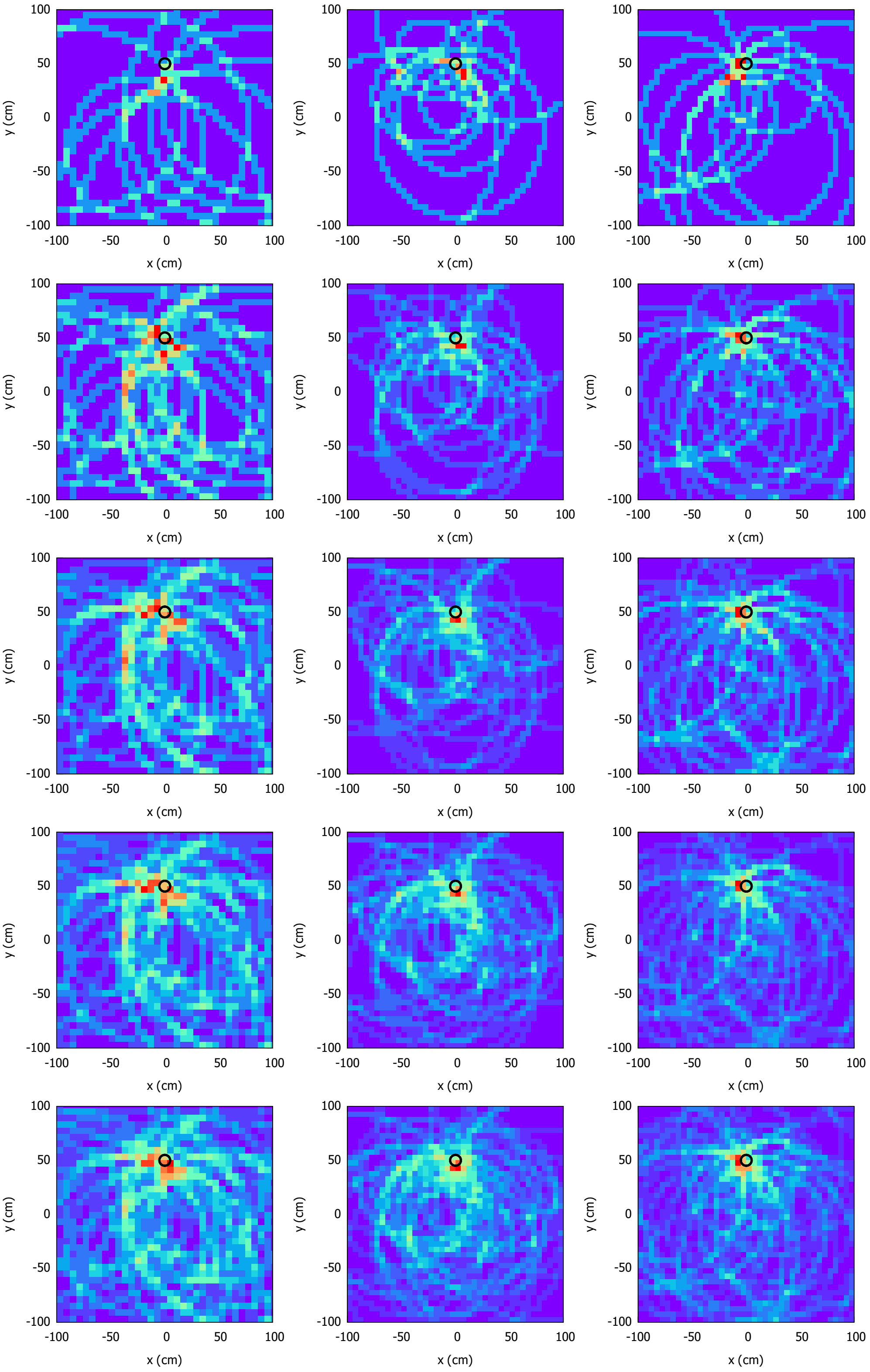

Figure 5.9: Back-projected images of ${}^{131}I$ (first column), ${}^{137}Cs$ (second column) and ${}^{60}Co$ (third column) sources, which were placed at $x = 0$, $y = 50$ cm (26.6°). Images were calculated using 10 (first row), 20 (second row), 30 (third row), 40 (fourth row) and 50 (fifth row) Compton cones. Distance between the surface of the scatter layer and the source on the z-axis is 100 cm. The pixel size was set to 3.6°, 3° and 2.6° on both axes for the sources of ${}^{131}I$, ${}^{137}Cs$ and ${}^{60}Co$, respectively.

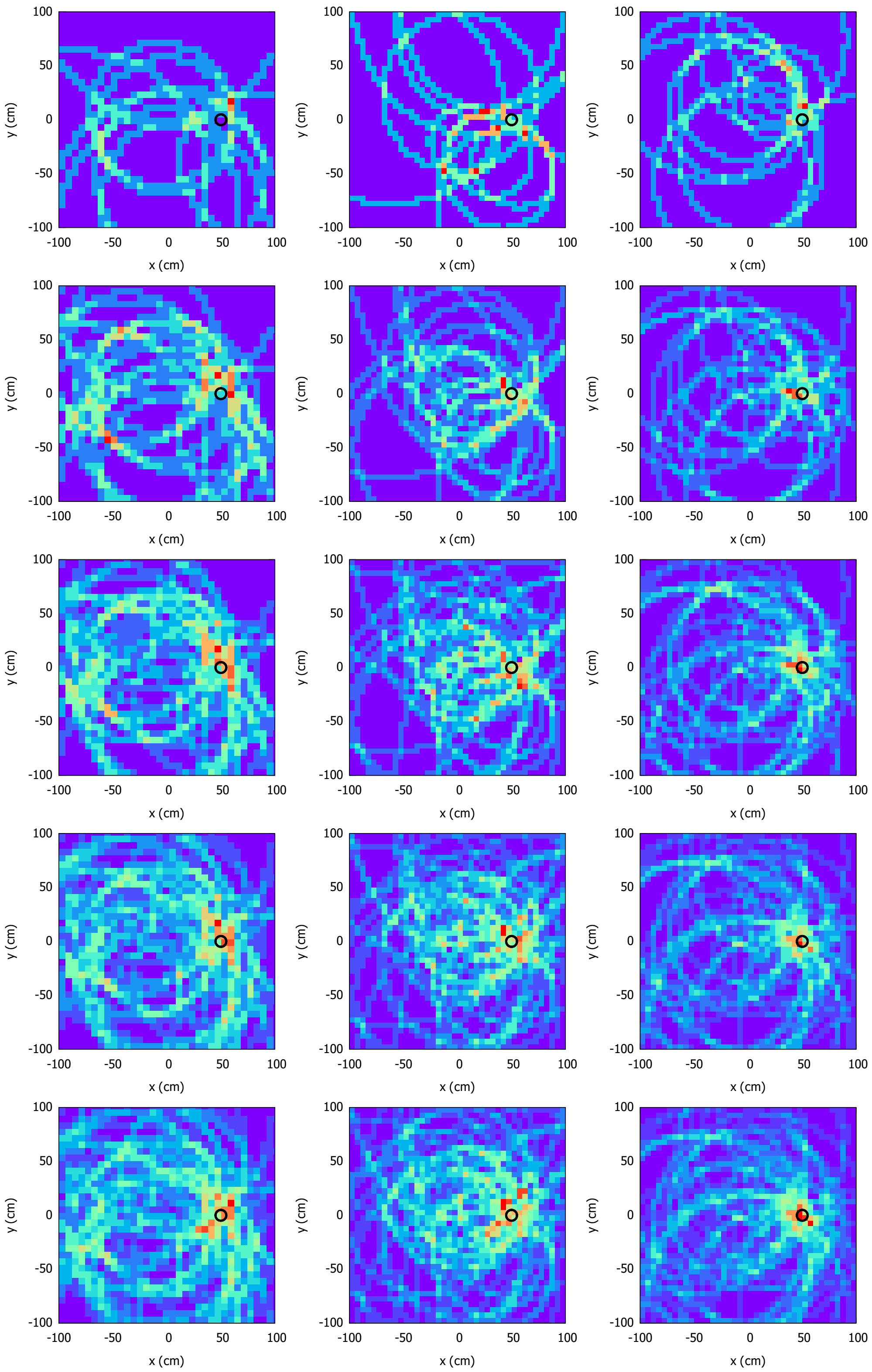

Figure 5.10: Back-projected images of ^{131}I (first column), ^{137}Cs (second column) and ^{60}Co (third column) sources, which were placed at $x = 50$ cm (26.6°), $y = 0$. Images were calculated using 10 (first row), 20 (second row), 30 (third row), 40 (fourth row) and 50 (fifth row) Compton cones. Distance between the surface of the scatter layer and the source on the z-axis is 100 cm. The pixel size was set to 3.6°, 3° and 2.6° on both axes for the sources of ^{131}I, ^{137}Cs and ^{60}Co, respectively.

$y = 50$ cm (26.6°) and $x = 50$ cm (26.6°), $y = 0$, respectively. Images of ^{131}I, ^{137}Cs and ^{60}Co sources are shown in the first, second and third column, respectively. Figs. 5.8, 5.9 and 5.10 have 5 rows of images. The difference between images from different rows are the number of cones used to calculate the image. The number of cones is 10, 20, 30, 40 and 50 from the top to the bottom.

The minimum number of cones depends on the size of the pixel. The larger the pixel size, the fewer cones are needed to determine the position of the source. However, the image resolution worsens when increasing the pixel size. In addition, the computational time needed to build an image using the back-projection algorithm depends on the number of intersections between the ellipses and the lines that limit the pixels. In order to have a reference, the size of the pixel was defined according to σ_{ARM}, which is the standard deviation of the ARM distribution ($FWHM_{ARM} = 2.35\sigma_{ARM}$). The ARM distribution indicates the distances between the ellipse and the source position. If we consider image resolution and the time needed to calculate the image, the pixel size was defined as $\sigma_{ARM}/2$. The angular resolution, $FWHM_{ARM}$, of the Compton camera is shown in Table 4.3 from Section 4.3. An angular resolution of $17.1° \pm 1.1°$, $13.63° \pm 0.12°$, $12.01° \pm 0.13°$ and $11.25° \pm 0.13°$ was found for energies of 364 keV, 662 keV, 1173 keV and 1332 keV, respectively. The pixel size was then set to 3.6°, 3° and 2.6° on both axes for the ^{131}I, ^{137}Cs and ^{60}Co sources, respectively.

As we can see in Figs. 5.8, 5.9 and 5.10, the minimum number of cones needed to locate a source is around 50 cones. The position of ^{131}I, ^{137}Cs and ^{60}Co sources placed at the centre can be determined by using 40, 30 and 30 cones, respectively. When sources are placed at $x = 0, y = 50$ cm (26.6°), around 40, 40 and 30 cones would be needed to locate ^{131}I, ^{137}Cs and ^{60}Co sources, respectively, while when sources are placed at $x = 50$ cm (26.6°),$y = 0$, the number of cones needed are around 50, 50 and 30 for ^{131}I, ^{137}Cs and ^{60}Co sources. Therefore, the minimum number of cones will be set to 50. It is important to point out that the minimum number of cones will be appropriate for a pixel size of $\sigma_{ARM}/2$.

Table 5.3: Minimum time needed to locate a ^{137}Cs source with an activity of 299MBq placed at the centre at distances of 5 m and 10 m from the Compton camera.

Distance h (m)	Efficiency (cones/hist)	Minimum time (s)
5	$1.0150 \cdot 10^{-7} \pm 1.8 \cdot 10^{-10}$	1.9
10	$2.422 \cdot 10^{-8} \pm 1.2 \cdot 10^{-10}$	8.1

5.3 Variation of efficiency, angular resolution and image resolution with Compton camera distance to the source

Efficiencies, angular resolution and image resolution were calculated for different Compton camera distances between the surface of the scatter detectors and sources, h. ^{131}I, ^{137}Cs and ^{60}Co sources were placed at $(x = 0, y = 0)$ in all the simulations.

Fig. 5.11 shows the efficiencies calculated for different distances h. As sources are moved away, the efficiency decreases approximately with $1/h^2$. Knowing the efficiencies, the minimum time needed to locate a source can be calculated with Eq. 5.1 when the number of cones is equal to the minimum number of required cones, which was set to 50 in Section 5.2.

$$cones = Eff\left[\frac{cones}{hist}\right] A t I_\gamma \geq Minimum\, number\, of\, cones \tag{5.1}$$

The parameter Eff is the efficiency with units of cones/history, where histories are the number of γ-rays emitted by the source. A is the activity of the source in Bq, t is the acquisition time in seconds and I_γ is the intensity of the γ-ray emission.

The ^{137}Cs source used in the experimental measurements in Section 2.4.2 can provide an example. Its activity was 299 MBq on 03/03/2020. The minimum time needed to locate this source when it was placed both at the centre and 5 and 10 metres away from the scatter layer is 1.9 and 8.1 seconds, as shown Table 5.3. The reconstructed images when this source is placed 5 and 10 metres away are shown in Fig 5.12. The number of γ-rays simulated are equivalent to the γ-rays emitted by the ^{137}Cs source with an activity of 299 MBq for the time shown in Table 5.3.

Angular resolution and image resolution were also calculated when the ^{131}I, ^{137}Cs and ^{60}Co sources were simulated at the centre at different distances from the Compton camera. Fig. 5.13a shows the angular resolution, while Fig. 5.13b shows the image resolution on both axes. Angular resolution improves a little between 1 and 2 metres, while it is constant for

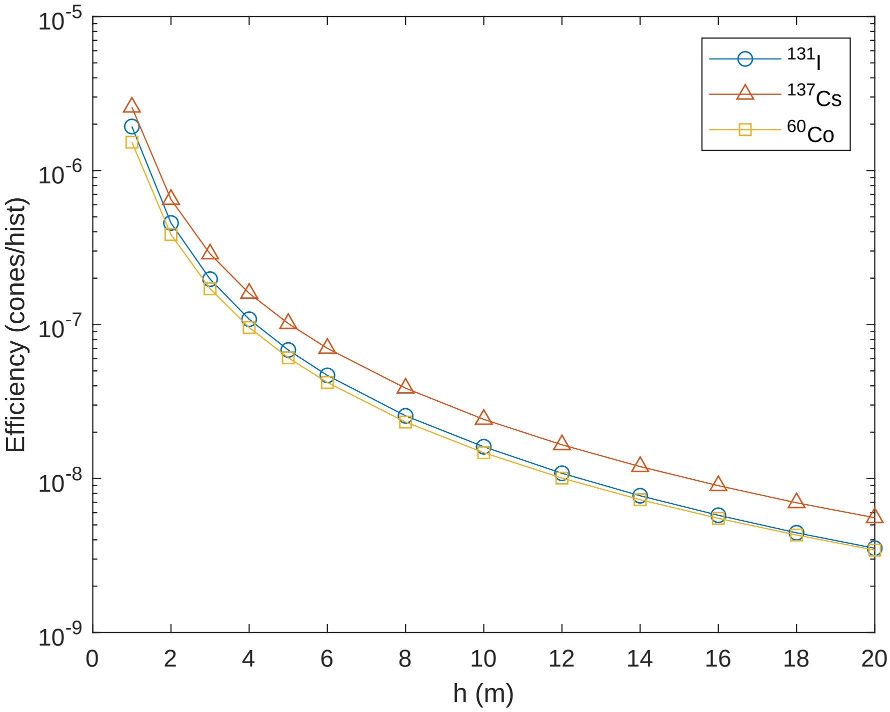

Figure 5.11: Compton camera efficiency when ^{131}I, ^{137}Cs and ^{60}Co sources were placed at different distances h from the Compton camera. Sources were placed at the centre and moved along the z-axis.

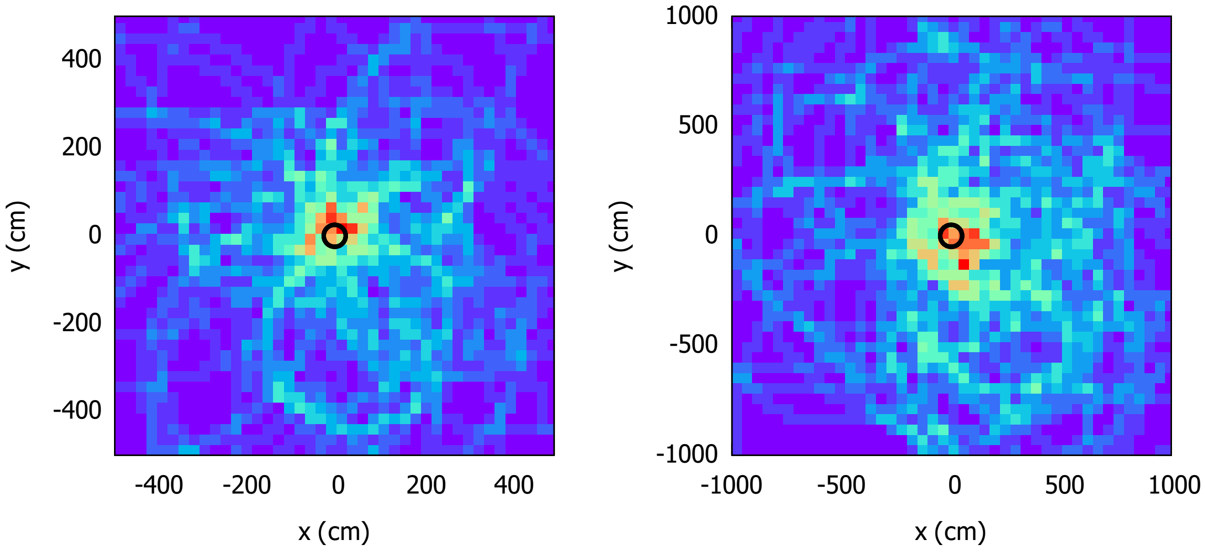

(a) $h = 5$ m

(b) $h = 10$ m

Figure 5.12: Back-projected images obtained for a ^{137}Cs source placed at (a) 5 m and (b) 10 m. The number of γ-rays simulated were calculated for a 299 MBq source with a time of exposition equal to the minimum time shown in Table 5.3. The source was placed at $(x = 0, y = 0)$. The pixel size was selected according to $\sigma_{ARM}/2$.

Table 5.4: Angular resolution ($FWHM_{ARM}$) and image resolution on both axes ($FWHM_x$ and $FWHM_y$) when ^{131}I, ^{137}Cs and ^{60}Co sources were placed at the centre at a distance of 2 metres from the Compton camera

Source	$FWHM_{ARM}$ (deg)	$FWHM_x$ (deg)	$FWHM_y$ (deg)
^{131}I	15.8 ± 1.1	21.2 ± 0.4	26.7 ± 0.7
^{137}Cs	13.17 ± 0.13	17.2 ± 0.2	18.1 ± 0.3
^{60}Co	11.40 ± 0.12	18.97 ± 0.12	15.8 ± 0.6

the other distances. Image resolution can be considered constant with distance h. Table 5.4 shows the angular resolution and image resolution of the Compton camera when ^{131}I, ^{137}Cs and ^{60}Co sources are placed at 2 metres from the scatter layer. The angular resolution is found to be between 11° and 16° degrees, depending on the energy. Image resolution is found to be between 17° and 21° on the x axis, while on the y axis it is found to be between 15° and 27°, depending on the energy.

The Compton camera design in this thesis has been compared with the Compton camera based on Ce:GAGG scintillator arrays and multi-pixel photon counter arrays described in the introduction chapter (Kataoka et al., 2013; Kishimoto et al., 2014). Each pixel of this Compton camera has a size of $1.5 \times 1.5 \times 5$ mm^3. The array configuration of each layer is 4 blocks of 15×15 pixels. The distance between layers is 16 mm. The Compton camera has a small size and a weight of 1.9 kg. The angular resolution achieved is 14° ($FWHM$) for gamma-rays of 662 keV. Its FOV is 180°. The authors were able to detect a point source with activity of 10 MBq at a distance of 50 cm (~ 5 μSv/h) with an acquisition time of 30 s.

The angular resolution achieved with the Compton camera designed in this thesis for a source of 662 keV placed at the centre and 50 cm away is $14.58° \pm 0.13°$ ($FWHM$). Furthermore, it is expected that this Compton camera can locate a ^{137}Cs source with an activity of 10 MBq at 50 cm in a short period of time. The efficiency when a source of ^{137}Cs is placed 50 cm away is $9.904 \cdot 10^{-6}$ cones/hist. Using Eq. 5.1, the time needed to obtain 50 cones is less than 1 s. Therefore, it seems that the Compton camera design here has a better efficiency than that designed in Kishimoto et al. (2014). This is due to the fact that the size of detectors that are used to build our Compton camera are larger. As regards the FOV of both cameras, the Compton camera designed in this thesis is lower than that developed in Kataoka et al. (2013). For instance, the FOV for a ^{137}Cs point source is 45° for the Compton camera in this thesis, while it is 180° for the pixelated camera.

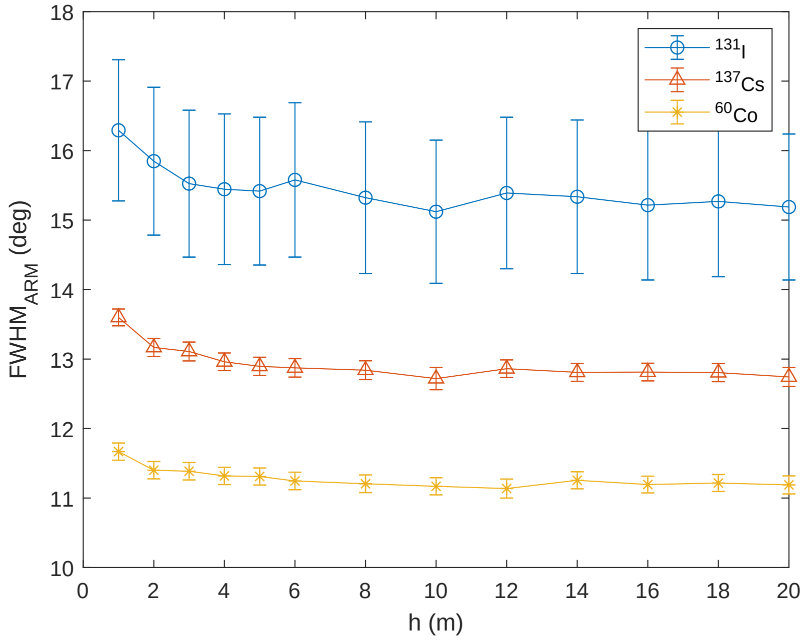

(a) Angular resolution

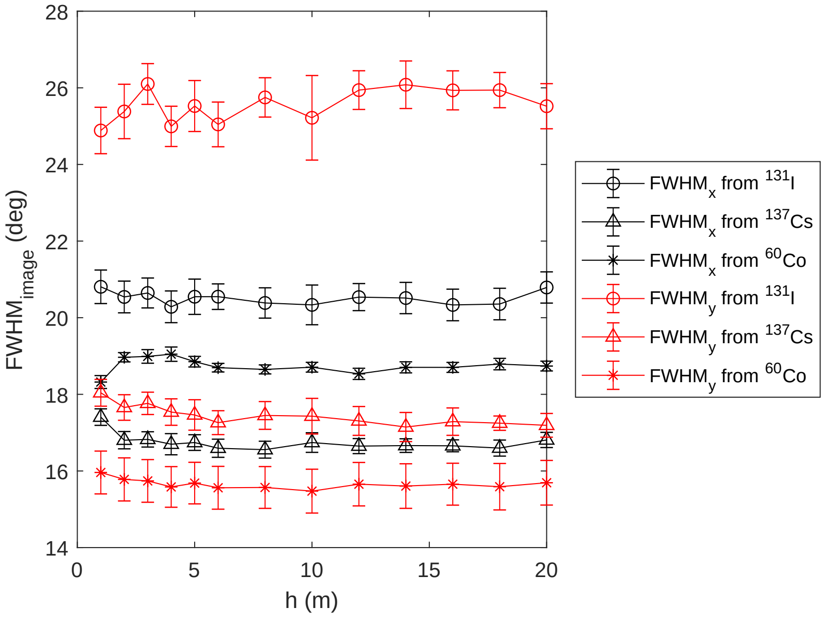

(b) Image resolution

Figure 5.13: Angular resolution and image resolution for different distances between the surface of the scatter layer and sources, h. ^{131}I, ^{137}Cs and ^{60}Co sources were placed at $(x = 0, y = 0)$

5.4 Ability of the Compton camera to detect several sources in the environment

The ability of the Compton camera to detect several sources in the environment using the back-projection method has been evaluated. To this end, two kinds of sources were simulated: point sources and surface sources. In both cases, ^{131}I, ^{137}Cs and ^{60}Co sources were simulated in order to analyse the effects of energy on the ability of the Compton camera.

5.4.1 Point sources

Firstly, simulations with several point sources were carried out in order to determine if the Compton camera is able to locate several sources simultaneously using the back-projection method. Fig. 5.14 shows the images obtained when two-, three- and four-point sources of ^{131}I (first column), ^{137}Cs (second column) and ^{60}Co (third column) were simulated. The first row of Fig. 5.14 shows images when two sources are placed at $x = 200$ cm (21.8°), $y = 0$ and $x = -200$ cm (−21.8°), $y = 0$. The images of three-point sources placed at $x = 200$ cm (21.8°), $y = 0$; $x = -200$ cm (−21.8°), $y = 0$ and $x = 0$, $y = 200$ cm (21.8°) are shown in the second row. The third row shows the images obtained when four sources are simulated, which were placed at $x = 0$, $y = 200$ cm (21.8°); $x = 0$, $y = -200$ cm (−21.8°); $x = 200$ cm (21.8°), $y = 0$ and $x = -200$ cm (−21.8°), $y = 0$. The positions of the point sources are marked with circles in the images. The distance between the surface of the scatter detectors and sources on the z-axis, h, is 500 cm. These images were calculated over a long period of time in order to have good statistics.

As we can see in Fig. 5.14, the Compton camera is able to locate two-point sources of ^{131}I, ^{137}Cs and ^{60}Co. When three-point sources are simulated, the Compton camera is not able to distinguish the three sources of ^{131}I, while it is able to locate the three sources of ^{137}Cs and ^{60}Co. This is mainly due to the fact that ^{131}I images have poor resolution compared to ^{137}Cs and ^{60}Co. In the last row of images in Fig. 5.14, we can see that four sources can only be perfectly distinguished for simulated sources of ^{60}Co.

Images obtained with the back-projection method are usually noisy due to overlapping of cones. This causes limitations in locating several sources. Results might be improved by using other reconstruction methods, such as the filtered back-projection method (Xu et al., 2004; Kagaya et al., 2015).

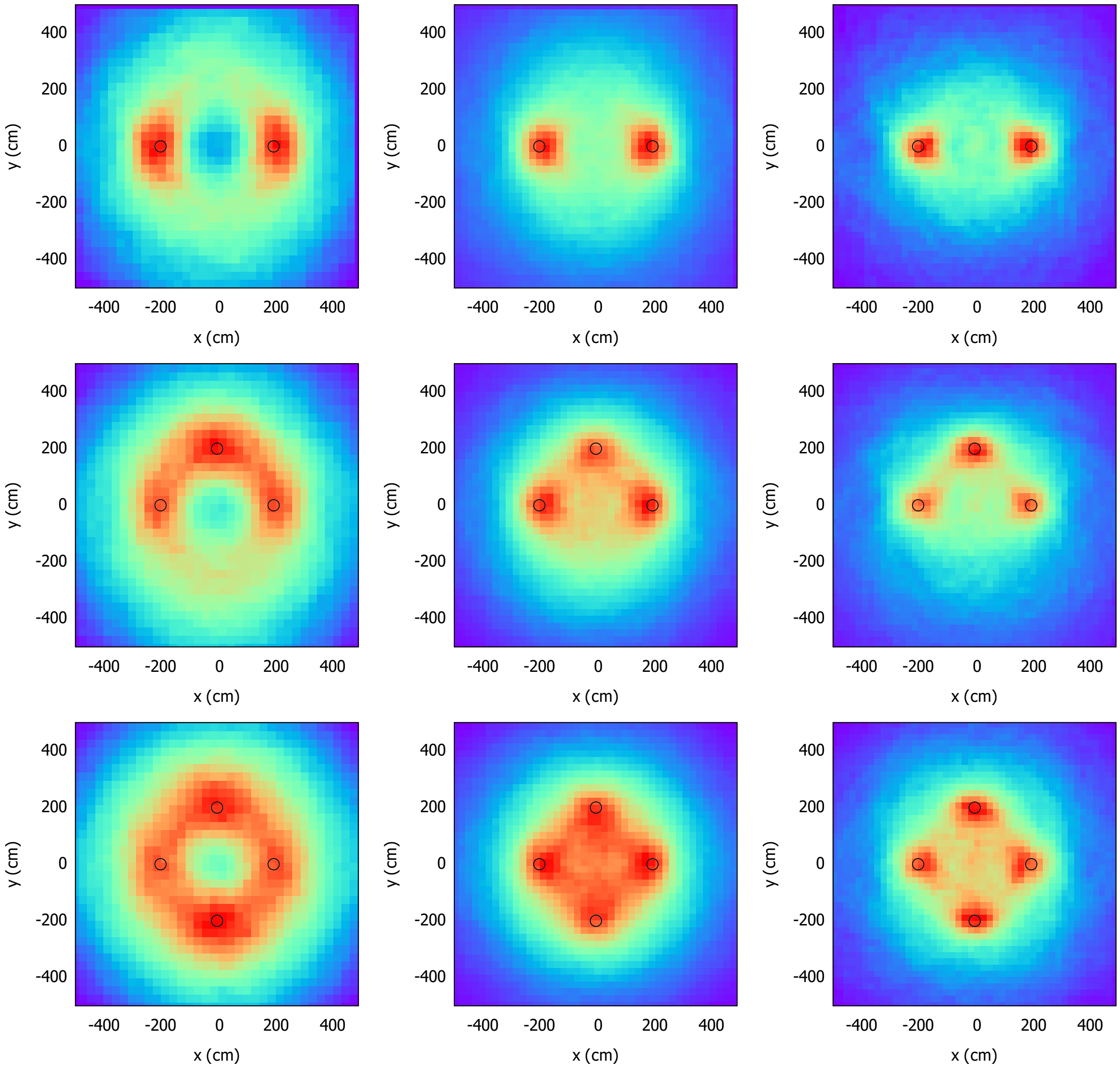

Figure 5.14: Back-projected images of point sources of ^{131}I (first column), ^{137}Cs (second column) and ^{60}Co (third column). Images from the simulations of two-, three- and four-point sources are shown in the first, second and third rows, respectively. The position of the sources is indicated with circles. The distance between the surface of the scatter layer and sources on the z-axis is 500 cm

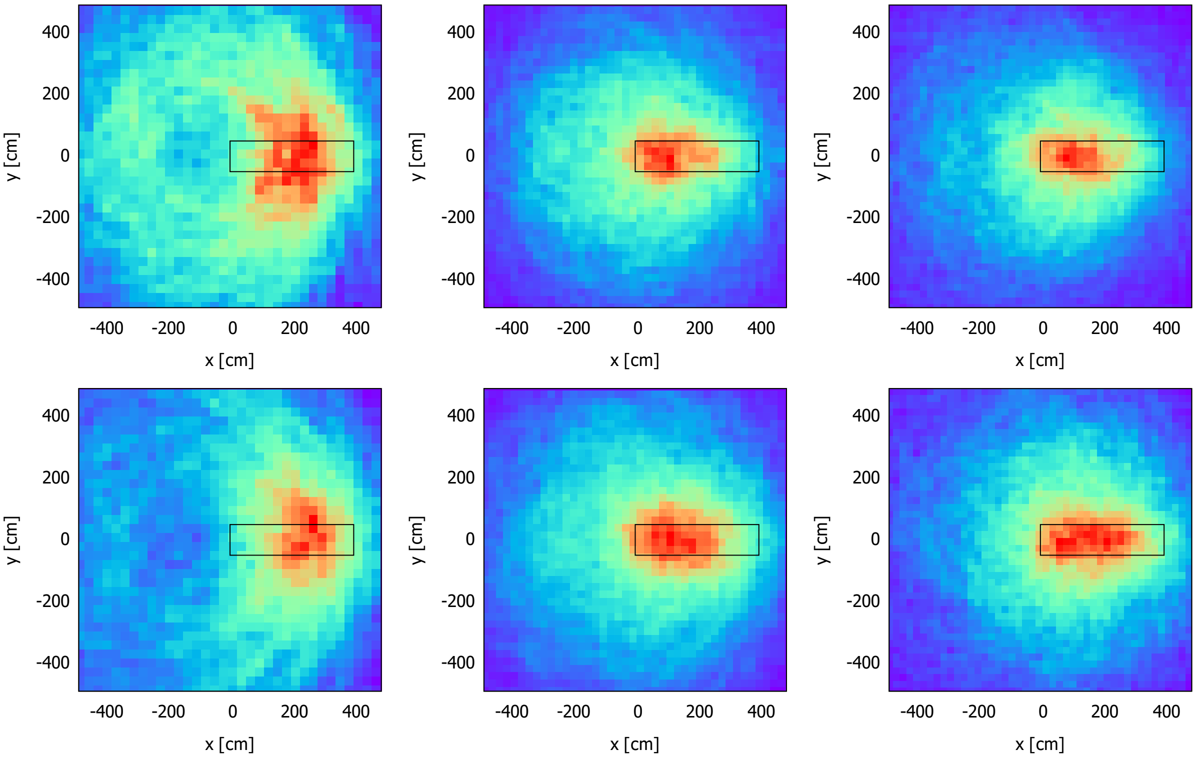

Figure 5.15: Back-projected images of a surface source of size 400 × 100 cm^2 centred at ($x = 200, y = 0$) cm. This surface emits γ-rays from sources of ^{131}I (first column), ^{137}Cs (second column) and ^{60}Co (third column). The distance between the scatter layer and sources is 500 cm in the first row and 700 cm in the second row. Sources are represented by black rectangles

5.4.2 Surface sources

In order to determine the ability of the Compton camera to determine deposition of radioactive material over a large area, a simulation of surface sources was done. Three kinds of contaminated areas were simulated: i) an area of 400 × 100 cm^2 centred at ($x = 200, y = 0$) cm (see Fig. 5.15), ii) an area of 100 × 400 cm2 centred at ($x = 0, y = 200$) cm (see Fig. 5.16), and iii) two radioactive areas of 400×100 cm^2 and 100×400 cm^2 centred at ($x = 200, y = 0$) cm and ($x = 0, y = 200$) cm, respectively (see Fig. 5.17). Figs. 5.15, 5.16 and 5.17 show the images calculated when these contaminated areas emit γ-rays from sources of ^{131}I (first column), ^{137}Cs (second column) and ^{60}Co (third column). These figures have two rows of images. The distance between the surface of the scatter layer and sources was set to 500 cm in the first row and 700 cm in the second row.

In Figs. 5.15, 5.16 and 5.17 it can be seen that when the distance between the Compton camera and the sources is 700 cm, the images better represent the source than for the distance of 500 cm. However, images are not able to reproduce the entire source. As in Section 5.4.1, images of ^{131}I sources do not have as good a resolution as those images

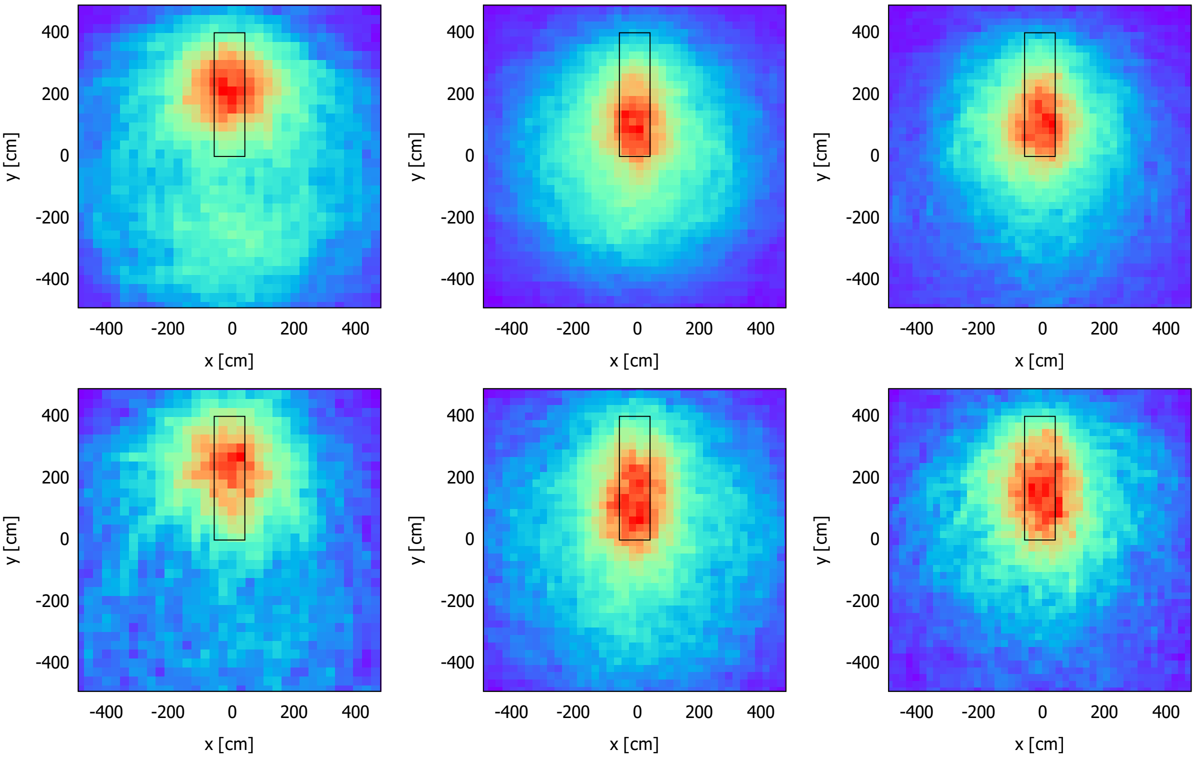

Figure 5.16: Back-projected images of a surface source of size 100 × 400 cm^2 centred at $(x = 0, y = 200)$ cm. This surface emits γ-rays from sources of ^{131}I (first column), ^{137}Cs (second column) and ^{60}Co (third column). The distance between the scatter layer and sources is 500 cm in the first row and 700 cm in the second row. Sources are represented by black rectangles

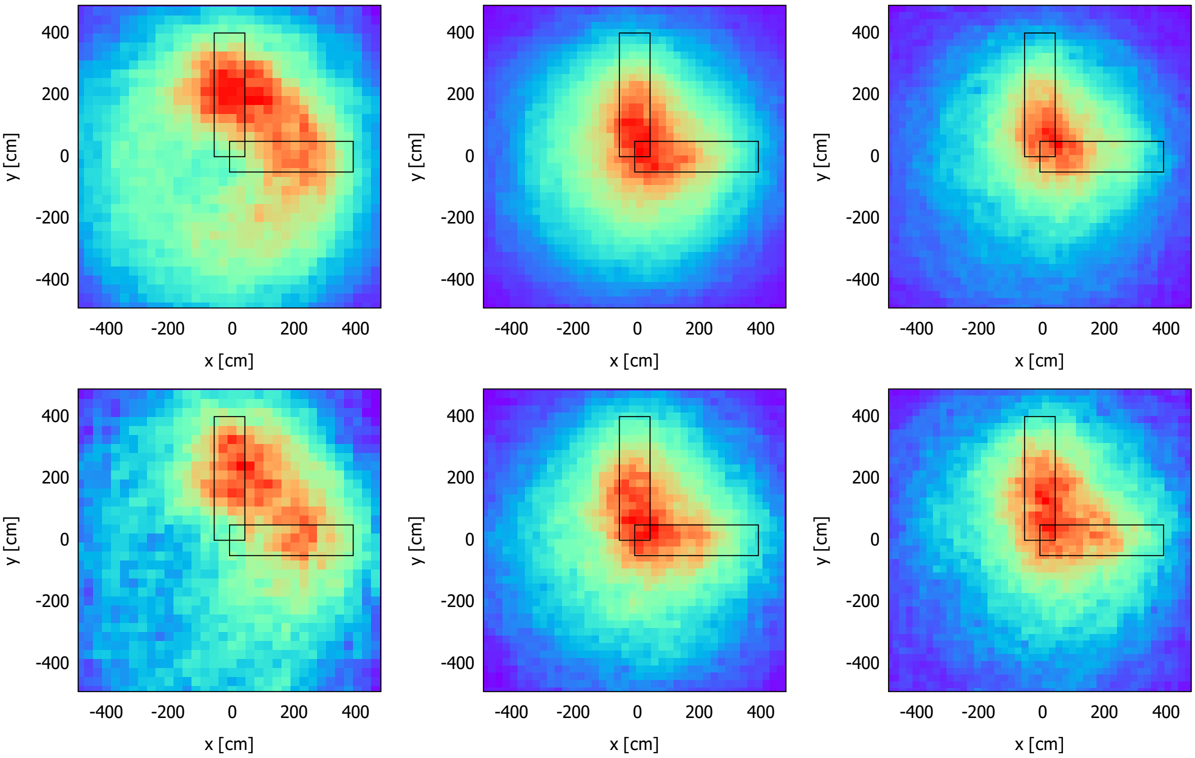

Figure 5.17: Back-projected images of two surface sources of size 400 × 100 cm^2 and 100 × 400 cm^2 centred at $(x = 200, y = 0)$ cm and $(x = 0, y = 200)$ cm, respectively. This surface emits γ-rays from sources of ^{131}I (first column), ^{137}Cs (second column) and ^{60}Co (third column) sources. The distance between the scatter layer and sources is 500 cm in the first row and 700 cm in the second row. Sources are represented by black rectangles

obtained with ^{137}Cs and ^{60}Co. This can be clearly seen in Fig. 5.17.

5.5 Conclusions

The characterization of the Compton camera designed in Chapter 4 consisting of eight scintillator bars of $2 \times 2 \times 10$ cm^3 was done using Monte Carlo simulations in this chapter. The FOV of the Compton camera was estimated for isotropic ^{131}I (364 keV), ^{137}Cs (662 keV) and ^{60}Co (1173 and 1332 keV) sources. Sources were moved in the plane $z = -100$ cm, which is parallel to the scatter layer. It was found that the FOV depends on the energy of the incident γ-rays. This is due to the energy windows defined for each energy. As regards the images calculated with the back-projection method, the FOV is approximately 60°, 45° and 45° on the x and y axes for ^{131}I, ^{137}Cs and ^{60}Co sources, respectively. In addition, it was found that images from ^{131}I sources are noisier than those obtained with ^{137}Cs and ^{60}Co sources.

The minimum number of cones required to locate ^{131}I, ^{137}Cs and ^{60}Co sources was estimated by calculating the images with an increasing number of cones. The minimum number of cones was selected at the point where the sources were distinguishable in the image. It was found that the number of cones should be approximately 50 cones in order to locate ^{131}I, ^{137}Cs and ^{60}Co sources using a pixel size of $\sigma_{ARM}/2$.

Efficiencies, angular resolution and image resolution were calculated for different distances between the surface of the scatter layer and sources on the z axis, h. As was expected, the Compton camera efficiency decreases approximately with $1/h^2$. Angular resolution is constant for distances h greater than 2 m and image resolution can be considered to be independent of the distance h. For distances of 2 metres, the angular resolution is found to be between 11° and 16° ($FWHM$), depending on the energy. Image resolution is found to be between 17° and 21° ($FWHM_x$) on the x axis, while on the y axis it is found to be between 17° and 27° ($FWHM_y$), depending on the energy.

The ability of the Compton camera to identify radioactive material in the environment using the back-projection method was evaluated by simulating several point and surface sources. The Compton camera was able to detect several sources simultaneously, but as the number of sources increases, the images become noisier. This makes identification of sources more difficult. As regards the surface sources, the Compton camera was not able to reproduce the entire contaminated areas. These results indicate that the back-projection method usually gives noisy images due to the overlapping of the cones, which limits the image resolution and, therefore, the identification of different sources. These results might be improved by using other reconstruction methods, such as the filtered back-projection method.

Chapter 6

Conclusions and future activities

The aim of the thesis was to design and characterise a Compton camera consisting of scintillator bars for subsequent mounting on a UAS so as to locate sources in the environment. The detectors used were long CsI(Tl) scintillator bars with two SiPMs placed at both ends of the bar. These detectors are both position and energy sensitive. It is expected that these kinds of detectors make the Compton camera robust enough so that it can be transported onto and around nuclear sites or mounted on a UAS. Another constraint is that the final Compton camera is affordable in order to meet the requirements of agencies with limited funds.

The design was done using PENELOPE/penEasy simulations. Firstly, the MC simulations were validated. To this end, two CsI(Tl) scintillator detectors were purchased from the Scionix company, which had previously treated the surfaces of the detectors in order to obtain an optimum position resolution. The validation of PENELOPE/penEasy Monte Carlo code was done by comparing experimental data with their equivalent simulated data. The validation consisted of i) validation of the geometry defined in MC simulations and ii) defining codes used to calculate the image for a Compton camera based on CsI(Tl) scintillator bars. This was done by comparing simulated data with experimental data obtained in two different experimental measurement campaigns. The first campaign corresponded to the irradiation of detectors with a collimated source of ^{137}Cs, while the second campaign consisted of irradiating a simple Compton camera consisting of two CsI(Tl) scintillator bars at a reference calibration laboratory (LCD) of the Institute of Energy Technologies (INTE) of the Technical University of Catalonia (UPC).

The first campaign was also used to characterise the detectors. The characterization of the bars consisted of determining the attenuation coefficient, as well as the energy and position resolution. The detectors acquired have attenuation coefficients of 0.056 ± 0.0015 cm^{-1} and 0.091 ± 0.0011 cm^{-1}. The difference between them might indicate that one of the detectors had suffered a change of the surface reflectivity or the optical transmission from the crystal to the SiPMs was not the same for both detectors. Energy resolution and position resolution were found to be almost independent of the position of gamma-ray interactions for a collimated ^{137}Cs source. Energy resolutions of the detectors were $7.6 \pm 0.2\%$ ($FWHM$) and $7.74 \pm 0.10\%$ ($FWHM$). Position resolutions of the detectors were 0.409 ± 0.007 cm (σ_y) and 0.291 ± 0.009 cm (σ_y). The difference between the position resolutions is a consequence of having different attenuation coefficients. The detector with a lower attenuation coefficient is not desirable for a Compton camera because it will introduce higher errors in the determination of the position of γ-ray interactions in the detector.

In order to carry out the validation, MC simulations equivalent to the experimental measurements were done. The validation consisted of comparing the main experimental and simulated results. The response of each individual detector, the Compton camera efficiency, the angular resolution and quality of images were compared. Images were obtained with the simple back-projection method. Results show good agreement between both experimental and simulated data.

It is important to point out that experimental images are not affected by the background. This is mainly due to the selection of events according to deposited energy, which reduces noisy events arising from the background or an initial scattered γ-ray.

Once simulations were fully validated, the design of a Compton camera consisting of two layers of CsI(Tl) scintillator bars was done. The cross-section size of crystals and distance between layers were optimized based on Compton camera efficiency, as well as angular resolution and image resolution. This study was done by simulating energies in a wide range: 364 keV (^{131}I), 662 keV (^{137}Cs), 1173 keV (^{60}Co) and 1332 keV (^{60}Co). The final optimized Compton camera consists of two layers separated by 10 cm. Each layer has 4 CsI(Tl) scintillator bars of $2 \times 2 \times 10$ cm^3.

The characterization of the optimized Compton camera was done by simulating the main γ-ray lines of ^{131}I, ^{137}Cs and ^{60}Co sources. The characterization consisted of determining the Compton camera FOV, the approximate number of Compton cones needed to locate a source, efficiency, angular resolution and image resolution.

The FOV depends on the deposited energy in the scatter layer, which determines the scattering angle of the γ-ray. The deposited energies allowed in the scatter layer were set to $E < 125$ keV; $E < 150$ keV; $E < 170$ keV and $260 < E < 490$ keV; and $E < 170$ keV and $280 < E < 600$ keV for γ-rays of 364 keV, 662 keV, 1173 keV and 1332 keV, respectively. This means that the Compton scattering angles are limited to $\theta_c < 75°$; $\theta_c < 39°$; $\theta_c < 22°$, $29° < \theta_c < 47°$; and $\theta_c < 19°$, $26° < \theta_c < 47°$ for gamma-ray energies of 364 keV, 662 keV, 1173 keV and 1332 keV, respectively. Images of the three sources were calculated and the FOV was found to be approximately 60°, 45° and 45° for ^{131}I, ^{137}Cs and ^{60}Co sources, respectively. This FOV is similar on both x and y axes.

The minimum number of cones required to locate ^{131}I, ^{137}Cs and ^{60}Co sources was estimated by calculating the images with an increasing number of cones. The minimum number of cones was selected at the point where the sources were distinguishable in the image. It was found that the number of cones should be around 50 cones in order to locate ^{131}I, ^{137}Cs and ^{60}Co sources.

Efficiencies, angular resolution and image resolution were calculated for different distances between the Compton camera and sources. For example, when this distance is 2 metres the angular resolution is found to be between 11° and 16° ($FWHM$), depending on the energy. Image resolution is found to be between 17° and 21° ($FWHM_x$) on the x axis, while on the y axis it is found to be between 16° and 27° ($FWHM_y$), depending on the energy. Efficiencies are $4.563 \cdot 10^{-7} \pm 0.009 \cdot 10^{-7}$ cones/history, $6.490 \cdot 10^{-7} \pm 0.011 \cdot 10^{-7}$ cones/history and $3.841 \cdot 10^{-7} \pm 0.007 \cdot 10^{-7}$ cones/history for ^{131}I, ^{137}Cs and ^{60}Co sources, respectively.

The ability of the Compton camera to identify radioactive material in the environment using the back-projection method was evaluated by simulating several point and surface sources. The Compton camera was able to detect several point sources simultaneously, but as the number of sources increases, images become noisier. As regards the surface sources, the Compton camera was not able to reproduce the entire contaminated areas for any of the energies tested.

6.1 Future activities

According to the promising results obtained in the design of a Compton Camera for mounting on a UAS, future activities to test the camera in real situations would be:

- Construction of the designed Compton Camera in a specific mechanical structure for mounting on a UAS.

- Optimization of the digital electronics for signal detection so that it has minimum size and weight.

- Improvement of the image software in order to obtain images in real time to facilitate the tasks of the radiological analyst.

- The images calculated in this thesis for several point and surface sources indicate that the back-projection method usually gives noisy images. Other reconstruction methods, such as the filtered back-projection method, should be tested in order to study the influence of the reconstruction method on image quality.

- Pile-up and dead time should be studied in case high activities are found in the environment.

- The possibility of using the individual pulse height spectra of the detectors and the sum of all the spectra to locate where the highest gamma-ray fluence arises and to identify the sources should be looked into. This could provide preliminary information on where to hover the UAS to obtain optimum radiological images.

- Finally, the detection system should be tested under laboratory conditions and under real conditions at an aerial site. Artificial sources or enhanced natural radionuclides, such as former uranium mines, might be used.

Bibliography

Agramunt, J., Tain, J. L., Albiol, F., Algora, A., Estevez, E., Giubrone, G., Jordan, M. D., Molina, F., Rubio, B., and Valencia, E. (2013). A triggerless digital data acquisition system for nuclear decay experiments. In *La Rabida 2012 International Scientific Meeting on Nuclear Physics*, pages 165–166.

Agramunt, J., Tain, J. L., Gómez-Hornillos, M. B., Garcia, A. R., Albiol, F., Algora, A., Caballero-Folch, R., Calviño, F., Cano-Ott, D., Cortés, G., Domingo-Pardo, C., Eronen, T., Gelletly, W., Gorelov, D., Gorlychev, V., Hakala, H., Jokinen, A., Jordan, M. D., Kankainen, A., Kolhinen, V., Kucuk, L., Martinez, T., Mason, P. J. R., Moore, I., Penttila, H., Podolyák, Z., Pretel, C., Reponen, M., Riego, A., Rissanen, J., Rubio, B., Saastamoinen, A., Tarifeño-Saldivia, A., and Valencia, E. (2016). Characterization of a neutron–beta counting system with beta-delayed neutron emitters. *Nuclear Instruments and Methods in Physics Research Section A: Accelerators, Spectrometers, Detectors and Associated Equipment*, 807:69–78.

Askari, M., Taheri, A., Mojtahedzadeh larijani, M., and Movafeghi, A. (2019). Industrial gamma computed tomography using high aspect ratio scintillator detectors (A Geant4 simulation). *Nuclear Instruments and Methods in Physics Research, Section A: Accelerators, Spectrometers, Detectors and Associated Equipment*, 923:109–117.

Bassalleck, B., Hasinoff, M. D., and Salomon, M. (1979). Test results from a position-sensitive NaI detector. *Nuclear Instruments and Methods*, 163(2-3):389–393.

Boyle, P. J., Hanna, D. S., MacLeod, A. M. L., Sinclair, L. E., Seywerd, H. C. J., and Saull, P. R. B. (2011). Optimization of pulse-height sharing for use below 150 keV in long bars of NaI(Tl). *2011 IEEE Nuclear Science Symposium Conference Record*, pages 440–443.

Carter, J. N., Charalambous, P., Dean, A. J., Stephen, J. B., Butler, R. C., Di Cocco, G., Morelli, E., Spada, G., Spizzichino, A., Barbareschi, L., Boella, G., Perotti, F., Villa, G., Badiali, M., La Padula, C., Polcaro, F., and Ubertini, P. (1982). A position sensitive detector for a gamma-ray imaging telescope. *Nuclear Instruments and Methods*, 196(2-3):477–482.

Charalambous, P. M., Dean, A. J., Drane, M., Gil, A., Stephen, J. B., Young, N. G. S., Butler, R. C., Caroli, E., Di Cocco, G., Spada, G., Spizzichino, A., Barbareschi, L., Perotti, F., Villa, G., Badiali, M., La Padula, C., Polcaro, F., and Ubertini, P. (1984). A two-dimensional low energy gamma-ray position sensitive detector. *Nuclear Instruments and Methods in Physics Research*, 221(1):183–186.

Ciocia, F., Braem, A., Chesi, E., De Leo, R., Joram, C., Lagamba, L., Nappi, E., Séguinot, J., Vilardi, I., and Weilhammer, P. (2009). GEANT4 studies on the propagation and detection of scintillation light in long thin YAP crystals. *Nuclear Instruments and Methods in Physics Research, Section A: Accelerators, Spectrometers, Detectors and Associated Equipment*, 600(2):506–512.

Court, A. J., Dean, A. J., Yearworth, M., Younis, F., Butler, R. C., Caroli, E., Di Cocco, G., Stephen, J. B., Chiappetti, L., Perotti, F., Villa, G., Ubertini, P., and La Padula, C. (1988). A position sensitive detector using a NaI(Tl)/photomultiplier tube combination for the energy range 200 keV to 10 MeV. *Nuclear Instruments and Methods in Physics Research Section A: Accelerators, Spectrometers, Detectors and Associated Equipment*, 273(2-3):706–710.

Gilmore, G. R. (2008). *Practical Gamma-Ray Spectrometry*. John Wiley & Sons, Wenheim, 2nd edition.

Gormley, J. E., Rogers, W. L., Clinthorne, N. H., Wehe, D. K., and Knoll, G. F. (1997). Experimental comparison of mechanical and electronic gamma-ray collimation. *Nuclear Instruments and Methods in Physics Research, Section A: Accelerators, Spectrometers, Detectors and Associated Equipment*, 397(2-3):440–447.

Kagaya, M., Katagiri, H., Enomoto, R., Hanafusa, R., Hosokawa, M., Itoh, Y., Muraishi, H., Nakayama, K., Satoh, K., Takeda, T., Tanaka, M. M., Uchida, T., Watanabe, T., Yanagita, S., Yoshida, T., and Umehara, K. (2015). Development of a low-cost-high-sensitivity Compton camera using CsI (Tl) scintillators (γI). *Nuclear Instruments and Methods in Physics*

Research, Section A: Accelerators, Spectrometers, Detectors and Associated Equipment, 804:25–32.

Kaloskamis, N. I., Chan, K. C., Chishti, A. A., Greenberg, J. S., Lister, C. J., Freedman, S. J., Wolanski, M., Last, J., and Utts, B. (1993). The trigger detector for APEX: An array of position-sensitive NaI(Tl) detectors for the imaging of positrons from heavy-ion collisions. *Nuclear Instruments and Methods in Physics Research Section A: Accelerators, Spectrometers, Detectors and Associated Equipment*, 330(3):447–457.

Kataoka, J., Kishimoto, A., Nishiyama, T., Fujita, T., Takeuchi, K., Kato, T., Nakamori, T., Ohsuka, S., Nakamura, S., Hirayanagi, M., Adachi, S., Uchiyama, T., and Yamamoto, K. (2013). Handy Compton camera using 3D position-sensitive scintillators coupled with large-area monolithic MPPC arrays. *Nuclear Instruments and Methods in Physics Research, Section A: Accelerators, Spectrometers, Detectors and Associated Equipment*, 732:403–407.

Kataoka, J., Kishimoto, A., Taya, T., Mochizuki, S., Tagawa, L., Koide, A., Sueoka, K., Morita, H., Maruhashi, T., Fujieda, K., Kurihara, T., Arimoto, M., Okochi, H., Katsumi, N., Kinno, S., Matsunaga, K., Ikeda, H., Shimosegawa, E., Hatazawa, J., Ohsuka, S., Toshito, T., Kimura, M., Nagao, Y., Yamaguchi, M., Kurita, K., and Kawachi, N. (2018). Ultracompact Compton camera for innovative gamma-ray imaging. *Nuclear Instruments and Methods in Physics Research, Section A: Accelerators, Spectrometers, Detectors and Associated Equipment*, 912:1–5.

Kishimoto, A., Kataoka, J., Nishiyama, T., Fujita, T., Takeuchi, K., Okochi, H., Ogata, H., Kuroshima, H., Ohsuka, S., Nakamura, S., Hirayanagi, M., Adachi, S., Uchiyama, T., and Suzuki, H. (2014). Performance and field tests of a handheld Compton camera using 3-D position-sensitive scintillators coupled to multi-pixel photon counter arrays. *Journal of Instrumentation*, 9(11):P11025–P11025.

Knoll, G. E. (2000). *Radiation detection and measurement.* John Wiley & Sons, New York, 3rd ed. edition.

Llosá, G. (2019). SiPM-based Compton cameras. *Nuclear Instruments and Methods in Physics Research, Section A: Accelerators, Spectrometers, Detectors and Associated Equipment*, 926:148–152.

MacLeod, A. M. L., Boyle, P. J., Hanna, D. S., Saull, P. R. B., Sinclair, L. E., and Seywerd, H. C. J. (2014). Development of a Compton imager based on bars of scintillator. *Nuclear Instruments and Methods in Physics Research, Section A: Accelerators, Spectrometers, Detectors and Associated Equipment*, 767:397–406.

Ordonez, C. E., Bolozdynya, A., and Chang, W. (1997). Doppler broadening of energy spectra in Compton cameras. *1997 IEEE Nuclear Science Symposium Conference Record*, 2:1361–1365.

Ordonez, C. E., Wei Chang, and Bolozdynya, A. (1999). Angular uncertainties due to geometry and spatial resolution in Compton cameras. *IEEE Transactions on Nuclear Science*, 46(4):1142–1147.

Saito, K., Mikami, S., Andoh, M., Matsuda, N., Kinase, S., Tsuda, S., Yoshida, T., Sato, T., Seki, A., Yamamoto, H., Sanada, Y., Wainwright-Murakami, H., and Takemiya, H. (2019). Summary of temporal changes in air dose rates and radionuclide deposition densities in the 80 km zone over five years after the Fukushima Nuclear Power Plant accident. *Journal of Environmental Radioactivity*, 210:105878.

Saito, K. and Onda, Y. (2015). Outline of the national mapping projects implemented after the Fukushima accident. *Journal of Environmental Radioactivity*, 139:240–249.

Salvat, F. (2015). PENELOPE-2014: A Code System for Monte Carlo Simulation of Electron and Photon Transport. *OECD Nuclear Energy Agency*.

Sanada, Y., Orita, T., and Torii, T. (2016). Temporal variation of dose rate distribution around the Fukushima Daiichi nuclear power station using unmanned helicopter. *Applied Radiation and Isotopes*, 118:308–316.

Sanada, Y. and Torii, T. (2015). Aerial radiation monitoring around the Fukushima Dai-ichi nuclear power plant using an unmanned helicopter. *Journal of Environmental Radioactivity*, 139:294–299.

Sanada, Y., Urabe, Y., Sasaki, M., Ochi, K., and Torii, T. (2018). Evaluation of ecological half-life of dose rate based on airborne radiation monitoring following the Fukushima Dai-ichi nuclear power plant accident. *Journal of Environmental Radioactivity*, 192:417–425.

Scheit, H., Glasmacher, T., Ibbotson, R. W., and Thirolf, P. G. (1999). A position sensitive high-efficiency NaI(Tl) photon-detection system for use with intermediate energy radioactive ion beams. *Nuclear Instruments and Methods in Physics Research, Section A: Accelerators, Spectrometers, Detectors and Associated Equipment*, 422(1-3):124–128.

Sempau, J., Badal, A., and Brualla, L. (2011). A PENELOPE-based system for the automated Monte Carlo simulation of clinacs and voxelized geometries-application to far-from-axis fields. *Medical Physics*, 38(11):5887–5895.

Syntfeld-Kazuch, A., Swiderski, L., Czarnacki, W., Gierlik, M., Klamra, W., Moszynski, M., and Schotanus, P. (2006). Non-proportionality and Energy Resolution of CsI(Tl). *2006 IEEE Nuclear Science Symposium Conference Record*, 2:1144–1149.

Takeda, S., Harayama, A., Ichinohe, Y., Odaka, H., Watanabe, S., Takahashi, T., Tajima, H., Genba, K., Matsuura, D., Ikebuchi, H., Kuroda, Y., and Tomonaka, T. (2015). A portable Si/CdTe Compton camera and its applications to the visualization of radioactive substances. *Nuclear Instruments and Methods in Physics Research, Section A: Accelerators, Spectrometers, Detectors and Associated Equipment*, 787:207–211.

Vargas, A., Camp, A., Roig, M., Duch, M. A., and Stöhlker, U. (2015). Metrology for radiological early warning networks in Europe. *MetroERM project. Deliverable D1.3.3 /D5(REG2)*.

Vilardi, I., Braem, A., Chesi, E., Ciocia, F., Colonna, N., Corsi, F., Cusanno, F., De Leo, R., Dragone, A., Garibaldi, F., Joram, C., Lagamba, L., Marrone, S., Nappi, E., Séguinot, J., Tagliente, G., Valentini, A., Weilhammer, P., and Zaidi, H. (2006). Optimization of the effective light attenuation length of YAP:Ce and LYSO:Ce crystals for a novel geometrical PET concept. *Nuclear Instruments and Methods in Physics Research, Section A: Accelerators, Spectrometers, Detectors and Associated Equipment*, 564(1):506–514.

Wilderman, S. J., Clinthorne, N. H., Fessler, J. A., and Rogers, W. L. (1998). List-mode maximum likelihood reconstruction of compton scatter camera images in nuclear medicine. *1998 IEEE Nuclear Science Symposium Conference Record. 1998 IEEE Nuclear Science Symposium and Medical Imaging Conference (Cat. No.98CH36255)*, 3:1716–1720.

Wilderman, S. J., Rogers, W. L., Knoll, G. F., and Engdahl, J. C. (1997). Fast algorithm for list mode back-projection of compton scatter camera data. *1997 IEEE Nuclear Science Symposium Conference Record*, 1:391–395.

Xiaofeng, G., Qingpei, X., Dongfeng, T., Yi, W., Fanhua, H., Yingzeng, Z., Chengsheng, C., and Na, L. (2017). Simulation study of the backward-scattering effect in Compton imager. *Applied Radiation and Isotopes*, 124:93–99.

Xu, D., He, Z., Lehner, C. E., and Zhang, F. (2004). 4pi Compton imaging with single 3D position-sensitive CdZnTe detector. *Hard X-Ray and Gamma-Ray Detector Physics VI*, 5540:144–155.

Zych, A. D., Tumer, O. T., and Dayton, B. (1983). Gamma Ray Detection with Long NaI(Tl) Scintillator Bars. *IEEE Transactions on Nuclear Science*, 30(1):383–386.